Master's thesis

NTNU
Norwegian University of Science and Technology
Faculty of Natural Sciences
Department of Physics

Mats Topstad

# Charged ferroelectric domain walls in $K_2MgWP_2O_{10}$ and $K_3Nb_3B_2O_{12}$ studied by transmission electron microscopy

Master's thesis in Nanotechnology
Supervisor: Antonius T. J. van Helvoort
Co-supervisor: Dennis Meier and Ivan Ushakov
June 2023

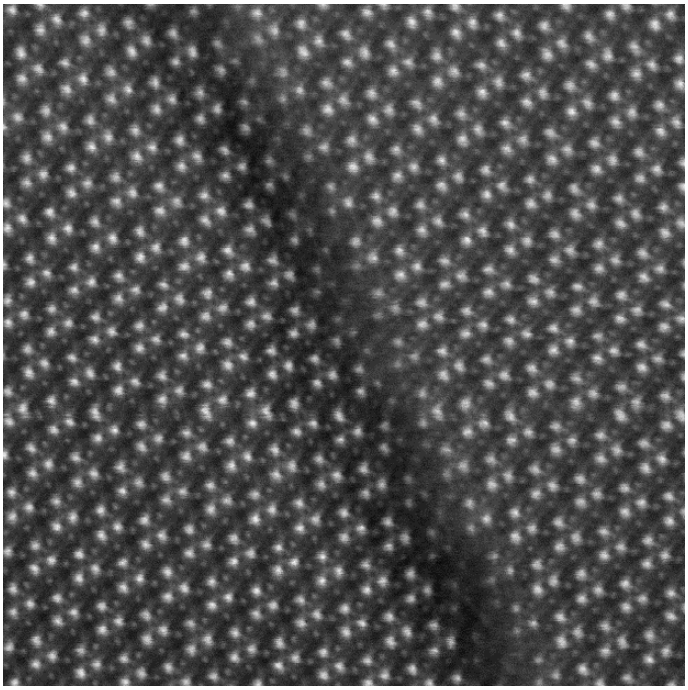

NTNU
Norwegian University of
Science and Technology

Mats Topstad

# Charged ferroelectric domain walls in $K_2MgWP_2O_{10}$ and $K_3Nb_3B_2O_{12}$ studied by transmission electron microscopy

Master's thesis in Nanotechnology
Supervisor: Antonius T. J. van Helvoort
Co-supervisor: Dennis Meier and Ivan Ushakov
June 2023

Norwegian University of Science and Technology
Faculty of Natural Sciences
Department of Physics

NTNU
Norwegian University of
Science and Technology

# ABSTRACT

Charged domain wall engineering is an emerging and exciting field that focuses on manipulating the functional properties of domain walls. Two promising ferroelectric oxides, $K_2MgWP_2O_{10}$ (KMWPO) and $K_3Nb_3B_2O_{12}$ (KNBO), have here been studied by transmission electron microscopy (TEM). This thesis employs a correlated microscopy approach, utilizing polarized light microscopy (PLM) and scanning probe microscopy (SPM) to prepare TEM specimens in a specific direction that contain domain walls. The successful site-specific specimen preparation involved correlated microscopy and mechanical tripod polishing. Resulting in high quality millimeter-sized tripod wedges of KMWPO in the [110] direction and of KNBO in the [001] direction were obtained.

This thesis presents the first TEM characterization of KMWPO, employing various electron diffraction techniques, conventional TEM, high-resolution TEM (HRTEM), and high-angle annular-dark field scanning TEM (HAADF STEM). The domain structure of the material was analyzed, revealing stripe domains ranging from less than a micron to a couple micrometer in width. A similar domain configuration was observed by piezoresponse force microscopy (PFM) configuration, indicating a polarization in-plane, in agreement with dark-field STEM indicating that the polar direction is $1\bar{1}0$. Detailed TEM investigations are impaired by beam damage indicating there is a critical dose over which the structure turns amorphous.

Using the same tripod polishing approach for the harder KNBO, charged head-to-head (H-H) twinning domain walls were studied for the first time by TEM. The twinning is characterized by a 120° rotation around the $c$-axis. As the orthorhombic structure is pseudo-hexagonal this rotation can not be observed in lattice imaging nor selected area diffraction. The rare presence charged twinning domains were identified by PFM and PLM and require highly site-specific specimen preparation. The position of H-H domain walls could be identified by conventional TEM and medium magnification HAADF STEM. Lattice imaging with HAADF STEM in an aberration-corrected microscope allowed atomic scale structural analysis of the H-H twinning domains. The domain walls span across less than a unit cell, with additional Nb columns situated between the 120° rotated twinning domains. Notably, atomic shifts were observed in the $c$-direction, further causing structural distortions and atomic shifts along the $b$-direction across the interface. Two types of interfaces were found. i) two straight boundaries along the $2\bar{3}0$ direction displaced in the $c$-direction ii) an inclined boundary with step shifts every 12 nm with the two domains shifted in the $c$-direction relative to each other. Conversely, the tail-to-tail (T-T) is found to have an absence of a structural discontinuity.

# SAMMENDRAG

Ladet domenevegg teknikk er et fremvoksende og spennende felt som fokuserer på å manipulere de funksjonelle egenskapene til domenevegger. To lovende ferroelektriske oksider, $K_2MgWP_2O_{10}$ (KMWPO) og $K_3Nb_3B_2O_{12}$ (KNBO), er her blitt studert ved hjelp av transmisjonselektronmikroskopi (TEM). Denne oppgaven tar i bruk en korrelert mikroskopi tilnærming, med polarisert lysmikroskopi (PLM) og sveipeprobe-mikroskopi (SPM) for å forberede TEM-prøver i en bestemt retning som inneholder domenevegger. Den vellykkede stedspesifikke prøvepreparasjonen involverte korrelert mikroskopi og mekanisk tripod polering. Resultatet var millimeterstore tripod kiler formet prøver av høy kvalitet for KMWPO i [110]-retning og for KNBO i [001]-retning.

Denne oppgaven presenterer den første TEM-karakteriseringen av KMWPO og benytter ulike elektrondiffraksjonsteknikker, konvensjonell TEM, høyoppløsnings-TEM (HRTEM) og høy-vinkel annulære mørke felt sveipe TEM (HAADF STEM). Materialeets domenestruktur ble analysert og viste stripede domener med bredde fra mindre enn en mikrometer til et par mikrometer. En lignende domenekonfigurasjon ble observert av piezorespons kraft mikroskopi (PFM), som indikerte en polarisering i plan, i enighet mørkefelt STEM som indikerer at den polare retningen er $1\bar{1}0$. Detaljerte TEM-undersøkelser er begrenset av stråleskader, som indikerer at det finnes en kritisk dose der strukturen blir amorf.

Ved å bruke samme tripod polering tilnærmingen for det hardere KNBO, ble ladete hode-til-hode (H-H) tvillingdomener studert for første gang ved hjelp av TEM. Tvillingdomenene karakteriseres av en rotasjon på 120° rundt $c$-aksen. Siden den ortorombiske strukturen er pseudo-heksagonal, kan denne rotasjonen ikke observeres i gitteravbildning eller utvalgt område-diffraksjon. De sjeldne ladete tvillingdomenene ble identifisert ved hjelp av PFM og PLM og krever høyt stedsspesifikk prøvepreparasjon. Posisjonen til H-H domenevegger kunne identifiseres ved hjelp av konvensjonell TEM og HAADF STEM ved middels forstørrelse. Gitteravbildning med HAADF STEM i et aberrasjons-korrigert mikroskop tillot strukturanalyse på atomnivå av H-H tvillingdomenene. Domeneveggene strekker seg over mindre enn en enhets-celle, med ekstra Nb-kolonner plassert mellom de 120° roterte tvillingdomenene. Bemerkelsesverdig ble det observert atomforskyvninger i $c$-retningen, som videre forårsaket strukturelle forvrengninger og atomforskyvninger langs $b$-retningen på tvers av grenseflaten. To typer grenseflater ble identifisert: i) to rette grenseflater langs $2\bar{3}0$ retningen forskyvet i $c$-retningen, og ii) en skrå grenseflate med trinnforskyvninger hver 12 nm der de to domenene er forskjøvet i $c$-retningen i forhold til hverandre. Omvendt, så er det ingen strukturell diskontinuitet i hale-til-hale (T-T) konfigurasjonen.

# PREFACE

With this thesis, I conclude my studies towards the MSc degree in Nanotechnology with specialization within Nanoelectronics at the faculty of Natural Sciences at the Norwegian University of Science and Technology (NTNU). The work presented in this thesis is the result of one years work starting August 2022 with the deadline of June 2023. During the first semester, the main focus was to get accustomed to and familiarize the instruments and methods at the TEM Gemini centre at the NORTEM department. The last semester has been spent on the work presented in this thesis.

I would like to express my sincere gratitude to my supervisor Antonius T. J. van Helvoort, for his encouraging and insightful guidance throughout the project. I am grateful for the rewarding opportunity to work under supervision of him for the Department of Physics, including the co-supervisors Dennis Meier and Ph.D. candidate Ivan Ushakov. Lastly, I would like to thank my favourite tweezers, Ricky and Julian, for all the good times in the lab. All the work presented in this thesis has been performed by the author, except for the PFM and EFM measurements on the bulk KNBO and KMWPO and the collection of data on the ARM instrument. The PFM and EFM measurements were performed by my co-supervisor Ivan Ushakov, while the data acquisition on ARM was performed by Dr E. Christiansen or Dr U. Ludacka.

Mats Topstad
NTNU, Trondheim
June $19^{th}$, 2023

# CONTENTS

# ABBREVIATIONS

- **CBED** Convergent-beam electron diffraction
- **CDW** Charged domain wall
- **DI** Deionized
- **DLF** Diamond lapping film
- **EFM** Electrostatic force microscopy
- **FEG** Field emission gun
- **FOLZ** First order laue zone
- **H-H** Head-to-head
- **KMWP** $K_2MgWP_2O_{10}$
- **KNBO** $K_3Nb_3B_2O_{12}$
- **HAADF** High angle annular dark-field
- **HRTEM** High-resolution transmission electron microscopy
- **NTNU** Norwegian University of Science and Technology
- **PCTF** Phase contrast transfer function
- **PFM** Piezoresponse force microscopy
- **PLM** Polarized light microscopy
- **SPM** Scanning probe microscopy
- **STEM** Scanning transmission electron microscopy
- **SAED** Selected area electron diffraction
- **TEM** Transmission electron microscopy
- **T-T** Tail-to-tail
- **VLM** Visual light microscope

CHAPTER

# ONE

# INTRODUCTION

Using ferroelectric materials, mostly as thin films, has for an extended period of time gained much attention for technological applications [1]. More recently, the attention has been shifted towards domain walls engineering, an emerging field that involves manipulating the functional properties of domain walls (DW) [2, 3], being the boundaries between regions of different electric or magnetic polarization. Ferroelectric domain wall engineering offers new ways of altering the functional properties of interfaces, such as their electronic and magnetic properties. Within this new paradigm, the domain walls are the active element rather than the domains as they have fundamental intriguing aspects. Further development within the field of charged domain wall engineering could enable the creation of new type of electronic devices with enhanced functionality and performance [4]. This new emerging technology has the potential to address several societal challenges such as energy harvesting and storage, sustainable electronics, and advancements in computing technologies [5, 6].

Ferroelectric domain walls are thin regions of a finite distance that separate ferroelectric domains of differently oriented polarizations [7]. Depending on the structural configuration, the polarization of adjacent domains can result in charged or uncharged interfaces. In an uncharged domain wall, the polarization direction rotates smoothly across the wall, with no net charge. Oppositely, in a charged domain wall (CDW), the polarization across the wall is also coupled to the presence of charged species, such as ions or electrons. These charged species affects the domain wall properties altering its conductivity, allowing the possibility to modify the electronic structure of the boundary and functionalizing it [8]. By functionalizing domain walls, researchers can tailor their electronic and polarization properties to create new innovative applications [9, 10, 11].

Ferroelectric domains occur naturally in ferroelectric materials, with the different polarities being energetically equivalent states, enabling switchable polarization through the application of an external electric field with field strength higher than the coercive field, $E_c$. In addition, application of an external field can induce motion of domain walls. In this way, ferroelectric domains can respond to external stimuli, due to a force imposed on the domain wall from the field to move it in a specific direction. Depending on the direction and strength of the field applied, the speed and direction of the movement can be controlled. In addition, there are other ways of manipulating domain walls spatially, such as mechanical stress

and applying an electric current. For this reason, the domain walls are termed as mobile, meaning they can be created, reshaped, moved, or erased to create a spatially mobile interface. Overall, the ability to manipulate the functionality and the spatially mobile interfaces in an otherwise insulating material offers a promising avenue. By combining the possibility to functionalize domain walls with their mobility, researchers can create domain walls with tailored properties to function as the active element in a variety of devices.

In order to understand these spatially mobile interfaces, it is important to understand the underlying mechanisms and the symmetry-property relationship of crystal structures [12]. The crystal symmetry of a material determines the possible directions of spontaneous polarization and its magnitude, which in turn affects the coupling between electric polarization and other functional properties [13]. Investigating these relationships are essential for prediction and control of the tailored properties in the process of designing technological applications. Conventional ferroelectric oxides, such as $BaTiO_3$ and multiferroic $BiFeO_3$, have for a longer time been utilized in ferroelectric applications. These are studied extensively at the atomic scale and are well understood [14, 15]. More exotic materials on the other hand, such as ferroelectric $LiNbO_3$ and multiferroic $ErMnO_3$ have been actively studied in the field of domain wall engineering more recently [9, 16]. They have actively been pursued because of their interesting properties for the use in a variety of applications. As the field have continued to expand, new and more complex ferroelectric and multiferroic materials are emerging as potential candidates for charged domain wall engineering for their special domain wall functionalities and unique promising properties. Twinned materials are at the centre of the search of materials for domain wall engineering, due to its possibility to functionalize the twin boundaries. Amongst the new candidates, there is $K_3Nb_3B_2O_{12}$ (KNBO) due to its unique multiferroic properties. The material displays ferroelectric, ferroelastic, and antiferroelectric properties at room temperature, making it a highly interesting material for domain wall engineering. Its antiferroelectric response is shown by the presence of an double P-E hysteresis loop [17, 18], leaving doubt about the materials true ferroic nature. In addition, KNBO exhibits ferroelastic twinning domains, showing three different twinning axes rotated by 120° relative to each other. At the lamellar twinning boundary between two twinning domains, a small fraction of the domain walls is observed as charged domain walls, displaying interesting functional properties. Kelvin probe force microscopy (KPFM) measurements of the ferroelectric boundaries show that the H-H configuration walls are charged while the T-T configurations walls are uncharged. Based on this, there has to be a deviation in the structural configurations between these domain walls. To be able to prove and understand this, high resolution lattice imaging is necessary to study the material at high spatial resolution. For this, transmission electron microscopy (TEM) is a popular option that utilizes powerful techniques capable of capturing atomic resolution images as well as obtaining a great variety of information from the material [13, 19].

While current candidates for domain wall engineering show promise, there are constantly new candidates with unique properties that could have important implications for the field. Not all materials exhibiting multiferroic properties are suitable for charged domain wall engineering applications, hence the need for continuous exploration of new materials. Amongst the interesting novel candidates,

$K_2MgWP_2O_{10}$ (KMWPO) is noteworthy due to its exciting properties, including ferroelectric, ferroelastic, and nonlinear optical properties at room temperature. Despite being relatively understudies, with only a few published papers on the material and no TEM studies previously reported, KMWPO exhibits interesting and complex twinning domains that are believed to be linked to its structural phase transitions.

In order to conduct site-specific specimen preparation for characterization of multiferroic materials, correlated microscopy techniques are employed to identify specific areas of the specimen with unique properties or characteristics. These areas are then prepared for further specimen preparation techniques. One approach is using PFM to identify the areas of interest, followed by ion milling by focused ion beam (FIB) to prepare a thin section of the specimen, known as lamella, for transmission electron microscopy. However, this technique results in a limited area that could potentially be prone to poling or alteration of ferroelectric domains due to the charged ions used in the process. Alternatively, PFM followed by a mechanical method that provides larger areas for specimen preparation could be employed. One advantageous technique in this regard is the tripod polishing technique, which results in a wedge-shaped specimen with millimeter-sized electron transparent edge of sufficient quality for investigating domain boundaries and to reveal their structural configuration with atomic resolution. For this, TEM is an appropriate instrument offering a variety of imaging techniques are employed to investigate anomalies generated by structural gradients in domain walls.

One of the limiting challenges in determining the structural configuration of domain walls is the specimen preparation. It requires the presence of domain walls exhibiting the properties of interest within the specimen and the use of techniques that can achieve sufficient resolution, often complimented by simulated models predicting the structural configuration. Density functional theory (DFT) simulations is a widely applied model for simulation of the local atomic and electronic structure, including domain walls and can be applied to materials such as KMWPO and KNBO. Within the commonly used simulations, the system adopts the lowest energy state to create structural models for materials [20]. Therefore, this report proposes a general workflow for investigating domain walls in multiferroic materials to determine their structural configuration. This involves i) to determine the viability of site-specific specimen preparation using correlated microscopy techniques, ii) provide an initial TEM characterization using appropriate imaging techniques to analyse the interesting properties reported for KMWPO, and iii) determine the structural configuration of the charged H-H twinning domain walls in KNBO.

CHAPTER

# TWO

# THEORY

The theory section presents the theoretical background relevant for the results and discussion in this project. This chapter begins by giving an introduction to crystallography and diffraction, before presenting ferroic materials. Further, an introduction to TEM is presented together with the techniques relevant for this project. Ultimately, a literature review section on KMWPO and KNBO is presented. A great deal of the theory presented is taken from previous work of the author [21], with some additional sections included.

## 2.1 Crystallography

Crystallography is the branch of science that deals with crystal structures and how to describe them. Crystallography has a strict and precise language which can be used in the understanding of atomic structures and properties related. A general introduction with the most important terms will be presented in this section. The first sections are based on based on a book titled *Introduction to Solid State Physics* by Charles Kittel [7], while the last sections are based on a paper by Dauter and Jaskolski [22].

### 2.1.1 Crystal Structure

Atoms in crystalline materials are organized periodically and systematically into unit cells. The identical building blocks are repeated continuously in a periodic array in a three-dimensional fashion forming the crystal. However real crystals are never perfect and will have point defects, planar defects or impurities accidentally included in the structure. Deviations from a perfect crystal structure will affect its physical properties, for example its conductivity. Periodical crystals can be categorized into a system of different geometric structures of crystal lattices, which can be described by mathematical vectors.

### 2.1.2 Mathematical Description

An ideal crystal contains an infinite periodical arrangement of identical atoms or sets of atoms which are called the basis. The basis is located on every lattice site.

The lattice, forms a three-dimensional arrangement that can be expressed mathematically by three translation vectors **a**, **b**, **c**. These are primitive translation vectors that can be multiplied by integer values to translate between identical points. The translation vector, a translation in which the atoms in the crystal look the same, can be defined as:

$$\mathbf{T} = u_1\mathbf{a} + u_2\mathbf{b} + u_3\mathbf{c} \tag{2.1}$$

Where $u_1$, $u_2$, and $u_3$ are integers moving along each of the directions in the lattice.

For the instance where the lattice looks the same after a translation of a suitable choice of integers, the lattice is primitive. The vectors that span the unit cell are called the primitive translation vectors, spanning a volume $V_c = \mathbf{a} \cdot \mathbf{b} \times \mathbf{c}$. The primitive unit cell corresponds to a unit cell containing a single lattice point in a primitive structure. For a given lattice, there are multiple choices of the primitive unit cell, that when repeated fill all space. Crystals can be mapped the crystal lattices into themselves by a translation **T** or by various symmetry operations. Amongst the symmetry operations, there is rotation symmetry around an axis passing through a lattice point, that allows periodic lattices to show one-, two-, three-, four- and sixfold symmetry, corresponding to $2\pi/n$ rotations. Fivefold symmetry is not allowed since the primitive unit cell does not fill out all space.

The primitive unit cell, if cubic, consist of $\frac{1}{8}$ atom on the corners, which is more convenient than 1 encapsulated atom in a cube, although it is allowed as both have one point per cell. The Wigner-Seitz cell and Brillouin zone are defined for the crystal and reciprocal lattice respectively. Other choices are viable when there are relations of symmetry that make it convenient to work with. Furthermore, the primitive translation vectors are often used as a definition of the crystal axes. The interaxial angles between the crystal axes are commonly defined as:

$$\mathbf{a}\angle\mathbf{b} = \gamma, \quad \mathbf{a}\angle\mathbf{c} = \beta, \quad \mathbf{b}\angle\mathbf{c} = \alpha \tag{2.2}$$

For the understanding of planes and directions within the lattice, Miller indices are used. Miller indices are sets of three numbers (hkl) indicating the orientation of planes or sets of parallel planes intersecting the crystallographic vector axes. Miller indices are found by taking the reciprocal of the intersection with the crystallographic axes and multiplying them with a common denominator resulting in the smallest possible integers (hkl). An example is the intersection of the $a$-axis at $\frac{1}{2}$, the $b$-axis at 1 and parallel to the $c$-axis, as illustrated in Figure 2.1. This gives the Miller indices (210) for a cubic crystal, giving the atomic plane or a set of parallel planes. Planes that intersect on the negative side of the origin, is indicated by placing a bar above the index (hk$\bar{l}$). Families of planes, symmetry equivalent planes, are denoted by curly brackets {hkl}

Since the periodic crystal is invariant under a translation of the form $\mathbf{T} = u_1\mathbf{a}_1 + u_2\mathbf{a}_2 + u_3\mathbf{a}_3$, then local physical properties of the crystal must also be invariant under **T**. This implies that Fourier analysis can be useful in the analysis of the crystal structure.

The reciprocal space can be related to real space by a Fourier transform. Within the reciprocal lattice, we can map out the set of vectors

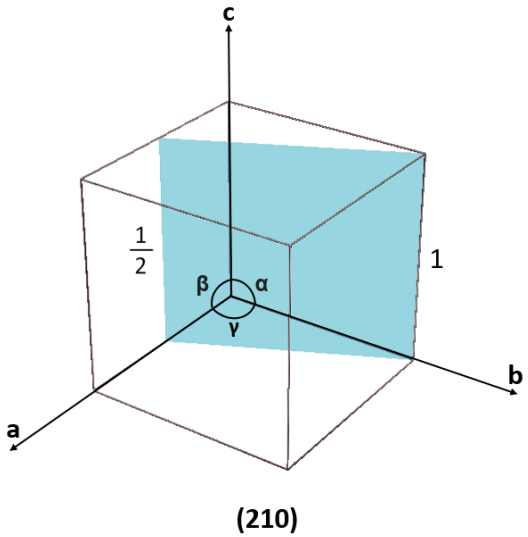


**Figure 2.1:** Schematic of plane intercepting the $a$- and $b$-axis, going parallel to the $c$-axis. Interception points are at $\frac{1}{2}\mathbf{a}$, $1\mathbf{b}$, and $\infty$c. Taking the reciprocal of the numbers gives the miller indices of the plane, (210).

.

$$b_i = 2\pi \frac{a_j \times a_k}{V_c}, \quad \epsilon_{ijk} = 1 \tag{2.3}$$

Where the b vectors are the primitive reciprocal lattice vectors and $a_1$, $a_2$, and $a_3$ refers to **a**, **b**, and **c**, respectively. Each vector defined is orthogonal to the remaining axis vectors of the crystal lattice. Therefore, the reciprocal lattice vectors have the property

$$b_i \cdot a_j = 2\pi\delta_{ij} \tag{2.4}$$

where $\delta_{ij} = 1$ if i = j and $\delta_{ij} = 0$ if $i \neq j$. This enables the translational symmetry, since $e^{iG\cdot(r+T)} = e^{iG\cdot r}$.

Similarly to real space, the points in reciprocal space are mapped out by the primitive reciprocal lattice vectors

$$G = v_1 b_1 + v_2 b_2 + v_3 b_3 \tag{2.5}$$

where $v_1$, $v_2$, $v_3$ are integers and the vector **G** is a reciprocal lattice vector.

### 2.1.3 Systematic Description of Crystals

Crystals take the form of one of the seven crystal systems shown table 2.1.1, originating from the different ways in which a periodic array can be made up in three dimensions and determines their symmetries. Furthermore, they can be divided into subgroups depending on their primitive unit cell. There are in total fourteen different ways a three-dimensional crystals can be arranged, called Bravais Lattices. A Bravais lattice is the array of points in which the repeated units of a crystal can be arranged and oriented such that it is invariant under a translation to any other discrete point. A Bravais lattice considers only the geometric aspect

of the periodic structure, regardless of its units. Bravais lattices belongs to one of the seven crystal systems, and contains a description of the unit cell. The general structure is the triclinic, together with the remaining thirteen lattices being special variation. These are either Primitive (P), Base-centered (C), Body-centered (I), or Face-centered (F). The fourteen Bravais lattices are illustrated in Figure 2.2 and consist of one triclinic (P), two monoclinic (P, C), four orthorhombic (P, C, I, F), two tetragonal (P, I), three cubic (P, I, F), one trigonal (P) and one hexagonal (P).

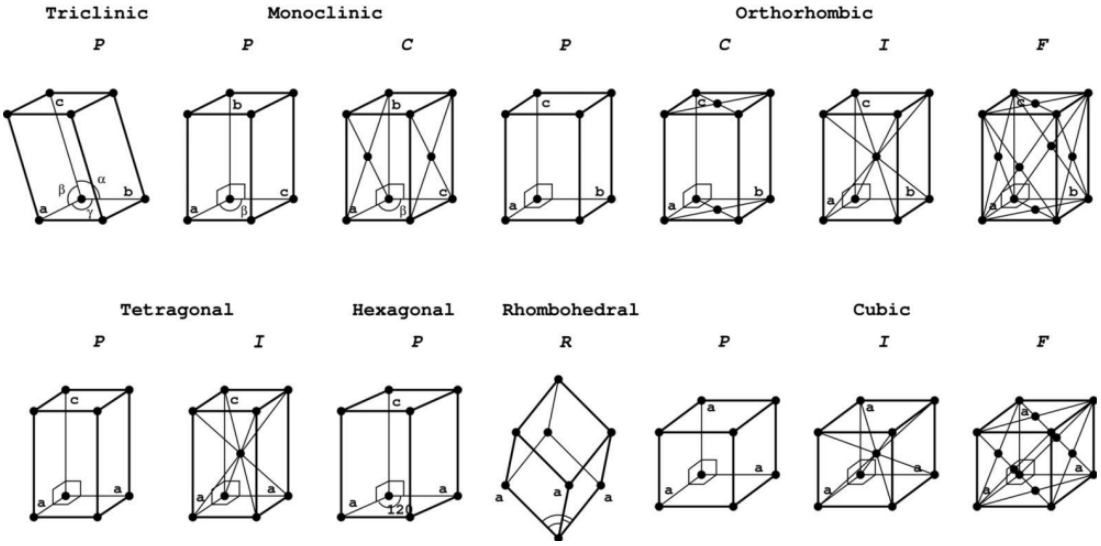


**Figure 2.2:** The 14 Bravais Lattices. Image taken from [22]

.

### 2.1.4 Symmetry of Crystals

The symmetry of crystals can be used in their description, as physical properties such as conductivity and polarization are dependent upon the symmetry elements. In general, lattice points can be described by a small group of symmetry elements such as rotations (1,2,3,4,6), reflection (m), inversion (i) and rotation-inversion. There are in total 32 unique point groups used in the description of 3D crystal structures. Point groups are the collection of symmetry operations that when applied about a lattice point, map the lattice into itself. One example is that unit cells can be mapped into themselves if they inherit n-fold symmetry which means they appear identical if they are rotated by $2\pi/n$. Mirror planes $m$ are reflections about a plane going through a lattice point, whilst an inversion is a rotation $\pi$ followed by a reflection normal to the rotation axis. An example is the 3-fold axis through the cubic crystal's body diagonal. Another symmetry element, rotoinversion, is a combination of a rotation and an inversion across an inversion center.

The 32 point groups convoluted with the 14 crystal lattice make up in total of 230 different space groups, ignoring duplicates, in three dimensions. These include two additional translation symmetry elements. Glide planes are mirror reflections through a plane combined with lattice translations parallel to it. A screw axis is

**Table 2.1.1:** The seven crystal systems in 3D space with their lengths and inter-axial angles between the crystal axes.

| System | Restrictions |
|---|---|
| Triclinic | $a_1 \neq a_2 \neq a_3$<br>$\alpha \neq \beta \neq \gamma$ |
| Monoclinic | $a_1 \neq a_2 \neq a_3$<br>$\alpha = \beta = 90^\circ \neq \gamma$ |
| Orthorhombic | $a_1 \neq a_2 \neq a_3$<br>$\alpha = \beta = \gamma = 90^\circ$ |
| Tetragonal | $a_1 = a_2 \neq a_3$<br>$\alpha = \beta = \gamma = 90^\circ$ |
| Cubic | $a_1 = a_2 = a_3$<br>$\alpha = \beta = \gamma = 90^\circ$ |
| Rhombohedral | $a_1 = a_2 = a_3$<br>$\alpha = \beta = \gamma < 120^\circ, \neq 90^\circ$ |
| Hexagonal | $a_1 = a_2 \neq a_3$<br>$\alpha = \beta = 90, \gamma = 120^\circ$ |

a rotation along a screw axis combined with a translation along the screw axis. All crystals fall within one of the space groups, which can be uniquely described by the lattice translation vector or symmetry elements.

There are in general two different notations generally used within the field of crystallography. The Hermann-Mauguin notation and the Schoenflies notation. The Hermann-Mauguin notation will be used in the description of symmetry elements in the crystal in this thesis.

Relationships between symmetries and the physical properties of macroscopic crystals are governed by Neumann's principle, also known as the principle of symmetry. It states that: if a crystal is invariant to certain symmetry elements, then any of its physical properties must also remain invariant to the same symmetry elements. Therefore, macroscopic physical properties are directly related to the symmetry elements of the point group of the crystal and vice versa. For this reason, a grouping of crystals based on the symmetries is of great interest.

### 2.1.5 Nomenclature

The International Tables for Crystallography is based on Hermann-Mauguin notations, which are necessary to describe to comprehend the crystallographic representation and crystal planes [23]. The Hermann-Mauguin notation consist of a series of symbols that represents the symmetry elements present in the crystal. The explanation given below is limited to orthorhombic crystal since it is the most relevant choice for $K_3Nb_3B_2O_{12}$.

The description of space groups is dependent on the crystal structure. The space group notation can for example be written on the form $D_{fgh}$, where D is the Bravais lattice description (P, C, I, F), and $fgh$ are symmetry elements along various crystallographic directions. For example, space group 29 has the

Hermann-Mauguin notation $Pca2_1$ [23]. This can be described by having primitive orthorhombic unit cell with atoms at each corner. It has a c-glide plane with a reflection about the $a$-axis, an a-glide plane with a reflection about the $b$-axis and a $2_1$ screw axis along the $c$-axis. What $2_1$ screw plane means is that it has a 2-fold rotation along the $c$-axis combined with a $\frac{1}{2}$ translation along the axis, hence it is a neutral screw axis.

The 3 indices are related to the lattice parameters and can be placed in multiple orders. For orthorhombic crystals, this is along the **a**, **b**, and **c** direction, respectively. Orthorhombic space groups may have different notations used in their description. There are in total six possible choices, being **abc**, $\boldsymbol{ba\bar{c}}$, **cab**, $\boldsymbol{\bar{c}ba}$, **bca**, and $\boldsymbol{a\bar{c}b}$. It has to be taken into consideration which setting is used in published work and eventually transfer to the most common setting. Throughout this thesis, the **cab**-system will be consistently used as the choice of axis system, which is also the standard for the International Tables of Crystallography. Other common choices are related to convenience and preferred systems.

Overall, the Hermann-Mauguin notation is a concise and standarized notation that provides a way of describing the symmetry properties of space groups, which is essential for understanding the relationship between physical properties and symmetries of the crystal.

## 2.2 Diffraction

This section will present the basics of kinematical diffraction to explain how electrons interact with crystalline samples to form diffraction patterns in a TEM. The section is mainly based on the book by C. Kittel [7].

### 2.2.1 Kinematic Diffraction

Diffraction is a phenomenon of wave properties where constructive and destructive interference after a wave has interacted with matter allows one to retrieve information about the crystal structure. The method uses photons or the wave-like property of neutrons and electrons in the examination of materials. Analyzing crystals using diffraction is a widely used method, with an intuitive explanation given by Bragg's law, illustrated in Figure 2.3. The derivation is based on coherent interaction between waves partially reflected by parallel planes of atoms in a perfect crystal. The incident beam is locally coherent. Bragg explains that at certain reflection angles the phase accumulation from the distance traveled creates constructive interference. The beam enters the crystal at an angle $\theta$ and is scattered at different atomic planes resulting in a path difference. When the phase difference accumulated is exactly equal to an integer number of the wavelength $\lambda$, then we have Braggs' law:

$$2d_{hkl}sin(\theta) = n\lambda \tag{2.6}$$

Where $d_{hkl}$ is the interplanar spacing between the scattering planes and n is an integer. The Bragg law offers a simplified and widely used version of diffraction from atomic planes in crystals. The explanation is a consequence of the periodicity of the lattice and coherent scattering, showing the appearance of sharp maxima

peaks at certain angles satisfying Equation 2.6. From this relatively simple equation, we can retrieve structural information about the crystal if we know the input parameter $\lambda$ and measure the scattering angle $\theta$. The result is that the distance between the maxima of the scattered spots is inversely related to the interplanar distance. The relative intensity is related to the scattering power and the relative position of the scattering units, i.e. interference, as explained in the following section.

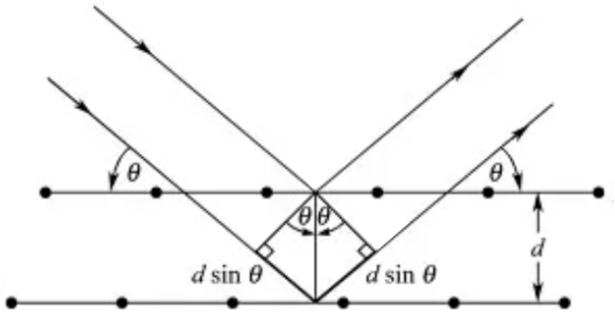


**Figure 2.3:** Bragg's law illustrated with its partially reflective planes. The total phase difference is $(\boldsymbol{k} - \boldsymbol{k'}) \cdot \boldsymbol{r}$

The wave vector, **k**, is the direction of the wavevector representing the direction of the phase velocity, normal to the wavefronts. The direction is often, but not always the same as the propagation direction. The wavevector **k** is related to the wavelength $\lambda$ through the relation $k = |\mathbf{k}| = \frac{2\pi}{\lambda}$.

We now define the scattering vector $\boldsymbol{\Delta k}$ as the difference between the incoming **k** and scattered wave vector **k'**.

$$\boldsymbol{\Delta k} = |\boldsymbol{\Delta k}| = \frac{4\pi}{\lambda} sin\theta \tag{2.7}$$

Charge density, n(**r**), is a physical property related to the crystal structure determined by the electron density distribution at atomic positions in the unit cell. It is repeated across the lattice structure with the same periodicity as the lattice itself, and thus invariant under a translation **T**. Because of this, Fourier analysis is extremely useful. The properties of crystals can be related to its Fourier components of the electron density. The periodic function n(**r**) across all three dimensions is given by:

$$n(\boldsymbol{r}) = \sum_{\boldsymbol{G}} n_G e^{i\boldsymbol{G}\cdot\boldsymbol{r}}, \quad where \quad n_{\boldsymbol{G}} = \frac{1}{V_c} \int_{V_{cell}} dV n(\boldsymbol{r}) e^{-i\boldsymbol{G}\cdot\boldsymbol{r}} \tag{2.8}$$

Where $V_c$ is the volume of the crystal.

The amplitude of the outgoing scattered wave in the direction **k'** is supposed proportional to the integral over the scattering density $\rho(r)$ for a given volume dV times the phase factor. The amplitude of the scattered wave is thus proportional to the integral defined as the quantity F, known as the scattering amplitude:

$$\boldsymbol{F} = \int_V dV \rho(r) e^{i(\boldsymbol{k}-\boldsymbol{k'})\cdot\boldsymbol{r}} \tag{2.9}$$

Which is essentially a Fourier transform of the scattering density $\rho(r)$. The change in wavevector is given by $\Delta k$, and is called the scattering vector.

The scattering density is dependent on which kind of wave is being used. For X-rays, the scattering density is simply the electron density. X-ray scattering is therefore dependent on atomic number, Z. For electrons, the scattering density is also dependent on coulomb interaction with the material, including the complete electrostatic potential. Inserting the formula given for electron density to replace the scattering density into Equation 2.9, the resulting scattering amplitude is:

$$\boldsymbol{F_G} = \sum_G \int dV \rho_{\boldsymbol{G}} e^{i(\boldsymbol{G}-\boldsymbol{\Delta k})\cdot \boldsymbol{r}} \tag{2.10}$$

As a result, the r dependence of this integral will average to zero unless the exponent goes to zero. This gives the diffraction condition $\boldsymbol{G} = \boldsymbol{\Delta k}$. The condition can be visualized by the Ewald sphere in Figure 2.4. It represents a geometrical construction in reciprocal space, in which the diffraction condition is fulfilled when the endpoints of the incoming and outgoing wave vectors are located on the sphere. If instead sample thickness is limited in the direction of the beam, there may still be diffraction without perfect overlap since the reciprocal points are elongated in the direction of limited thickness. For this condition, a modification is made with the help of the deviation parameter **s**, given by $\boldsymbol{\Delta k} = \boldsymbol{G} + \boldsymbol{s}$. The dependence of the intensity on the thickness of the sample and the deviation parameter is given for a specimen with thickness t and deviation parameter **s**:

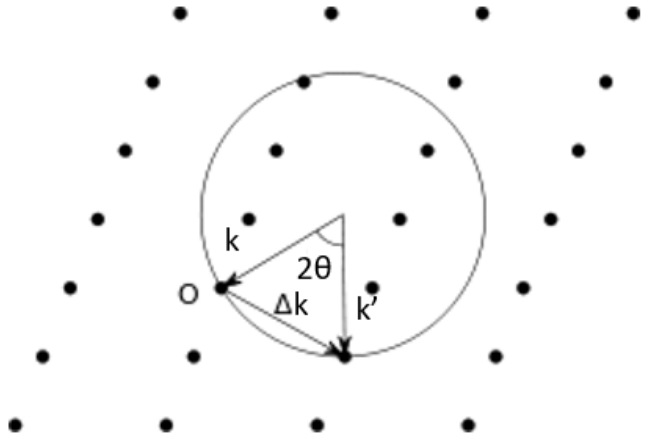


**Figure 2.4:** Schematic of Ewald sphere illustrated with **k** and **k'** being the incident and scattered wavevector, respectively. Electrons have a shorter wavelength and hence a much larger radius than illustrated here. The points which intercept with the Ewald sphere in reciprocal space will fulfill the Laue conditions. The angle $\theta$ corresponds with the angle in Fig. 2.3.

$$I_G(s) \sim \frac{sin^2(\pi t s)}{(\pi s)^2} \tag{2.11}$$

It has been shown that one can deduce the above.

By only considering elastic scattering of electron and neutron beams, we get that the magnitude of **k** is equal to **k'**, thus the diffraction conditions become:

$$(\boldsymbol{k}+\boldsymbol{G})^2 = k^2 \quad or \quad 2\boldsymbol{k}\cdot\boldsymbol{G} = G^2 \tag{2.12}$$

This is another statement of the Bragg condition in Equation 2.6. The diffraction condition $\mathbf{G} = \Delta\mathbf{k}$ can also be used to derive the Laue equations. A set of equations with a geometrical interpretation. By multiplying each side with the translational vectors **a**, **b**, and **c**, we get:

$$\boldsymbol{a}\cdot\boldsymbol{\Delta k} = 2\pi h, \quad \boldsymbol{b}\cdot\boldsymbol{\Delta k} = 2\pi k, \quad \boldsymbol{c}\cdot\boldsymbol{\Delta k} = 2\pi l \tag{2.13}$$

From each of the equations, it results that $\boldsymbol{\Delta k}$ must be an integer value of $2\pi$ and that it must lay on a cone in the direction of the translational vectors, satisfying all equations at once. Thus, it must lie within the intersection of three cones, which corresponds to the Ewald sphere. Therefore, for a diffracted beam to be formed it is required to have intersections with the sphere and the reciprocal lattice vector **G**.

Kinematic diffraction theory in comparison with Bragg's law includes the prediction of relative intensities. However, one of the large limitations of this model is that it only takes single scattering events into account. The model considers a crystal of finite thickness to calculate the scattering intensities. Electrons are charged particles that experience coulomb forces leading to strong scattering, and hence even for very thin samples, plural scattering events can occur and the intensity distribution predicted by the kinematic theory is incorrect. In the following section, the effect of having a non-primitive unit cell (i.e. more than 1 motif) will be addressed.

When considering a structure, all the atoms in the structure must be accounted for with atomic form factors based on the atomic placement within the lattice. Each atom will have an associated electron concentration $n_j$. Thus, each atom type will have a different scattering amplitude.

When the diffraction condition $\boldsymbol{\Delta k} = \boldsymbol{G}$ is fulfilled, the scattering amplitude for N unit cells is given by

$$F_{\boldsymbol{G}} = N\int_{cell} dV\,\rho(\boldsymbol{r})e^{-i\boldsymbol{G}\cdot\boldsymbol{r}} = NS_G \tag{2.14}$$

With $S_G$ defined as the structure factor over a single cell.

Writing the scattering density $\rho(\boldsymbol{r})$ as the superposition of the local scattering density $\rho_j$ associated with each atom $j$ within the unit cell. Considering $\boldsymbol{r}_j$ to be the position of atom $j$, then $\rho_j(\boldsymbol{r}-\boldsymbol{r}_j)$ defines the atom's contribution to the scattering density at a position **r**. Hence, the total scattering density at **r** due to atoms in a unit cell is

$$\rho(\boldsymbol{r}) = \sum_{j-1}^{s}\rho_j(\boldsymbol{r}-\boldsymbol{r}_j) \tag{2.15}$$

over the s atoms of the basis.

The structure factor is simply obtained by adding up each atoms contribution to the scattering, taking the phase into consideration. Since a crystal is periodic, then it only has to be performed for one unit cell. Now the structure factor may be rewritten over the s atoms in the cell:

$$S_{\boldsymbol{G}} = \sum_j F_j = \sum_j \int dV \rho_j(\boldsymbol{r} - \boldsymbol{r}_j) e^{-i\boldsymbol{G}\cdot\boldsymbol{r}} \tag{2.16}$$

Considering that it's only the position difference $\boldsymbol{r} - \boldsymbol{r_j}$ that matters, we can redefine it as **r'**. Now we can introduce the atomic form factor

$$f_j = \int dV \rho_j(\boldsymbol{r'}) e^{-i\boldsymbol{G}\cdot\boldsymbol{r'}} \tag{2.17}$$

The atomic form factor $f_j$ is an atomic property if the scattering density $\rho_j(\boldsymbol{r'}$ is an atomic property. This unique property must be considered for a basis containing more than one atom. It increases with atomic number Z, i.e. heavier elements will scatter more strongly.

Combining equations 2.16 and 2.17, the structure factor of the basis is written as

$$S_{\boldsymbol{G}} = \sum_j f_j e^{-i\boldsymbol{G}\cdot\boldsymbol{r_j}} \tag{2.18}$$

Using the Laue conditions, expressing $\mathbf{r}_j$ with relative coordinates $\mathbf{r}_j = x_j\boldsymbol{a} + y_j\boldsymbol{b} + z_j\boldsymbol{c}$, and inserting this into Equation 2.18, we get a new expression for the structure factor:

$$S = \sum_j f_j e^{-2\pi i(hx_j + ky_j + lz_j)} \tag{2.19}$$

In certain cases, the individual terms sum up to zero, resulting in no diffracted beams, commonly referred to as kinematical *forbidden reflections*.

Considering the basis of the fcc, a cubic cell, with identical atoms at 000; $0\frac{1}{2}\frac{1}{2}$; $\frac{1}{2}0\frac{1}{2}$; $\frac{1}{2}\frac{1}{2}0$. For this basis, the structure factor becomes

$$S(hkl) = f[1 + e^{-i\pi(k+l)} + e^{-i\pi(h+l)} + e^{-i\pi(h+k)}] \tag{2.20}$$

From the fcc structure factor, one observes that if all indices are even or odd, then S = 4f. Therefore, a diffraction pattern for a mixture of odd and even numbers there will appear no reflections for such indices. For diffraction patterns, this is essential to consider for indexing and calculation of crystal properties retrieved from the diffraction. It is important to be critical as in the event of dynamic scattering effects, some of the "forbidden reflections" might still appear in the diffraction pattern, e. g. when two allowed reflections are added up. For this dynamical scattering is necessary to describe multiple scattering events, which will not be discussed further in this section.

## 2.3 Ferroic materials

The objective of this chapter is to investigate the ferroelectric domain structure of KMWPO and KNBO. In this section, a comprehensive overview of ferroelectricity is provided, including both the microscopic and macroscopic behavior of typical ferroelectrics, as well as the necessary mechanisms to explain the emergence of ferroelectricity. Additionally, a brief overview of ferroelasticity is presented. The

focus of this thesis is on the ferroelectric and ferroelastic properties of KMWPO and KNBO; therefore, ferromagnetism is not discussed in this chapter. The fundamentals of ferroelectrics is based on the paper by Ping Shi. et al and the review paper by Catalan et al. [24, 25]. Moreover, details on ferroelectric mechanisms are based on a review papers by Brink and Khomskii [26].

### 2.3.1 Macroscopic Behavior of Ferroelectric Crystals

Ferroelectricity is a pheonomenon exhibited by certain materials that have a spontaneous electric polarization that is reversible upon application of an external field stronger than the coercive field, $E_c$. These materials are known as ferroelectric materials that exhibit reversible polarization displayed by the characteristics hysteresis curve, illustrated in Figure 2.7. Ferroelectric materials arise due to displacement of ions within the crystal lattice due to mechanisms that will be discussed in subsection 2.3.4, that occurs below a transition temperature known as the curie temperature. Upon transitioning into a ferroelectric at the transition temperature, the material transitions from a non-polar paraelectric phase into a polar ferroelectric phase, illustrated for $BaTiO_3$ in Figure 2.5. In the paraelectric phase, the material exhibit no alignment of dipoles, hence no polarization, in the absence of an external electric field. Within the ferroelectric phase, separate regions with a spontaneous polarization are formed, called ferroelectric domains. Ferroelectric domains are areas with oriented spontaneous polarization, randomly distributed between the equally probable polarities in the absence of an external electric field. Separating the ferroelectric domains there are the domain walls. Domain walls are boundaries of finite width separating domains with different orientation of the electric polarization. The ferroelectric and the paraelectric phase exhibits different symmetry, however the domain wall captures the symmetry of both the phases. Hence, the domain wall has different properties compared to the adjacent ferroelectric domains and can exhibit exciting properties.

Ferroelectric crystals split into multiple domains to lower the total free energy by reducing electrostatic energy originating from the spontaneous formation of polarization charge. Oppositely, the formation of domain walls cost energy and competes against the domain formation. Once the electrostatic energy is equal to the domain wall energy, the system reaches an equilibrium state and stabilizes. In general, through reducing the domain size, a larger volumetric fraction of domain walls results, increasing the domain wall energy contribution. Therefore, upon reaching equilibrium conditions, a stable domain size will be established. Furthermore, splitting into domains can for certain materials be strongly dependent on the direction within the material, the presence of defects, applied stress, or external fields.

Domain walls are often neutral, not carrying any bound charges as this is energetically costly. Such domain walls are electrically neutral, hence they are called neutral domain walls (NDW). However, ferroelectric domains can also carry bound charges screened by free carriers. Such domain walls, with a non-zero bound charge within the domain walls are called charged domain walls (CDWs). The difference between NDWs and CDWs depends on a variety of factors, including the orientation of the polarization direction, the presence of defects or impurities, and the external environment. In a perfect ferroelectric, neutral domain walls are created

between domain where the polarity is parallel to the domain wall, illustrated by the 180° domain wall in Figure 2.6. Oppositely, CDWs are domain walls can also occur where the polarity of ferroelectric domains creates an angle different than 90° in relation to the domain wall, resulting in a non-zero bound charge. Configurations in which the polarity is perpendicular to the domain wall is referred to as head-to-head (H-H) configuration or tail-to-tail (T-T) configuration. Depending on the configuration and the screening of free charges, one can distinguish between strongly charged domain walls (SCDWs) and weakly charged domain walls (WCDWs). For SCDWs to exist, screening is necessary as the electric fields produced by bound charges would create instabilities in the ferroelectric. WCDWs on the other hand are more stable and can exist without charge screening. However, in reality there are presence of defects and impurities that can lead to the formation of charged domain walls. The charged domain walls can alter the properties of the materials and the behavior of the domain walls.

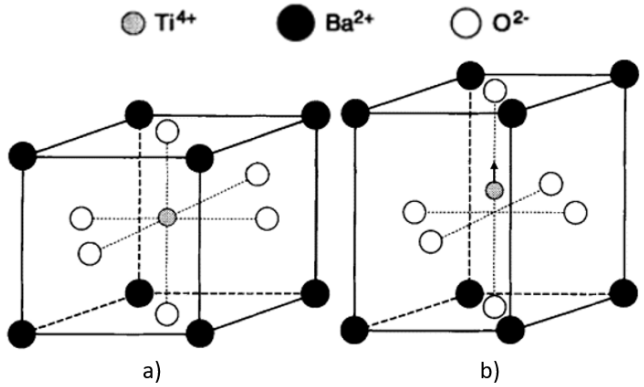


**Figure 2.5:** Illustration of Barium titanate ($BaTiO_3$) in its paraelectric phase (a) and in the ferroelectric phase (b). Upon transitioning into a ferroelectric phase $BaTiO_3$ changes from a cubic to a tetragonal structure. Due to its polarization being reversable upon application of an electric field, $BaTiO_3$ is consdered a proper ferroelectric.

The electric polarization direction of domains form at specific angles depending on the crystal structure, resulting in two or more polarities that are energetically and chemically equivalent. Dipoles localized inside ferroelectric domains find it energetically favorable to align, while it is unfavorable at a macroscopical level. Therefore, in the absence of an external field, no net macroscopic polarization is created. However, upon applying an external electric field, an electric dipole moment is caused within the material, causing ferroelectric domains to align along the direction of the electric field. Upon reversing the field, the ferroelectric polarization can be reversed if the field is stronger than the coercive field, $E_c$. This leads to a reorientation of the electric polarization in the opposite direction.

Upon applying an external electric field, the material responds differently depending on whether it being in its high- or low-symmetry state. In the paraelectric state, dipoles align weakly along the direction of the applied field. However, in the ferroelectric state the electrical polarization reorients between equilibrium states upon the application of an external field, polarizing domains to a higher degree in the direction parallel to the field. The response of a ferroelectric crystal to an

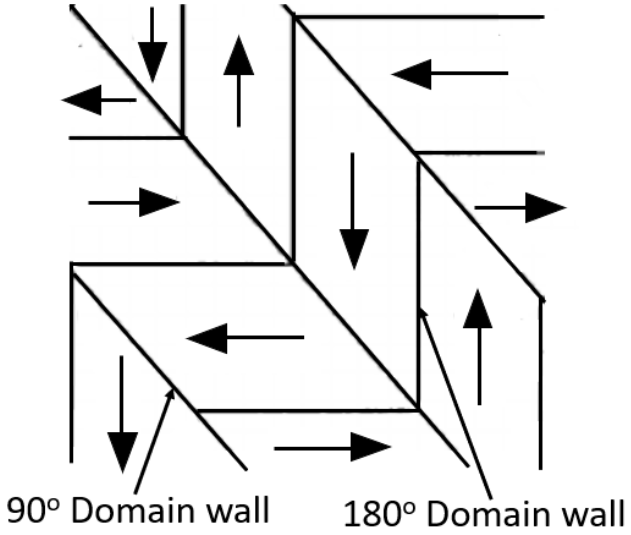


**Figure 2.6:** Schematic of domain wall configuration for a ferroelectric material. Arrows indicates the polarity of domains, while dark lines indicates domain walls, separating adjacent domains.

external field generates a characteristic hysteresis loop illustrated in Figure 2.7, showing a hysteresis loop. The switching of polarization is one of the most important characteristics of the ferroelectric state. For a paraelectric phase, the relationship between the polarization and the externally applied field is linear, while it is nonlinear for the ferroelectric phase. Before the application of an electric field, the net polarization is zero, starting at the origin of the figure. Once an electric field is applied, the polarization aligns gradually with the electric field until a saturation value for the polarization is reached for a given strength of the electric field. At this point, a further increase in the electric field just causes a stretching effect on the dipoles, giving no further increase in polarization. Once the electric field is removed, some domains switch polarity back to their original configuration, decreasing the total polarization until it reaches a stable value called the remnant polarization $P_r$. The remnant polarization is defined as the polarization that remains after the removal of the external field. Applying an electric field in the opposite direction will cause the polarization to gradually reorient and drop off until it reaches the saturation value in the opposite direction. Upon crossing the point with no net polarization, we have reached the electric field referred to as the coercive field $E_c$. The coercive field is defined as the necessary field strength required to neutralize the materials polarization. It describes the material's ability to withstand an external field without losing its polarization. If the coercivity for a given material is low it is called soft, whilst a material with high coercivity is called hard. The coercivity of a material is dependent on impurity concentration and strain and decreases with the increase of both.

### 2.3.2 Ferroelectric Domain Structures

To reach equilibrium states, the competition between electrostatic energy and domain wall energy of the crystal is essential to consider for the understanding of

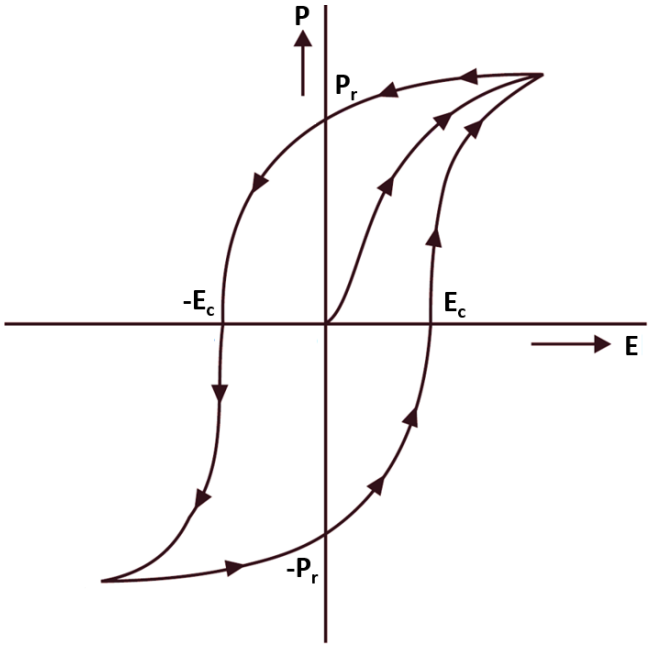


**Figure 2.7:** Illustration of the hysteresis loop for a ferroelectric material including the coercive field, $E_c$, and the remnant polarization, $P_r$. The maximum polarization achievable is the saturated polarization.

ferroelectric domain structures. For the theory, the model is limited to formation domains in ferroelectric thin films with anti-parallel domains separated by 180°. The problem of domain scaling was first analyzed by Landau and Liftshitz [27] and by Kittel [28], who proposed a model for the scaling laws of ferroelectric thin films. The law gives the proportionality between domain width w and the specimen thickness d in the polarization direction. The formation of domains can for a ferroelectric thin film be expressed through Kittel's law:

$$w = \sqrt{\frac{\sigma}{U} d} \tag{2.21}$$

where $\sigma$ is the energy density per area of the domain wall and U is the volume energy density of domains. The model described is only valid for anti-parallel domain structures, but the results provide useful predictions that are valid for most ferroic materials: the domain size decreases, resulting in an increasing fraction of domain walls, as the sample thickness decreases in the polarization direction. This is useful as it holds for most materials until the ferroelectric thin film reaches a critical thickness. Upon crossing the critical thickness, approximately when the domain width approaches the sample thickness, the model no longer gives correct predictions and the scaling law is no longer valid. Below this limit domain widths in some cases increase for decreasing thickness.

Kittel's law assumes the domain walls have a negligible thickness, whereas in reality, it has a finite thickness $\delta$. The thickness $\delta$ can be found from the equation:

$$\frac{w^2}{\delta d} = G \tag{2.22}$$

where the parameter G is weakly dependent on material classes, normally set

to be around 1.765. From this equation, it is possible to calculate the domain wall size given that the domain size is known.

Note that the validity of these equations is based on the assumption of anti-parallel domains separated with a 180° change in polarization direction for thin films.

### 2.3.3 Phase Transition and Landau Theory

Upon transitioning from the higher symmetry state at the paraelectric phase to a lower symmetry state at the ferroelectric phase, the material undergoes a structural transition. The transition between the states is characterized by a second-order transition for ferroelectrics, same as for the transition from normal conducting to superconducting materials. General transitions between states of a material are characterized by first order transitions. The distinction between the transitions is that for first-order phase transitions an abrupt change occurs in the system's order parameters, inducing an equilibrium state through releasing or absorbing energy in the form of latent heat to compensate for the entropy change. Second order transitions on the other hand, changes its order parameters, being the spontaneous polarization for ferroelectrics, continuously upon transitioning, involving no exchange of latent heat. To further explain this phenomenon, the Landau Theory of Phase Transitions is presented. The Landau theory describes the free energy of the material as a function of the order parameter, which is a measure of the degree of symmetry breaking in the crystal structure of the material

Landau realized that close to the Curie temperature, one can make an approximation of the free energy without calculating the microscopic states. This can be done as the order parameter can be approximated as close to negligible in the vicinity of the transition temperature. Therefore, it is possible to make a power series expansion of the free energy close to the critical temperature $T_c$ as a function of the order parameter, being the polarization P:

$$F(P;T,E) = -EP + g_0 + \frac{1}{2}g_2P^2 + \frac{1}{4}g_4P^4 + \frac{1}{6}g_6P^6 + \cdots \tag{2.23}$$

Where E is an external field. The coefficients $g_n$ are temperature dependent, and the odd powers of P disappear since the unpolarized paraelectric crystal in most situations has a center of inversion symmetry. Hence, the free energy is symmetric concerning the direction of the polarization. To find the equilibrium value of the order parameter given by the minimum of the free energy F, one minimizes the free energy with respect to the polarization.

$$\frac{\partial F}{\partial P} = 0 = -E + g_2P + g_4P^3 + g_6P^5 + \cdots \tag{2.24}$$

To arrive at a ferroelectric state it is required that the coefficient $g_2$ passes through zero at a temperature $T_c$. Therefore, $g_2$ can be expressed as $g_2 = \gamma(T - T_c)$ with $\gamma$ taken as a positive constant. Small values of $g_2$ indicate that one is close to the transition temperature, where the lattice is "soft" or unstable. The Landau free energy given for different temperatures is illustrated in Figure 2.8, showing the creation of local minima at a given polarization for temperatures below $T_c$, being the stable polarization state.

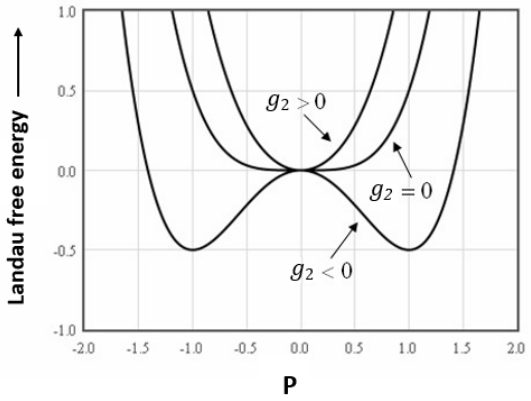


**Figure 2.8:** Landau free energy as a function of polarization for a second-order transition. For temperatures below $T_c$, the minimum shifts for larger values of P. For $T = T_c$ a discontinuous change occurs in the position of the absolute minima, for $g_2 <= 0$.

For temperatures above $T_c$, where $g_4$ is positive, nothing new would be added by $g_6$ since all coefficients would be positive, allowing its contribution to be ignored. Using a similar argument for temperatures below $T_c$, where there is a balance between the negative $g_2$ against positive $g_4$ and $g_6$, one can ignore its contribution. Thus, it is of unimportance for both cases and will be disregarded in further calculations. In the absence of an external field, equations 2.23 and 2.24 give an equation for the polarization at the minimum of the free energy:

$$P^2 = \frac{\gamma}{g_4}(T_c - T), \quad T < T_c \tag{2.25}$$

Since $\gamma$ and $g_4$ are both positive, then the polarization must be zero. This confirms that the phase transition is of second order since the polarization continuously approaches zero from both sides of the transition temperature.

Landau theory explains the phenomenological reason for the phase transitions in terms of the free energy of the material as a function of the order parameter. To understand what happens upon transitioning the curie temperature, it is necessary to elaborate on the mechanisms behind ferroelectricity. This will be considered in the following section.

### 2.3.4 Ferroelectric Mechanisms

The mechanisms responsible for the microscopic properties of ferroelectrics are more complex and are different depending on the crystal structure. It is necessary to present this theory for elaborating the ferroelectric mechanism of KNBO and KMWPO which will be explained through the literature review in sections 2.6 and 2.5.

Mechanisms for ferroelectricity can be divided into two sets of mechanisms. Firstly, order-disorder will be introduced as an individual ordering of ions. This is a consequence of structural displacement, creating ferroelectricity from the relative displacement of ions, making the centers of charge not coincide. The structural

rearrangement reduces crystal symmetry, creating a non-centrosymmetric polar state. Other mechanisms do not involve structural rearrangements, but rather a rearrangement of the ions from a disordered state to a non-centrosymmetric ordered state. Secondly, displacive types of ferroelectrics shifts the whole sublattice relative to the sublattice of a different type, making the centers of charge not coincide. Furthermore, there is a distinction between proper and improper ferroelectrics. In the Landau theory, the focus was on the change of the order parameter. If polarization is the primary order parameter for the transition, then it is a proper ferroelectric. Proper ferroelectrics show a distortion of the crystal that breaks symmetry giving rise to polarization. In the case of improper ferroelectrics, distortions generate polarization as a secondary effect. The mechanisms for proper and improper ferroelectrics are multiple. In general, there is made a distinction between five main mechanisms that will be reviewed briefly below.

Amongst the proper ferroelectric mechanisms, there is a hybridization interaction between the transition metal cation with its surrounding anions, leading to an off-centered displacement towards one or more of the anions. The mechanisms involve both the crystal's atomic and electronic structures, but also involve Coulomb interactions influencing the covalency of the cations. This is the mechanism of most conventional ferroelectric perovskite structures, such as $BaTiO_3$. Then there is the second mechanism for proper ferroelectrics being the lone pair mechanism. The lone pair mechanism consists of unbonded valence electrons, or so-called dangling bonds, with a high polarizability. The lone pairs are distributed anisotropically around the host ion, causing polarization through rehybridization.

Amongst the remaining three mechanisms for improper ferroelectrics, there is charge ordering ferroelectrics, where charge carriers are locally distributed anisotropically around the host ion, creating a non-centrosymmetric lattice. If both sites and bonds are inequivalent after undergoing a charge ordering, ferroelectricity can occur. The second mechanism is geometric ferroelectricity, being a displacive mechanism. Geometrical ferroelectricity is often due to rotations and tilting of anions, creating a net force that gives rise to structural instabilities resulting in polar distortions. This creates closer packing and a shift of the charge center resulting in geometrical constraints and size effects rather than changes in bindings. Lastly, there is magnetically induced ferroelectricity, where ferroelectricity occurs as a by-product from a magnetically ordered state. Through relativistic spin-orbit coupling, magnetic symmetry is projected onto the lattice inducing ferroelectricity. The magnetic order due to competing magnetic interactions breaks the inversion symmetry of the material, hence inducing an electric polarization.

### 2.3.5 Ferroelasticity

Ferroelastic materials is the mechanical equivalent of ferroelectrics, which describes the phenomenon where a material exhibits a spontaneous strain. Upon applying external stress to the ferroelastic material it will undergo a phase change to experience a structural deformation. Ferroelastic materials can therefore undergo mechanical switching, analogous to the polarization switching for ferroelectric materials. Similarly, ferroelastic materials display a characteristic stress-strain curve where a permanent reorientation can occur for two stable energetically equivalent oriental states of the ferroelastic material. The two states differ only slightly from

each other, and is therefore able to switch between the states through the application of a small uniaxial stress. The deformation that occurs from the uniaxial stress is possible due to the motion of dislocations or twin boundaries.

Ferroelastic materials are capable of existing in more than one orientation state simultaneously, giving the ferroelastic behavior. Because the orientational states are equally stable, the material does not transition back to the initial state when the stress is removed, forming domains of orientational states. Therefore, two adjacent ferroelastic domains can form a twinned ferroelastic domain wall. Within the field of ferroelastic domain walls, the lamellar twinning of ferroelastic domain walls is central [29]. Ferroelastic domains form to minimise local strain, at places where strain fields extend causing needle-shaped domains.

## 2.4 TEM

The theory presented in the following section is mainly based on the book by Williams and Carter [30] unless otherwise stated.

### 2.4.1 Microscope Setup

The TEM system consists of three main components: the illumination system, the objective lens and stage, and the imaging system. A schematic of a conventional TEM column is illustrated in Figure 2.9. The illumination system is comprised of the electron gun, and the lenses accelerating it and focusing it onto the specimen. This system is responsible for creating a parallel or convergent beam. The objective lens and the specimen stage system is the region where the beam-specimen interactions take place allowing for the creation and formation of images and DPs. The objective lens system is also an essential lens as it determines the quality of information from the specimen as this is where the beam-specimen interactions take place.

Lastly, the imaging system uses a lens system of multiple lenses to magnify the image or the DP produced by the objective lens and focuses it onto the viewing screen or via a detector, CCD, or TV camera. The magnifying lenses are commonly referred to as the intermediate and diffraction lenses and the final one is the projector lens. In addition, the system contains apertures that select or restrict which parts of the electron beam that contribute to the formation of the image or DP.

#### Electron Gun

The electron gun is located at the top of the electron column. Electron sources commonly used are thermionic emitters, field emitters, and Schottky emitters, each having their advantages and disadvantages. Thermionic emitters emit electrons overcoming the potential barrier upon thermal heating, field emitters emit electrons upon the application of a strong electric field to a sharp tip with a small radius. Lastly, Schottky emitters are electron guns that use a combination of thermal heating and electric fields applied to the tip, ultimately decreasing the potential barrier that electrons must overcome to be extracted. Most conventional TEMs are operated at acceleration voltages of 200 keV.

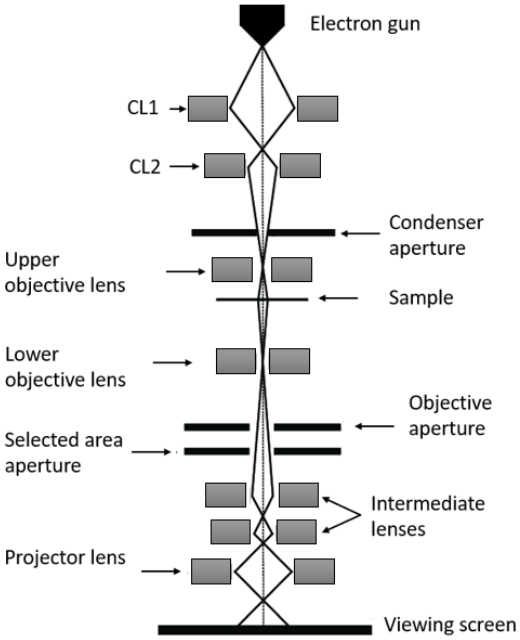


**Figure 2.9:** Simplified schematic diagram of transmission electron microscope with the electron beam travelling down the column.

### Electron Column

Following the extraction of electrons from the electron gun, there are electromagnetic lenses and apertures that converge or diverge the beam and control the convergence angle of the electron beam before it hits the sample. Condenser lenses, C1 and C2, together with the upper objective lens, C3 or c/o, and the condenser aperture decides the convergence angle and the beam-spread before it hits the sample. C1 mainly controls the brightness and spot size of the beam, while C2 and the upper objective lens are more important for the convergence angle. This allows the TEM to be operated using a parallel or a focused beam.

The objective lens and the stage are the heart of the TEM. The objective lens has an upper and a lower lens above and below the sample stage. The objective lens' role is to form the intermediate image and diffraction, which is subsequently magnified and projected by the imaging system. Diffraction patterns (DPs) are formed in the back focal plane, whilst images are formed in the image plane of the lower objective lens. By using the objective aperture in the back focal plane of the objective lens, it is possible to selectively choose the contributing electrons to create diffraction contrast. Inserting the selected area diffraction (SAD) aperture, it is possible to limit which area of the specimen contributes to the formation of the image or DP.

The imaging system consists of a series of intermediate lenses and the projector lens that magnify and focus the image plane or back focal plane onto the fluorescent screen or the CCD camera. One or more of these lenses can be active during the image formation, with one or more projector lenses commonly being turned off at lower magnification. For the DP formed in the back focal plane, the camera length is used as a measurement to indicate magnification. Camera length is defined as the distance from the specimen to the recording plane, the detector.

### 2.4.2 Aberrations

The illumination-system lenses suffer from lens imperfections, such as aberration and astigmatism. Limiting these aberrations is crucial to forming a small probe in STEM mode, but doesn't have the same limiting effects for the TEM operated by parallel mode.

One of the main lens aberrations that degrade the image quality is spherical aberration. Aberrations in the probe forming lens (C3) will affect the fine tuning of the minimum possible probe size. Spherical aberrations occur as a result of the difference in focus of the electrons depending on their distance from the optical axis. Electrons far away from the optical axis experience a stronger field than the ones close to the optical axis, hence they are deflected more strongly. This causes electrons near the optical axis to have a focus point further behind the lens than the electrons deviating more from the axis. As a result, airy disks are formed, which are intensity distributions that determines the resolving power of the instrument. This creates distortions in the image plane, limiting the ability to distinguish adjacent points. To reduce this effect, the condenser aperture is inserted, limiting the contributing electrons to the ones close to the optical axis through reducing the collection angle.

The effect of spherical aberrations can be partially compensated for by using a slight under focus, known as the Scherzer defocus, to achieve the best possible resolution. In modern TEMs, there are spherical aberration correctors that exploit non-round lenses to balance out and minimize spherical aberrations.

The other main lens aberration limiting the resolution is chromatic aberrations. This occurs when we have energy spread in the electrons originating from the electron gun. The energy spread is dependent on which type of electron gun is being used, with the FEG having the minimum energy spread. Since electrons are not fully monochromatic they are deflected differently by the electromagnetic lenses, causing a range of different focal lengths. This ultimately causes an intensity distribution in the image, which distorts the image.

Chromatic aberrations shows a different dependency on the collection angle compared to spherical aberrations, being less dependent on the collection angle. However, also chromatic aberrations are reduced by inserting a condenser aperture. In most cases, there is no need to correct for chromatic aberrations as this is not the limiting factor for the resolution, but when it is necessary, the resolution is increased by making the beam more monochromatic.

If the strength of lenses varies differently across the lens, the beam is affected by astigmatism. Astigmatism causes electrons not to be focused at the same spot, distorting the image in an elliptical manner. This problem arises as a consequence of the condenser aperture being misaligned or by contamination creating charge up, leading to a deflection of the beam. Astigmatism within the electromagnetic lenses is corrected for by lens stigmators which introduce compensating fields to adjust the shape of the beam to a round shape. Correcting for astigmatism is especially important for higher-resolution techniques.

There are several factors affecting the image or diffraction pattern quality that are important to compensate for or make correct alignments to minimize. It is therefore of great importance to correctly align the systems for collecting the best possible data.

### 2.4.3 Electron Interaction

As electrons are accelerated down the electron column and hit the specimen, the electrons can interact either elastically or inelastically with the sample. Elastic scattering involves little to no loss in energy. This type of scattering is prominent for thin samples and high energy and forms the main signal in both DP's and imaging. Inelastic scattering on the other hand is more interesting as it can originate from different processes and gives rise to various signals. Scattered electrons can be separated into coherently and incoherently scattered electrons. Elastic scattering is usually coherent, whilst inelastic scattering is incoherent. As the angle of scattering ($\theta$) increases, the degree of coherency generally decreases.

Electron interaction with the specimen is illustrated in Figure 2.10, showing how electrons scatter and dissipate their energy within the material, generating various types of signals that are exploited in different imaging techniques. Conventional TEM imaging mainly uses coherent elastic signals, while STEM uses incoherently scattered electrons. Incoherently scattered electrons give rise to phase contrast which can be utilized in imaging techniques with atomic resolution. In addition to the transmitted electrons, there are also the reflected or backscattered electrons, as well as the signals generated as a result of ionization, shown in Figure 2.10. X-ray signals on the other hand can be used for compositional analysis to obtain elemental information. The amount of each signal that is generated is highly dependent on the sample composition and sample thickness. Backscattered electrons and inelastically scattered electrons become more prominent for higher sample thickness. This is because it is affected by the atomic number (Z) of the elemental composition, which may affect the scattering cross section. In general, thin specimens favor elastic scattering compared to thicker samples that have an increasing fraction of inelastic scattering.

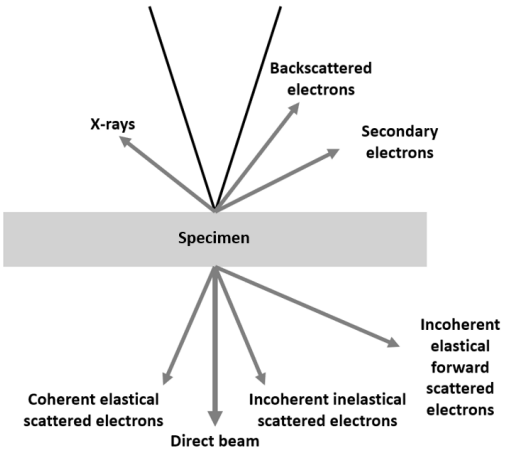


**Figure 2.10:** Simplified schematic diagram of the most important beam-sample interactions showing various signals generated from the sample.

#### Elastic scattering of electrons

Because of the Lorentz force, the electrons from the beam are scattered by the electric fields of the atoms. When considering scattering from single atoms, scat-

tering occurs as a consequence of interactions with the electron clouds surrounding the atom or the tightly bound nucleus. Depending on where the electron penetrates the electron clouds, the distance from the nucleus strongly affects how the electrons scatter. Low-angle coherent scattering, defined for angles $< 3°$, mostly originates from electron-electron scatterings while higher-angle incoherent scattering is mostly due to electron-nucleus interaction.

#### Inelastic scattering of electrons

Inelastic scattering, where the electron experience a loss in energy, gives rise to a range of characterization signals such as X-rays, secondary electrons, auger electrons, and incoherently forward scattered electrons. From the electron-sample interaction, the inelastic interactions can be separated into processes that generate electrons, processes that generate X-rays, or processes that result from collective interactions with atoms or electrons. X-rays can be continuous Bremsstrahlung X-rays or characteristic X-rays that can be used for elemental analysis through techniques such as Energy-dispersive X-ray spectroscopy. Inner shell electrons interacting with the incident electrons can be ejected from the atom leaving the atom ionized. Subsequently, an electron from an outer shell will fill its place releasing the energy difference as an auger electron or as a characteristic X-ray. These signals are characteristic and can be used to identify the transition which it originates from allowing for a more complete characterization.

There are as mentioned many advantages of using ionizing radiation. However, all the inelastic processes dissipate energy within the specimen, which might lead to beam damage if the sample is sensitive. If the sample is susceptible the beam might affect its structure and/or chemistry, depending on the tolerance. The processes causing damage to the material can be radiolysis, knock-on damage or sputtering, or general heating of the sample. These all occur at different rates depending on the acceleration voltage and material, but they can all occur within all voltage ranges.

### 2.4.4 TEM Techniques

As the signals generated from the sample exit the surface, adjusting the imaging system can make the back-focal plane or the image plane coincide with the object plane. Thus, acting in diffraction mode or imaging mode. The TEM can operate in a variety of imaging modes including the more common modes of broad illumination, such as imaging and diffraction mode. In addition, there are multiple modes in which the system uses apertures or changes the field strength in the lenses to achieve the desired information, giving a variety of different modes. One of the more advantageous modes that can be utilized in modern TEMs is the possibility to operate the microscope in its STEM mode. The STEM mode uses a focused electron probe to scan across specimen, allowing for a fine probe to scan over selected regions with the resolution limited by probe quality.

#### Diffraction in TEM

Diffraction patterns are formed when we send a parallel beam through a specimen, creating bright spots projected onto the screen with positions depending on the

Bragg's angles given by Equation 2.6 and the exclusion rules from Equation 2.18. This allows for certain **r** spacings in the diffraction patterns, giving structural information about the specimen.

For sufficiently thin samples, the patterns are mainly formed by kinematic scattering, mentioned in subsection 2.2.1, while dynamic scattering is mostly discarded as noise. If the crystal planes are oriented optimally relative to the incident electron beams, referred to as being on zone, an ordered array of spots appears. Illuminating large parts of the specimen gives rise to multiple patterns that are often not very helpful and hard to interpret. By inserting the selected area electron diffraction (SAED) aperture into the image plane of the objective lens, one places a virtual aperture at the plane of the specimen to select the area of interest that is to be illuminated. This is also beneficial as the intensity of the direct beam is reduced, avoiding damage or oversaturation of the CCD camera. By placing the back focal plane of the objective lens within the objective plane of the intermediate lens, one can represent the reciprocal space of the lattice produced by elastic scattering events.

In some cases, the specimen has a thickness allowing for a high number of incoherent scattering events in the forward direction. When this happens, incoherent electrons can have a scattering angle to another lattice plane hkl, where they have a probability to undergo scattering again. Upon reaching a thickness where a substantial amount of electrons experience multiple scattering events, dynamical scattering theory is required. In the case where the Kossel cone overlaps with the Ewald's sphere, lines called Kikuchi lines can form. Kikuchi patterns are discrete lines that can be used as an map for oriental mapping to find a specific zone axis, [UVW]. This is a useful tool when performing TEM orienting between different zone axes by tilting, making it easier to put the incident beam parallel to the zone axis.

### Bright-Field and Dark-Field Imaging

Bright-field (BF) and dark-field (DF) imaging are two of the conventional techniques used in TEM imaging. Upon capturing an image, the image plane of the objective lens is magnified and projected onto the detector which is amplified and displayed on a screen. By controlling the strength of the intermediate lens, the image plane is placed within the objective plane of the intermediate lens. Subsequently, the image is captured and displayed.

Bright field and dark field are complementary techniques that use the objective aperture to actively select which of the scattered electron reflections contribute to the formation of the image. Scattering may originate from and be affected by various factors, such as defects, strain fields, crystal grains, and boundaries between grains. The presence of scattering will generate contrast in BF and DF imaging. Bright field and dark field images are formed simply by selecting either the direct beam or one or multiple diffraction spots that contribute to the formation of the image by inserting the objective aperture in the back focal plane of the objective lens. By doing so one enhances amplitude contrast by blocking signals from certain scattering effects, which comes at the cost of removing the phase contrast. The result is high contrast images without much noise from nearby diffraction spots. Because of the amplitude contrast, BF and DF can be used for the inspection of

sample thickness and crystal orientation.

Upon capturing a BF image the beam around the central spot is selected by placing the objective aperture, such that the direct beam is chosen. In this way non-scattered electrons contribute to the image, making the regions that cause scattering appear dark, while the directly transmitted electrons are captured. This can allow for the inspection of thickness fringes and crystal orientation.

Centering the objective aperture around one or more reflection spots, excluding the direct beam, results in DF imaging. It is distinguished from BF by the fact that the contributing electrons are lower- and higher-order scattered electrons, making the regions causing the scattering to appear bright. The smaller the size of the objective aperture, the stronger the contrast in the image. In this way, diffracting planes and grain borders with a high density of defects may be distinguishable from the environment. Hence, DF imaging can be useful for identifying factors such as thickness variation, bending, crystal defects, strain, interfaces, and in some cases ferroic domain walls. In principle, the reflection should be centered at the optical axis by beam tilting to reduce aberration and astigmatism, referred to as centered DF. Centered DF is achieved by translating and tilting the beam for proper alignment with the optical axis down the column through the use of scan coils that deflect the beam.

In TEM imaging, BF and DF are two useful complementary techniques that are allowing for the identification of defects, interfaces and thickness variations. It may also be used for identifying structural changes across a border creating contrast where the crystal structure changes.

### STEM Imaging

The subsequent theory presented on STEM imaging and Lattice Imaging in subsection 2.4.5 below is based on the work of Rolf Erni titled *Aberration-Corrected Imaging in Transmission Electron Microscopy* [31].

In the STEM imaging, information about the specimen is obtained by scanning a fine electron probe across the specimen.The C1 lens determines the probe size, while the C2 is responsible for focusing the electron beam towards the sample in this mode. In the STEM mode, the upper pole piece of the objective lens is introduced as a third condenser lens, where the strength of the C2 lens is weakened and the upper objective lens operates at a stronger field than usual to focus the probe on the specimen surface. By inserting an condenser aperture, the electron beam is formed by a convergent semi-angle $\alpha$ which is much larger than in conventional TEM. The probe is effectively focused by the condenser system, with the upper objective lens operating at a stronger field than usual, to converge the beam onto the specimen.

To capture an image, the electron probe is scanned across the specimen using scan deflection coils. At each scan position, a site-specific pattern in a diffraction plane can be recorded as the intensity from a detector. This can be registered to create a two-dimensional array of data points that can be used to relate a position to an x- and y-coordinate. The scan coils can thus relate each data point to a given scan position, where the resolution depends on the probe size and the scan step size. The magnification is determined by the scan step size, with smaller steps giving a higher magnification. Where the settings above the

specimen determines what is scanned, the setup below the specimen determines what information is recorded. It primarily depends on the size, shape and position of the detector. What part of the diffraction plane falls on a specific detector can be controlled by the intermediate lenses. If a round detector around the optical axis is used at a high camera length, the recorded intensity is mainly the direct beam, but due to high convergence angle there is an overlap between the direct and the diffraction beams that can contribute. This is BF STEM and the contrast is similar as observed in BF TEM (see section 2.4.4) Due to scanning noise and slower recording, BF STEM has added limited value to BF TEM.

If an annular (ring) detector is used which starts at a higher scattering angle (typically $> 50$ mrad) and the detector is large, the intensity of unrelated scattering events is summed up over a angular range. Incoherent imaging is complementary to coherent imaging, and is what forms for example DP (subsection 2.2.1), as illustrated in Figure 2.11. Electrons scattered to these angles will have higher intensity if the specimen is locally thicker or if the electron is scattered by higher atomic numbers (Z). Thickness can give shape information, while at a given constant thickness, it gives Z-contrast. Intensity can for high-angle electron scattering be described by Rutherford scattering, characterised by a $Z^2$ dependency. However, due to screening phenomena this is closer to an exponential dependency of 1.6-1.8 instead of 2. For these angles, high-angle annular dark-field (HAADF) STEM becomes a useful imaging technique because of the incoherent nature of the scattered electrons and its relative easily interpretable contrast.

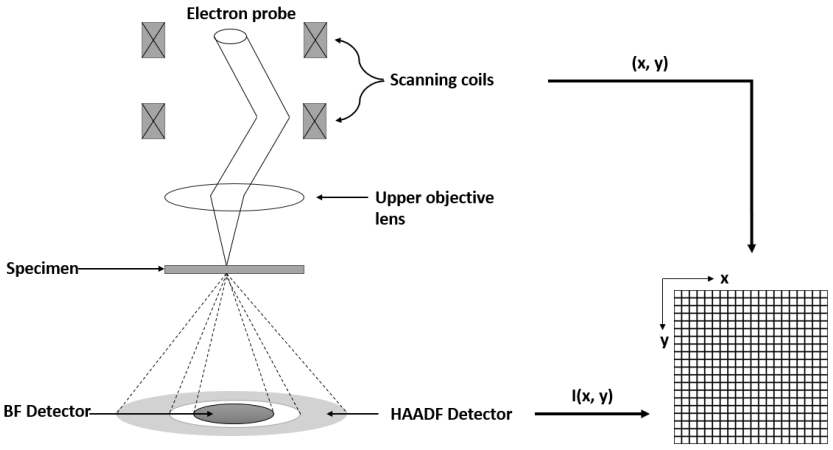


**Figure 2.11:** Scanning the electron probe across the specimen by the use of two pairs of scanning coils, that applies an electric field to deflect the electron beam to scan across the specimen. Each scan position is registered as a position (x, y), and the relative intensity of each point is collected by the use of different detectors, here BF and HAADF is shown. Thus the intensity is collected as a function of position I(x, y) onto a pixelated grid.

Note that if techniques such as energy dispersive X-ray spectroscopy (EDX), electron energy loss spectroscopy is used, the detectors are 2D pixelated detectors instead of discs or rings, where for each beam position a diffraction pattern is recorded (4D-STEM). These techniques can be used for compositional mapping and give electronic structure information. In addition, the ring detectors can

be divided into segments. When combining signals from several detectors, the signals can give multidimensional data sets. Postprocessing signal handling is often required to extract information. In this work HAADF STEM is the main used STEM based technique.

### 2.4.5 Lattice Imaging

TEM allows for high spatial resolution in both static broad beam mode (TEM) and scanning mode (STEM). Diffraction is based on a regular configuration and with SAED it is limited to approximately 100 nm in area. The question is if the spatial resolution is enough to directly image the atomic lattice and potential defects, such as dislocations, stacking faults or interfaces.

Understanding the structure of materials at the atomic scale is essential for developing new materials with desired properties. Lattice imaging with atomic resolution provides valuable information about the structure, defects, and interfaces of materials. Two powerful techniques used to achieve this are High-resolution TEM (HRTEM) and High-resolution STEM (HR STEM) are two fundamental and commonly used techniques for lattice imaging with atomic resolution. However, there are some differences between the two methods in terms of their image formation and the way they spatially image the lattice structure.

HRTEM, also known as phase contrast imaging, involves illuminating the specimen with a broad beam parallel to the optical axis. Upon transmission of a zone-axis oriented crystalline specimen, the beam is diffracted in a way determined by the structure factor of the crystal with each scattered beam being shifted by a specific phase shift. A post-field below the specimen is created by the objective lens and focuses all transmitted and scattered beams to the back focal plane which are transferred to the image plane where the beams interfere and form an image. In the following explanation, the inelastic interactions and absorption is neglected, such that one can assume that the specimen is a weak-phase object that alters the phase of the waves, but not their amplitudes.

Upon recording the wave intensity the phase information is lost. Therefore, it is not possible to detect how the phase modulation alters the intensity of the image. To account for the phase modulations effect, it is required to be able to represent it as an amplitude modulation. The technique commonly used to do so is known as the *phase contrast method*. This theory was originally developed for optics, but is applicable for electron microscopy.

In transmission electron microscopy the phase contrast transfer is dependent on the characteristic of the post-field of the lower objective lens. How the exit-field is transferred in the phase contrast transfer determines a substantial amount of the information contained in the atomic-resolution image. The information transfer in HRTEM is thus dependent on a number of factors such as aberrations, limited coherence of the beam, stability issues such as mechanical instabilities and drift, and incoherent contributions. In addition, extra phase shifts induced by defocus and spherical aberrations in the post-field of the objective lens can create contrast. This ultimately determines how the relative phase shifts between the diffracted electrons are transferred to form an image, illustrated in Figure 2.12. The final result for the information transfer can be described by the phase contrast transfer function (PCTF), given by Equation 2.26.

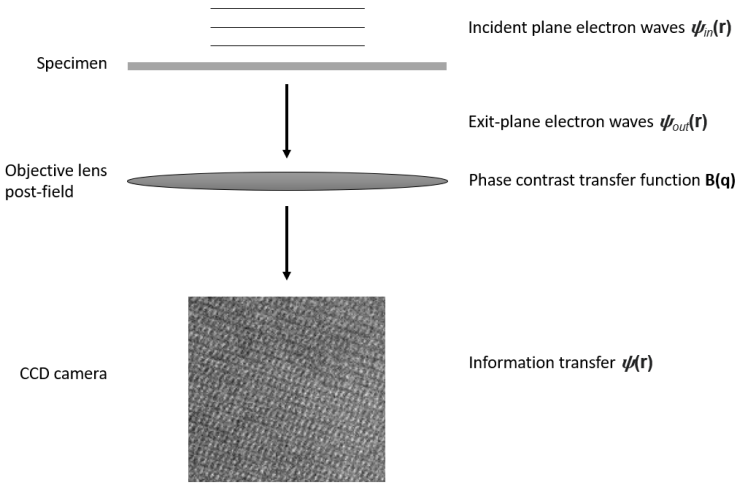


**Figure 2.12:** The information transfer through the electron column in TEM. The process is given for HRTEM imaging with the phase contrast transfer function B(**q**). The HRTEM image is taken of KMWPO.

$$B(q) = sin(\chi(q)) = sin(\frac{1}{2}\pi\lambda^3 C_s \cdot q^4 + \pi\lambda\Delta f \cdot q^2) \tag{2.26}$$

Where $\Delta f$ is the defocus, while $C_s$ is the spherical aberration coefficient. The phase contrast transfer function is a function of the parameter q, being the spatial frequency. An aberration-corrected TEM would depend on more parameters, which are considered negligible for an uncorrected TEM which the equation is given for. In addition, HRTEM is sensitive to sample thickness, crystal orientation, and detector geometry which affects the resolution and the contrast of the image. Hence, PCTF describes how the contrast in the image is created by the additional phase shifts induced on the exit-wave by the post-field of the objective lens. There is a point value q after which the contrast can invert, making interpretation of the contrast difficult, but the spatial resolution better. By choosing an optimal defocus, known as the Scherzer defocus. The Scherzer defocus for electrons accelerated at 200 kV, when $C_s$ = 1 mm, is given by $\Delta f$ = -58 nm, which is illustrated in Figure 2.13. In this way, one can partially compensate for the fixed spherical aberrations to reach the optimal contrast. However, caution is required when interpreting HRTEM images as the interference can cause contrast to vary depending on the value of the PCTF. A negative value gives positive contrast, meaning that atoms appear dark on a bright background and vice versa. Therefore, interpretations should always be supported by complementary data and image simulations.

HR STEM imaging was explained above in section 2.4.4 for an electron probe being scanned over an area by the help of scan coils to give a two-dimensional array of data points that are registered by detectors and transferred to a pixelated grid to create an image. For this imaging technique, the probe size is decisive for the resolution, where a smaller probe results in a better lateral resolution. Therefore, this mode is highly dependent on the probe formation, i.e. the pre-field of the objective lens, contrary to HRTEM which depends on the post-field of the objective lens. However, the lenses have the same limitations, so the minimal

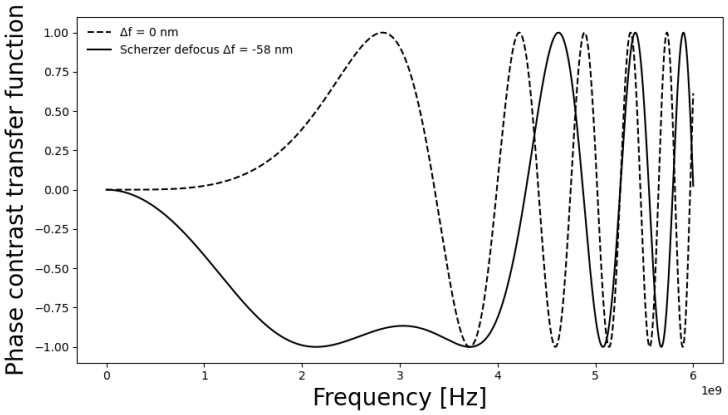


**Figure 2.13:** Phase contrast transfer function B(q) according to eq. 2.26 for a TEM operating at 200 kV with $C_s = 1$ mm. The function is shown by the dashed line for defocus $\Delta f = 0$ and by the black line for Scherzer defocus $\Delta f$ = -58 nm. The ideal contrast value is close to $\pm 1$ over large areas and spread. Note that damping terms given by envelope functions are not included.

probe size depends on the same aberrations (defocus and spherical aberrations). In addition, there is an effect of the energy spread within the probe and stability issues. If the electron beam is focused such that it reaches a probe size smaller than the the atomic spacing and a scan step smaller than atomic spacing is used, it can directly reveal the atomic distances of the crystal. STEM imaging is therefore determined by the quality of the probe formed by the condenser lens system. For these techniques it is advantageous having a FEG for characteristics such as high brightness, high spatial and temporary coherence, small virtual probe size and the degree of monochromaticity, as well as having a high enough semi-angle $\alpha$ to get overlap between diffraction disks.

We get information from local position of the probe. What intensity is recorded depends on the detector selected. Here the incoherent HAADF STEM signal has the advantage of being easily interpretable over the BF STEM signal which is coherent. The HAADF detector measures the total intensity scattered onto the detector that stretches over a certain range of angles. For each pixel, the intensity of inelastically scattered electrons is measured as a function of position. The angular range from which the electrons are selected are determined by the size of the annular detector as well as the camera length L, the effective distance by which the diffraction pattern is projected from the specimen onto the detector. For high angles the coherence effects is averaged out, such that the signal is essentially incoherent. In this mode, the scattering is dominated by Rutherford scattering, yielding images that are highly affected by atomic number Z, commonly referred to as Z-contrast imaging. STEM HAADF images is therefore capable of imaging the Z-contrast at atomic resolution, with higher atomic Z number appearing as brighter due to the increased scattering effect. This allows for a direct interpretation of images in terms of atomic positions, as well as the Z-contrast.

The main differences between the techniques in terms of imaging the lattice structure lies in the way the image is formed, i.e. static parallel beam vs fine

scanning probe and the nature of the signal. In HRTEM the image is formed by the diffraction pattern from relative phase shifts, which contains information about the crystal lattice and can easily reveal details such as crystal defects, grain boundaries, and stacking faults. In contrast HRSTEM forms an image based on the scattering intensity of the electrons for each given probe position on the specimen to form an image. Each scanning point produces a site-specific diffraction pattern dependent on the scattering power of the atoms in the sample, as well as the thickness. For this imaging technique, the probe size is decisive for the resolution, where a smaller probe combined with small scan steps result in better lateral resolution.

## 2.5 Literature Review KMWPO

Since its discovery in 1993 by A. Wostrack (unpublished), there has only been produced a handful of published articles on $K_2MgWP_2O_{10}$ (KMWPO), despite its interesting ferroic properties. From literature it becomes clear that many of its properties are as of now not fully understood, as there is a lack of studies at high spatial resolution. Therefore, many questions about its crystal structure and ferroic properties at a nanometre resolution are yet to be determined. For this, TEM inspection of the material would be suitable characterisation tool as there are no previously published TEM studies of KMWPO available.

In the following chapter, relevant structural properties of KMWPO will be presented to understand how its phyiscal properties are related to the crystal structure. This works as a brief summary of the handful of published articles with a focus on its structural and ferroic properties. In general, there is a high degree of agreement on published studies of the crystal structure and ferroic properties of KMWPO.

### 2.5.1 Crystal Structure of KMWPO

KMWPO crystallize into a tetragonal crystal at 1068K into its high-temperature phase with space group $P4_12_12$ [32, 33, 34]. Under cooling it undergoes a series of phase transitions seen in Equation 2.27, altering its crystal structure. In its room temperature phase, denoted $\varphi$, which will be the focus of this thesis, the crystal structure is characterized as a triclinic structure with space group P1 [32, 34, 35]. Using X-ray powder diffraction by the Rietveld method Peuchert *et al.* characterized the structure to be the triclinic P1 structure with lattice parameters $a = 9.141$Å, $b = 9.160$Å, and $c = 10.736$Å, with interaxial angles $\alpha = 90.28°$, $\beta = 90.52°$, and $\gamma = 90.11°$ [32]. There appears to be no contradicting published articles stating otherwise on the crystal structure of KMWPO as far as the author can confirm.

$$\boldsymbol{\alpha} \xrightarrow{1068K} \boldsymbol{\beta} \xrightarrow{782K} \boldsymbol{\gamma} \xrightarrow{637K} \boldsymbol{\delta} \xrightarrow{537K} \boldsymbol{\epsilon} \xrightarrow{535K} \boldsymbol{\phi} \xrightarrow{436K} \boldsymbol{\varphi} \tag{2.27}$$

From Figure 2.14 KMWPO is illustrated for its room temperature phase, showing projections along its crystallographic axes. The crystal structure is characterised by a helical chain of alternately linked [$WO_6$] and [$MgO_6$] octahedras connected by the corners and oriented along the $c$-direction. These helical chains are

further connected via a slightly distorted phosphate tetrahedra to form a three-dimensional network. Within the three-dimensional network large prismatic cavities are formed with two close to equivalent positions, which the potassium atoms can occupy. In its different phases, the potassium atoms can preferentially occupy one or both of the positions. For both positions the ions are surrounded by 13 oxygen atoms, making their environment close to equivalent unless the structure is distorted [36].

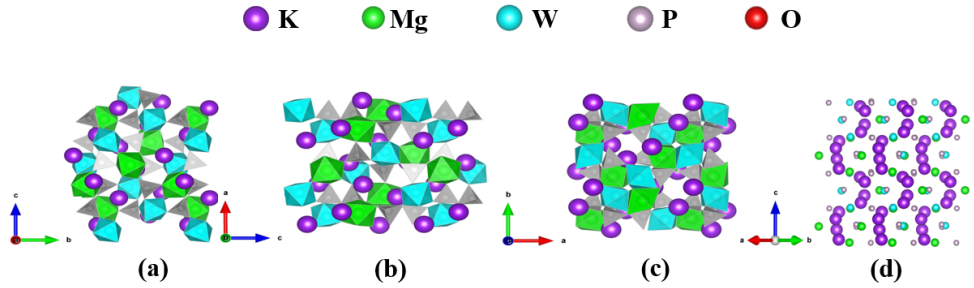


**Figure 2.14:** Projection of KMWPO crystal structure along its crystallographic axes (a-c) and oriented along the [110] zone axis (d) showing the characteristic alternating chains of W and K atoms. The image is visualized by VESTA [37], and allows for the identification of structural units, such as the alternating chain of $[WO_6]$ and $[MgO_6]$ octahedras linked along the *c*-direction. The KMWPO structure displays no symmetries in any directions.

Upon transitioning from the high temperature phase with space group $P4_12_12$ to the room temperature phase with polar space group P1, the crystal goes through multiple order-disorder and/or displacive driven phenomena that involves ionic motion along the tunnel formed by prismatic cavities, tilts and weak distortions by the $[PO_4]$, $[WO_6]$, and $[MgO_6]$ groups. The end result is the room temperature phase with a slightly distorted triclinic pseudo-tetragonal modification, mostly affected by the motion of potassium ions within the rigid network [34, 38]. Going into the room temperature phase, the potassium ions goes into a symmetrically independent state with a preferred position within the cavities.

### 2.5.2 Ferroic Properties of KMWPO

KMWPO is considered to be both ferroelectric and ferroelastic, displaying multiferroic properties below 537 K [32, 36, 38]. In the room temperature phase, KMWPO has a non-centrosymmetric crystal structure, giving a spontaneous polarization direction that has not been fully described in literature, due to the lack of symmetries in the crystal structure. However, twinning domains have been reported for KMWPO by Peuchert *et al.* [36] for temperatures below the transition temperature 537 K, exhibiting a complex twinning configuration. The twinning domains disappears above this temperature due to the tetragonal symmetry of the high temperature phase at which a uniaxial single-domain phase is formed [34]. Polydomain twinning of the crystal below 537 K is visible using PLM down to room temperature. Twinning domains gradually change through the phase transitions in conjunction with the loss of symmetry. At room temperature, the twin

domains are parallel to (100) and (001) directions with the domains being poorly spatially resolvable [39]. Domain boundaries tend to have blurred domain boundaries, ranging between 5-100 um in width, with overlapping in all directions. The ferroelasticity of KMWPO can be displayed by inducing an external force on the crystal, causing ferroelastic domains to become notable through folding processes of individual domains. Upon cooling down to room temperature, the loss of symmetry creates eight possible triclinic energetically equivalent orientational states. Despite this, no previous work have been performed on the characterization of the twinning domains at a higher spatial resolution than with PLM.

KMWPO has been reported to be a ferroic material due to its transition into a polar space group shown through dielectric measurements and ionic conductivity [32, 36]. Going through five transitions, three of which significantly reduces its crystal symmetry from its high temperature tetragonal phase through spontaneous deformation changing its material properties. In its room temperature phase, KMWPO has a non-centrosymmetric distorted triclinic pseudo-tetragonal crystal structure. Previously, authors have published Brillouin scattering studies to investigate the phase transition mechanisms of KNBO. However, no attempts have previously been made on characterising its ferroic mechanisms nor domain structure using TEM as far as the author can confirm. Hence, it is of great interest to investigate how its physical properties are related to the crystal structure by using a correlated microscopy study.

## 2.6 Literature Review KNBO

Since its discovery in 1977 by Choisnet *et al.* [40], there has only been a limited number of published articles on $K_3Nb_3B_2O_{12}$ (KNBO), despite its highly interesting ferroic properties. From literature, it becomes clear that many of its properties are as of now not fully understood, as conflicting results are reported on the fundamental properties of the crystal structure. With only a handful of published articles, some open questions about its crystal structure and ferroic properties resides that are still to be determined.

In the following chapter, structural properties of KNBO will be presented to understand how its physical properties is related to the crystal structure. This is followed by a summary where the ferroic properties are outlined, together with disagreements with the current assumed structure of KNBO. Lastly, a brief review of previous TEM studies will be presented, which this work serves as a continuation based on recent publications.

### 2.6.1 Structural Properties of KNBO

KNBO crystallize into hexagonal shaped crystals at 783K as the $\alpha$ phase with space group $P\bar{6}2m$ [41, 42, 43]. Under cooling it undergoes a series of phase transformations that can be seen from the transitions in Equation 2.28, altering its crystal structure. In its room temperature phase, denoted $\epsilon$, which will be the focus of this thesis, the crystal structure is characterized as a orthorhombic structure with space group $P2_1ma$ [43, 44, 17]. This was originally believed by Choisnet *et al.* to have a trigonal crystal structure with space group $P31m$ [40], but was later corrected by Becker *et al.* in 1995. Using Buerger precission X-ray

diffraction (XRD), Becker *et al.* characterized the KNBO crystal structure to be the orthorhombic structure with space group $P2_1ma$ with lattice parameters $a$ = 17.506Å, $b$ = 15.162Å, and $c$ = 3.968Å [43]. KNBO has a pseudo-hexagonal shape in its $\epsilon$ phase, originating from the small distortion of 0.01% between the orthorhombic cell and the hexagonal cell [44]. Therefore, crystallographic directions are commonly defined using pseudo-hexagonal axes. This can be interpreted from the illustration in Figure 2.15.

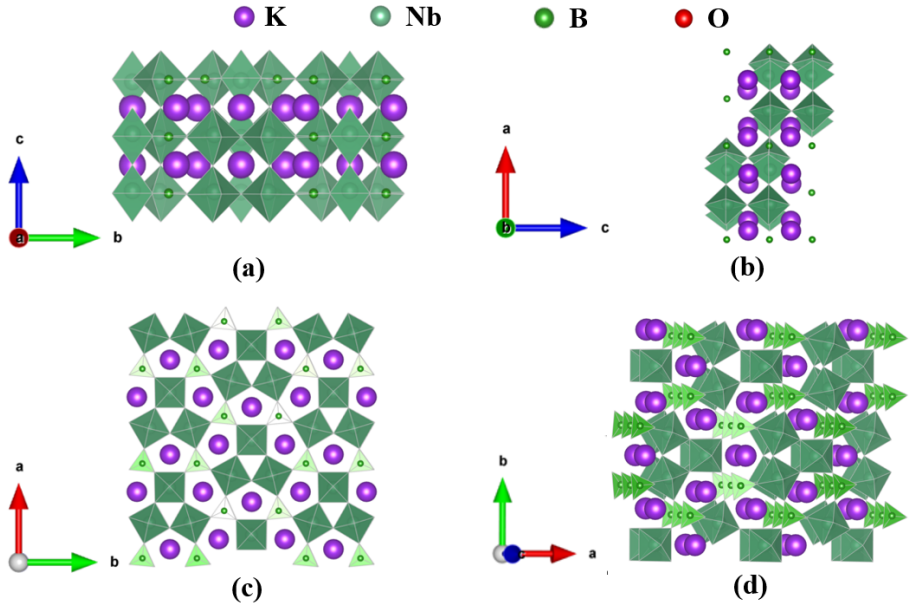


**Figure 2.15:** Projection of KNBO crystal structure along its crystallographic axes (a-c), and (d) a slight tilt from the $c$-axis. The image is visualized by VESTA [37], and allows for the identification of structural units as well as their symmetries, described by space group $P2_1ma$.

$$\boldsymbol{\alpha} \xrightarrow{783K} \boldsymbol{\beta} \xrightarrow{743K} \boldsymbol{\gamma} \xrightarrow{693K} \boldsymbol{\delta} \xrightarrow{383K} \boldsymbol{\epsilon} \xrightarrow{190K} \boldsymbol{\phi} \xrightarrow{178K} \boldsymbol{\varphi} \tag{2.28}$$

From Figure 2.15, KNBO is illustrated for its room temperature $\epsilon$ phase, showing the different crystallographic orientations. The crystal structure is characterised by $[NbO_6]$ octahedral chains connected through $[BO_3]$ triangles. The $[NbO_6]$ chains are connected by sharing two O atoms at the equatorial plane via their common corners, forming triangular prisms. This results in the formation of 2D layers close to parallel along the $c$-axis. The sheets are linked in the a-b plane, with spaces between $[NbO_6]$ octahedras and $[BO_3]$ triangles forming pentagonal cavities. The pentagonal cavities are occupied by the potassium ions, which are shifted to give a spontaneous polarization in the $P2_1ma$ structure [42].

Upon transitioning from the high temperature $\alpha$ phase with space group $P\bar{6}2m$ to the room temperature phase with polar space group $P2_1ma$, the crystal structure is altered by order-disorder driven phenomena that involves shifts of the potassium ions and smaller distortions of the $[NbO_6]$ octahedra [42]. In its room temperature phase, KNBO displays a neutral $2_1$ screw axis along the $a$-axis, a mirror plane along the $b$-axis, and an $a$-glide plane along its $c$-axis. Inspection of Figure 2.15 allows for the identification of the mentioned symmetries.

### 2.6.2 Ferroic Properties of KNBO

KNBO is considered to be both ferroelectric and ferroelastic, displaying multiferroic properties below 783 K with a spontaneous polarization along the $a$-axis. KNBO exhibit ferroelastic twinning domains that can be observed in Figure 2.16, with the common ferroelastic needle-like structures [45]. Twinning domains were suggested to go parallel to the $10\bar{1}0$ and $11\bar{2}0$ [46], forming angles of 120° in relation to other domain orientations. The domains, which are mobile under the application of mechanical force, have a twinning axis along the $c$-axis, showing six possible orientations of the ferroelastic domains [43].

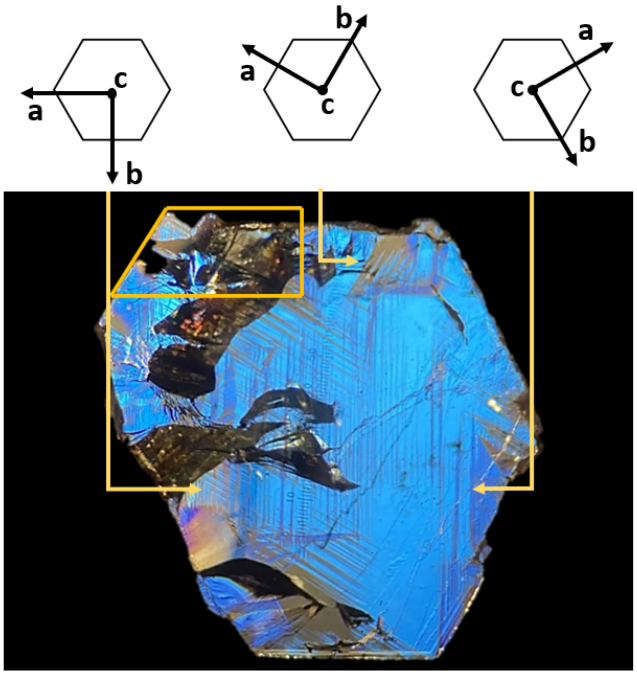


**Figure 2.16:** KNBO exhibiting ferroelastic (and ferroelectric) behavior at room temperature, displaying three different twin domains with the twinning axis $c$, being the facet of the crystal. In the lamellae structure captured with PLM the three twinning axes are highlighted by needle-shaped domain forming angles of 120° in relation to each other. Their relative orientations is illustrated above with pseudo-hexagonal axes. The enclosed area in the upper corner of the crystal marks the area from which the TEM specimen was produced.

KNBO have been suggested to exhibit ferroelectric properties, with a spontaneous polarization along the $a$-axis. This is unveiled from dielectric properties and Brillouin studies through interacting mechanisms of polar ordering [46, 47]. The polar $a$-axis will be assumed throughout this project, despite contradicting publications which will be elaborated on in the subsubsection 2.6.2.1. In addition, KNBO has been reported to exhibit antiferroelectric response by Shan *et al.* [17, 18] through measurements of a double hysteresis loop along the c-axis in P-E curves. Performing a local dipole analysis, using the bond-valence method, Shan *et al.* suggested that the KNBO crystal showed antiparallel sublattices along the $c$-direction. This complicates the current structural model as an absence of a hysteresis curve along the $a$-axis has been demonstrated by Shan *et al.*. However,

in the same paper a polar displacement involving potassium and niobium ions was found along the $a$-axis through the use of its non-linear optical properties.

#### 2.6.2.1 Contradictions With the Current Structural Model

The inconsistent reports on its physical properties have caused contradictive arguments in the scientific community on the real crystal structure of KNBO. The ferroic properties are not fully understood, with contradicting reports on many of its physical properties. This have caused speculations around its space group in its room temperature phase, determined to be $P2_1ma$ [41, 42, 43]. Amongst the reports challenging the structural model, there is Maczka *et al.* whom reported transverse acoustic modes for KNBO that are forbidden for orthorhombic crystal structures [42, 47]. Furthermore, KNBO have displayed superionic properties due to the mobility of potassium through the interstitial cavities along the $c$-axis. Hence, researchers have suggested that the true polar axis is the $c$-axis. Based on this and the indications that the symmetry of the crystal structure is no higher than orthorhombic, it has been suggested that the real crystal structure of KNBO is monoclinic or triclinic, rather than orthorhombic from recent publications [48, 49].

There has also been reported structural discrepancies with the suggested structural model of KNBO. It has been emphasized by other authors that the suggested spontaneous polarization is not in agreement with the $P2_1ma$ symmetry and therefore that the symmetry is not completely determined [48, 49]. Contradicting publications have stated that the true spontaneous polarization direction of KNBO is the $c$-direction. This was based on Brilluoin scattering and conductivity studies [42, 47]. Furthermore, statements saying that KNBO exhibit superionic conductivity along the $c$-axis has been put forward [46, 47, 48, 49]. This further supports the suggestion that the true polar axis of KNBO is the $c$-axis. However, this is not in agreement with the proposed space group, which have been repeatedly reproduced as space group $P2_1ma$. No alternative space groups have for this reason been put forward, leaving open questions regarding the crystal structure and the true polarization direction.

### 2.6.3 TEM Studies on KNBO

There have previously been performed three TEM studies of KNBO to the authors knowledge. The first TEM study was performed by Ryggetangen [50], whom demonstrated the $6mm$ symmetry in SAED patterns as well as showing the $3m$ symmetry in on-zone CBED patternss with zone axis [001]. These $3m$ mirror planes extended along the [100], $[\bar{1}20]$, and $[\bar{1}\bar{2}0]$ directions. Off-zone CBED patterns revealed two mirror planes along the directions [100] and [010]. Not in agreement with simulations, displaying a single mirror line along the [100] direction.

The two remaining TEM studies have been performed by Linnerud [51, 52], whom successfully reproduced the results of Ryggetangen. However, the off-zone CBED patterns revealed similar 3m symmetry as the on-zone patterns with mirror planes along the [100], $[\bar{1}20]$, and $[\bar{1}\bar{2}0]$ directions. Additionally, Linnerud produced procedures for domain wall investigation using HAADF STEM as well as creating a

framework for domain inspections at the atomic scale. Low-angle grain boundaries with a 0.6° rotation of the crystal structure was reported with the suggestion of being two antiferroelectric domains or two sub-grains. Structural 120° twin domains was successfully characterised with lattice resolution, confirming that the *c*-axis is the twinning axis for KNBO. Measurements suggest that the minoriy of the antiferroelectric twinning domains being charged twinning domains, i.e. a charged H-H configuration and an uncharged T-T configuration. Therefore, a high-resolution HAADF STEM inspection of the domain structure using the framework established by Linnerud could disclose interesting details on the CDW functionality.

CHAPTER

# THREE

# EXPERIMENTAL METHODS

The success of any TEM study relies heavily on the quality of specimen preparation. In this project, the primary objectives are to give a general characterization of KMWPO and inspect charged H-H domains of KNBO using TEM. Thus, this chapter outlines the experimental techniques utilized in the project, with emphasis on the specimen preparation further based on the previous work of the author [21]. The chapter is organized into two main sections, detailing the specimen preparation procedures used for KMWPO and KNBO. As these materials require different degrees of accuracy, somewhat separate procedures were employed. Following this, the chapter describes the TEM imaging techniques employed for material characterization. Lastly, the data processing procedures are presented, along with a brief overview of the correlated microscopy techniques, including polarized light microscopy (PLM) and piezoresponse force microscopy (PFM).

## 3.1 Material Synthesis

The synthesis of high-quality single crystals with a known crystallographic orientation is crucial for the research within material science. In this report, two different single crystals are used for specimen preparation, each with a known crystallographic orientation. The crystals were both grown using high-temperature growth methods with precise control over crystal growth parameters. The synthesized crystals serves as the basis for the investigation into their interesting material properties to both KMWPO and KNBO.

### 3.1.1 Crystal Growth KMWPO

Crystal growth was performed by using a modified *Nacken-Kyropoulos* technique from a stoichiometric melt [36]. Starting at 1120 K, the melt was placed a platinum crucible where it was kept for 1 day. A precisely oriented seed crystal is immersed into the melt. Following, the viscous melt was cooled to 990 K at a cooling rate of 0.5 K/hour followed by a more rapid cooling rate at 20K/hour. KMWPO crystallized in its high temperature tetragonal crystal as an optically perfect colorless single crystal downwards into the crucible, rather than being pulled upwards as in the Czochralski method [53]. The resulting crystal has the same orientation as the seed crystal immersed into the solution, being $2 \times 3 \times 3$ cm$^3$.

### 3.1.2 Crystal Growth KNBO

Crystal growth was performed by using the *top seeding solution growth* technique, explained in the paper by Becker *et al.* [43]. Starting at an initial temperature of 1210 K, the crystal was cooled down using a cooling rate of 0.1 K/day combined with a crystal pulling rate of 0.1 mm/day. The crystal crystallizes in its high-temperature hexagonal phase as a colorless single crystal as a hexagonal prism, with a $c$-axis along its long direction, being $6 \times 6 \times 20$ mm$^3$. During crystal growth X-ray diffraction phase analysis and electron microprobe analysis is carried out to verify the correct crystal growth and reveal any variations in stoichiometry.

## 3.2 Specimen Preparation

The main TEM specimen preparation technique applied in this thesis was the tripod polishing process. The routine is a purely mechanical preparation technique demonstrated to give large areas of superior quality compared to the conventional technique of Ar-ion milling. The advantage over conventional Ar-ion milling is that it does not introduce an amorphous surface layers and results in large millimeter sized specimens. The tripod polishing process is inspired by the work of Hunnestad [54], and based on the work by Eberg et al. [55].

### 3.2.1 Tripod Polishing

Tripod polishing is a purely mechanical specimen preparation method that has proved itself as a promising sample preparation method for perovskite materials [55]. The full tripod polishing scheme/method is provided in Appendix A. The full scheme is based on the work of Hunnestad [54], including an optimization of the technique by including and excluding certain steps.

An *Allied Multiprep System* [56] was used in the tripod polishing process to prepare the TEM specimen. The bulk specimen was mounted on a glass plate using wax before it was divided into smaller pieces perpendicular to the known facet of the bulk crystal. Initially, the bulk specimen is divided into larger slabs before being further subdivided into smaller pieces of $1-2 \times 1$ mm$^2$, using the *Testbourne Model 60 Low-Speed Diamond Wheel Saw* with a $150\mu m$ diamond metal bonded wafering blade. The $1 - 2 \times 1$ mm$^2$ slab was then attached to a pyrex, which had previously been mounted on the *Allied Multiprep System* sample holder and polished with diamond lapping films (DLFs) with coarseness 15 $\mu m$ and 6 $\mu m$. The schematic setup is illustrated in Figure 3.1, showing the subdivided crystal slab attached to the pyrex that is mounted on the polisher together with the finished sample wedge.

After calibrating the polisher, the sample holder was mounted and the crystal is polished using DLFs with coarseness 15 $\mu m$, 6 $\mu m$, 3 $\mu m$, and 1 $\mu m$ at 30 rpm using similar loads. After each grain size, successive DLFs should remove approximately three times the grain size of the previous step to ensure complete removal of deep scratches from the previous step. For the first polishing steps using 15 $\mu m$, 6 $\mu m$, and 3 $\mu m$, the load is set to 200 g, where residues are removed by a constant flow of water. For the smaller grain size with 1 $\mu m$ coarseness, the load is reduced to 50 g and *Allied GreenLube Polishing lubricant* is applied to avoid

chipping and crack formation. As the final step, a polyurethane polishing cloth with a buffered colloidal silica ($SiO_2$) solution with 0.02 $\mu m$ sized particles (*Allied Colloidal Silica Suspension*) is used. Subsequent to polishing the specimen, it is thoroughly washed with *Allied Micro Organic Soap* diluted to 2% in DI water and rinsed in DI water before inspected for chipping, scratches, or cracks.

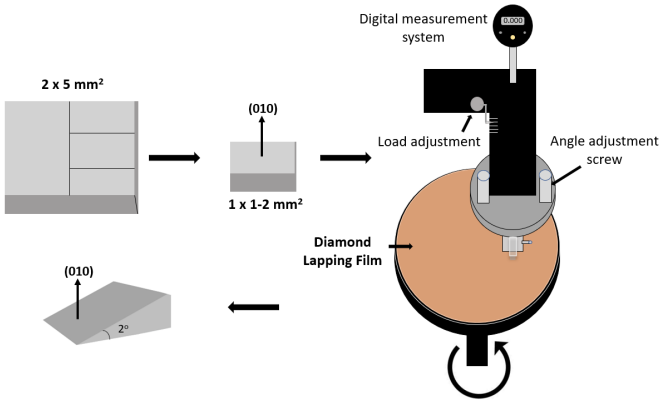


**Figure 3.1:** Schematic illustration of the specimen preparation workflow using the tripod polishing routine for a larger crystal with a known orientation having a (010) facet being produced into a wedge shaped TEM specimen.

After polishing the first side down to a smooth flat surface, it is detached using an acetone bath followed by a rinse in ethanol before being flipped and reattached with the polished side facing the cleaned pyrex for successive processing.

Using the 15 $\mu m$ DLF, the second side is polished down to approximately 500 $\mu m$ before introducing a 2° angle to the polishing system. Depending on the specimen properties, this angle can be chosen differently if larger electron transparent areas (low angle) are desired. The specimen is then polished down to 60 $\mu m$ using DLFs down to 3 $\mu m$. For subsequent steps, 1 $\mu m$ and below, the load is reduced to $< 50$ g and the sample is inspected in an Olympus X60 visual light microscope (VLM) between short intervals of 30 s, until thickness fringes are visible. The last step is using the polishing cloth with the colloidal silica solution with short time intervals for smoothing the wedge until the thickness fringes become more pronounced. The colloidal silica particles are a source of contamination that needs to be removed using the diluted *Allied Micro Organic Soap* applied to a cotton swab followed by thorough rinsing with DI water. The specimen was then attached to a Cu TEM half-grid using *Araldite* two-part epoxy glue before it was detached from the pyrex using an acetone bath. Ultimately, the specimen was cleaned in ethanol before it was ready for TEM inspection.

## 3.3 Transmission Electron Microscopy

All TEM inspections were performed at the TEM Gemini centre at NTNU, using three different microscopes. The TEM instruments used in the project is the $LaB_6$ thermionic electron source *JEOL JEM-2100*, the ZrO/W(100) Schottky field emitter electron gun *JEOL JEM-2100F*, and the cold field emitter electron gun *JEOL ARM200F*. These will be referred to as the 2100 microscope, the 2100F microscope, and the ARM microscope. The 2100 microscope, the 2100F microscope,

and the ARM microscope are equipped with a Gatan inc. *ORIUS SC 200D CCD* camera, with a Gatan inc. *UltraScan CCD* camera, and 2k Orius CCD and 2k UltraScan XP CCD, respectively. All microscopes are operated on 200 kV using a *JEOL EM-31640* double tilt specimen holder, allowing for tilt ranges of $\pm 30°$ in the x-direction and $\pm 15°$ in the y-direction.

SAED patterns were acquired working in the diffraction mode as previously described in the theory section. All diffraction patterns are captured with a camera length of 80 cm and 20-30 cm for the 2100 and 2100F, respectively unless otherwise is stated. STEM characterisation were performed on the 2100F using a *JEOL* HAADF detector and on the ARM using both a BF detector and a HAADF detector. Further imaging conditions for high resolution and regular HAADF STEM is enlisted below.

### 3.3.1 Conventional TEM

Techniques used in conventional TEM for the structural characterisation of KMWPO and KNBO involve the techniques such as BF, DF, SAED, CBED, and HRTEM. Most of the conventional TEM characterization was performed using the 40 $\mu$m condenser aperture.

### 3.3.2 Scanning TEM

BF STEM imaging were acquired using the ARM microscope, while HAADF STEM imaging were acquired using both the 2100F microscope and the ARM microscope. Below is a table listing the relevant HAADF STEM setup parameters for the 2100F microscope used together with *Digiscan* for data acquisition. The ARM microscope used similar setup parameters, but utilizes an increased electron dosage by using a larger condenser aperture.

| HAADF STEM | |
|---|---|
| Camera length | 4 - 20 cm |
| Condenser aperture | 40 $\mu m$ |
| Detector range | $\sim$ 50 - 200 mrad |
| Probe size | 0.2 nm |

All STEM data acquisition on the 2100F microscope was performed by me, while all STEM data acquisition on the ARM microscope was performed by Dr E. Christiansen or Dr U. Ludacka from the department of material science and engineering, NTNU.

## 3.4 Data Handling

All crystal visualizations presented in the project are produced with *VESTA* [37], a 3D visualization program for structural models. All TEM data analysis have been performed in *Digital Micrograph* [57] and *ImageJ* [58]. *Recipro* was also used for the analysis and indexing of diffraction patterns, using the inbuilt *Spot ID v1* and *Spot ID v2* functions [59]. PFM micrograph measurements were analysed and visualised using the *Gwyddion* software [60], version 2.62.

## 3.5 Correlated Microscopy

In order to localize the charged domain walls, the bulk crystal went through complementary techniques studies based on the work of O. Ryggetangen [50], to localize and perform site specific specimen preparation. Large regions of the bulk crystal with one side polished were mapped out using lower spatial resolution complementary imaging techniques. These techniques allow for a localization of areas containing interesting features such as CDWs, thereby greatly simplifying and increasing the chance of successfully performing site-specific specimen preparation.

### 3.5.1 Polarized Light Microscopy

Polarized light microscopy (PLM) imaging was used on the bulk crystal to map out the distribution of ferroelastic domains over larger portions of the crystal, as can be seen in figure 2.16. This allowed for the localization of the promising areas with potential charged domain walls. PLM imaging thus allowed to locate the twinning of ferroelastic domains, both before and during specimen preparation of the wedge samples until surpassing a certain thickness, being approximately 70 $\mu$m. Through locating the potential areas, the crystal could be cut into smaller-sized crystals to be prepared for wedge TEM specimen that could subsequently be polished and scanned using a PFM, which will be presented in subsection 3.5.2.

PLM imaging was performed using the *Olympus BX60* VLM with a U-AN360 quarter-wave plate. All images were acquired using a *Sony XC-77CE CCD* video camera coupled to a *Sony CMA-D2* camera adaptor. After an initial inspection, the most promising area of the crystal was selected using the *Testbourne Model 60 Low-Speed Diamond Wheel Saw*. The smaller pieces could then be polished and prepared for PFM scans to locate the site-specific areas that would be targeted using the tripod polishing routine.

A schematic setup of PLM can be seen in figure 3.2. In this routine, the specimen is illuminated from below in transmission mode, where a quarter-wave plate is inserted below the sample as a polarization filter. The light is then transmitted through the specimen before it is collected through the objective lens where it passes through an analyzer placed before the camera. Contrast then arises as a consequence from the interaction of plane-polarized light with a birefringent specimen, meaning it has a difference in its refractive index along different mutually perpendicular crystallographic directions. Upon exiting the crystal, the light components are out of phase, but are recombined and interferes as they pass through the analyzer. In this way, one can exploit the materials optical properties to reveal structural information concerning the crystal structure which is invaluable for the identification of promising domains. An image captured of the crystal with one side polished by tripod polishing can be seen in Figure 3.3, showing darker twinning domains in the shape of needles in KNBO.

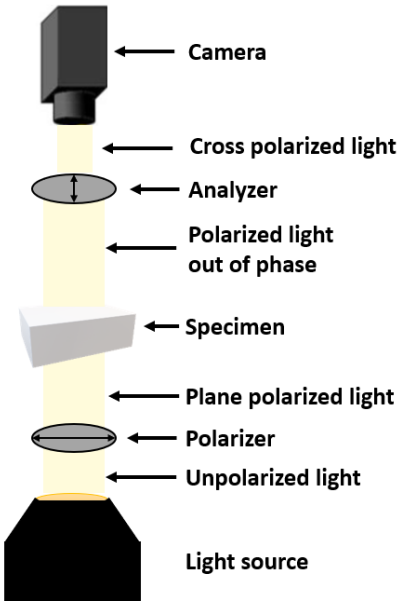


**Figure 3.2:** Simplified illustration of a general PLM setup. The light passes through two polarizing filters, rotated with 90° relative to each other because of the quarter wave plate located above the specimen.

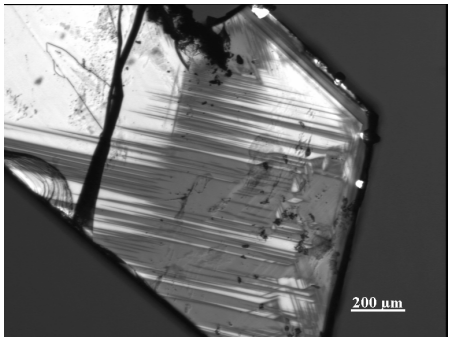


**Figure 3.3:** PLM image captured of the KNBO crystal showing dark needle-like twinning domains over large regions of the crystal.

### 3.5.2 Piezoresponse Force Microscopy

Piezoresponse force microscopy (PFM) imaging was used on the bulk polished specimen to map out the CDW distribution across the twinning regions where ferroelastic twin domains create lamellar structures. These are the CDWs observed previously in Figure 3.3, which were selected to locate the twinning regions. Contrarily to PLM, PFM can also measure the difference in potential across the domain walls, allowing for the localization of the CDWs that is of interest for this project. Performing PFM on the crystal thus show the region containing the highest density of CDWs which will be the focus of tripod polishing. The site-specific specimen preparation is performed in this order to localize the optimal stopping point for the TEM specimen preparation.

PFM imaging was performed by PhD candidate and co-supervisor Ivan Ushakov at the Department of Material Science and Engineering, NTNU. Scanning probe microscopy (SPM) data was acquired using the *NT-MDT NTEGRA* and the *Asylum Research Cypher* scanning probe microscopes, both equipped with a *ASYELEC.01-R2* tip. In the PFM configuration, the NTEGRA microscope was used where the PFM tip was grounded where an alternating voltage of 10 V and 40.13 kHz frequency was applied to the specimen stage. PFM measurements of the specimen were acquired using a scan rate of 0.22 Hz spanning over areas up to 85 x 85 $\mu m^2$. PFM measurements were processed using the SPM data analysis software *Gwyddion* [60]. In addition, kelvin probe force microscopy (KPFM) and electrostatic force microscopy (EFM) was attempted to verify the nature of the CDWs, to ensure the configuration of the domain walls. These measurements were captured using the Asylum microscope in both configurations. In the EFM configuration a voltage of 15 V applied to the tip, at the same resonance frequency. In the KPFM configuration an alternating voltage of 3 V was applied to the tip, at the same resonance frequency.

CHAPTER

# FOUR

# RESULTS

The following chapter will present the results from the specimen preparation and TEM characterization for KMWPO in section 4.1 and KNBO in section 4.2. First, the specimen preparation for each material is presented in each section: an [110] oriented large specimen of KMWPO and a [001] oriented large specimen of KNBO. Second, a structural characterization of the prepared tripod wedges are presented with the main focus on domain structure imaging of KMWPO and lattice imaging of a specific H-H domain wall of KNBO.

## 4.1 KMWPO

This section presents the findings related to the preparation and characterization of the [110] out-of-plane oriented specimen, including a description of the specimen preparation, structural analysis, and inspection of structural features. One of the main objectives of this study is to provide a first basic TEM characterization of KMWPO. In order to study and investigate the material known to have different planar boundaries (e.g. twin boundaries and different types of domain walls), correlated microscopy techniques were employed to increase the likelihood for the specimen to contain areas with interesting features after specimen preparation. In the TEM analysis, the central parts are i) to confirm the crystallographic orientation of the specimen via a tilt-series analysis and ii) an analysis of the structural features observed along the electron transparent specimen edge.

### 4.1.1 Specimen Preparation

A specimen of [110] oriented KMWPO was prepared using the mechanical tripod polishing routine described in Appendix A. The crystal underwent a series of steps in the routine, gradually introducing finer roughness DLFs. KMWPO experiences fast material removal in all directions, imposing the risk of removing excessive amounts of material with the tripod polishing technique. After polishing the first side with the final step using colloidal silica particles, polarized light microscopy was employed. PLM did not reveal apparent twinning domains, but did show a slight change in contrast of certain areas along the edge upon adjusting the analyzer, marked with arrows in Figure 4.1. A small region along the edge of the

attached sample can be seen to appear darker in Figure 4.1 (a) while in (b) it appear more alike to the surrounding areas of the crystal.

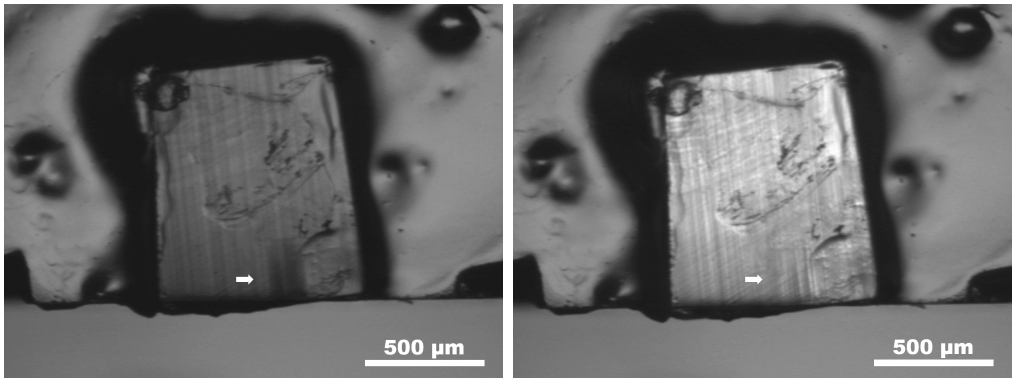


**(a)** **(b)**

**Figure 4.1:** PLM overview images (a) and (b) in transmitted light mode captured of the KMWPO crystal attached to the polishing stub prior to the second side polishing at two different analyzer settings. The arrow points at the region of changing contrast.

The area of interest marked in Figure 4.1 was marked as the area of interest prior to planar polishing of the second side. The polishing routine was subsequently continued, with regular inspection in optical microscope, until the thickness of the crystal was reduced sufficiently to give an inward shift of the specimen edge upon further material removal as well as the appearance of thickness fringes along the edge of the crystal. The resulting crystal after the second side polishing using colloidal silica particles can be seen being attached to a TEM half-grid in Figure 4.2 (a). The specimen exhibited some degree of chipping along the $> 1$ mm edge. At higher magnification thickness fringes became visible in Figure 4.2 (b), observed along the parts of the edge not affected by chipping. In general, the cracks and chipping only affected a relatively small area along the large specimen edge showing uniform thickness fringes. All of these observations serve as indications that a high quality TEM specimen is obtained from the tripod polishing specimen preparation routine.

Crystal inspection using PLM with the [110] in-plane orientation revealed interesting characteristics appearing at different analyzer settings. A PLM of a polished cross-section of the specimen is shown in Figure 4.3. Compared to the [110] out-of-plane, the [110] in-plane show differently colored domains and are visible across the entire specimen. The domains are very sensitive to the analyzer setting which is seen from adjusting the analyzer settings. Darker contrast domains is seen along four different directions within the crystal. The dark domains in Figure 4.3 (c) can be seen to extend perpendicular to each other, while within each of the domains enclosed by these features, there are domains forming at an angle of $\sim 45^\circ$ in relation to them. These alternate within each region enclosed by the darker domains and show inverse directions upon transitioning to the adjacent domain. There are many intriguing details that can be observed with the given orientation of the crystal. However, due to unfortunate geometry of the crystal, tripod polish consuming material, and small dimensions of the crystal, no success-

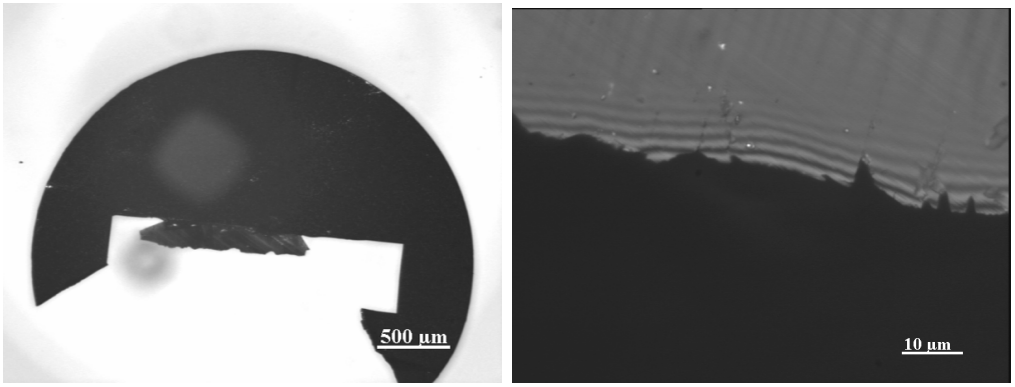


**(a)** **(b)**

**Figure 4.2:** Optical images (a) of KMWPO tripod specimen attached to the TEM half-grid and (b) thickness fringes along the edge of the KMWPO tripod edge.

ful tripod specimens were produced. Several attempts were made, but no final TEM specimen was achieved with the main problem being to attach the polished wedge specimen to the half-grid without getting glue on the electron transparent areas.

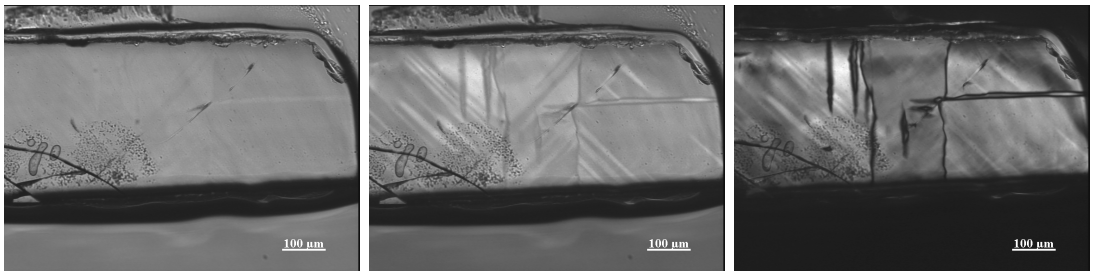


**(a)** **(b)** **(c)**

**Figure 4.3:** PLM (a-c) overview of [110] in-plane oriented KMWPO showing different analyzer settings.

PFM measurements show dominating stripe domains with additional zig-zag patterns of alternating contrast on the polished surface of the bulk KMWPO crystal, seen in Figure 4.4. Alternating contrast domains are seen to be equidistant along the surface, with a width of approximately 2.1 $\mu$m. The out-of-plane configuration, meaning the cantilever is deflected out-of-plane, reveals the best contrast difference for the domain structure, with the most distinct contrast difference seen for the zig-zag pattern in Figure 4.4 (a). The oscillating zig-zag pattern appears to increase in width and length further upwards in the material. Alternating stripes appear rather uniform without any apparent changes. The features extend at an angle in relation to each other, and appear to have opposite contrasts as they intersect.

These patterns, such as the ones in Figure 4.4, were observed to dominate over large parts of the crystal with the given orientation.

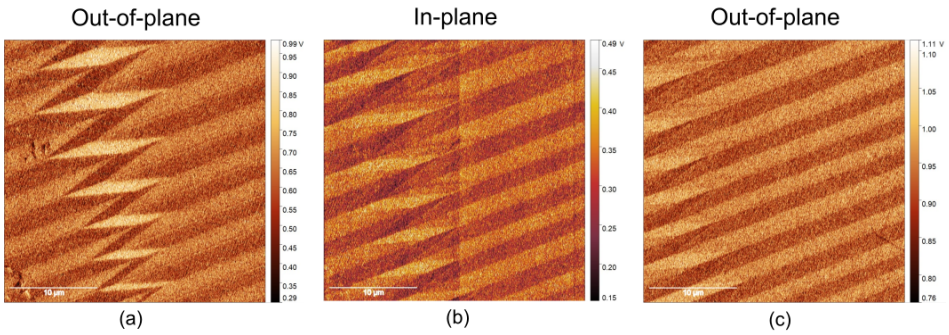


**Figure 4.4:** PFM scans (a-c) with two different configurations of a bulk KMWPO crystal showing a dominating stripe domain of alternating contrast and a zig-zag pattern. The different configurations measure the cantilever deflection in-plane and out-of-plane. In courtesy of Ivan Ushakov and Dennis Meier.

### 4.1.2 TEM and STEM Characterization

During the TEM inspection of the KMWPO specimen, the majority of the edge was observed to exhibit homogeneous electron transparency, except for regions covered by $SiO_2$ particles and cracked areas from specimen preparation and specimen handling. To study the single crystal in this orientation the specimen preparation was highly successful, showing high quality regions with low degree of induced damage from mechanical specimen preparation. However, contaminants in the form of specimen chipping and cracking were detected near parts of the specimen edge, resting on the bulk crystal, as shown in Figure 4.5. Cracking in the crystal seem random and not straight, indicating that there is no apparent cleaving planes perpendicular to the [110] direction. Along parts of the specimen edge, induced specimen bending was observed as variations in crystallographic orientation and bending contrast. These effects only affected the thinnest part of the specimen and remained uniform at thicker regions.

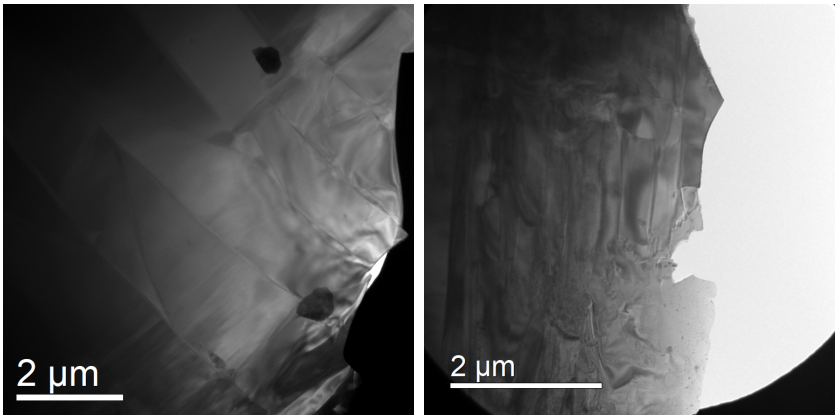


**Figure 4.5:** Representative BF overview images of (a) thick area with dark particles resting on the specimen and (b) thin edge with uniform intensity and no features.

To confirm the crystallographic orientation of the KMWPO crystal, which was intentionally prepared with a [110] facet, a tilt series was captured from the same position in the crystal. This tilt series successfully mapped out all reachable lower order zone axes along the kikuchi bands parallel to the tilt directions illustrated in Figure 4.6 (a).

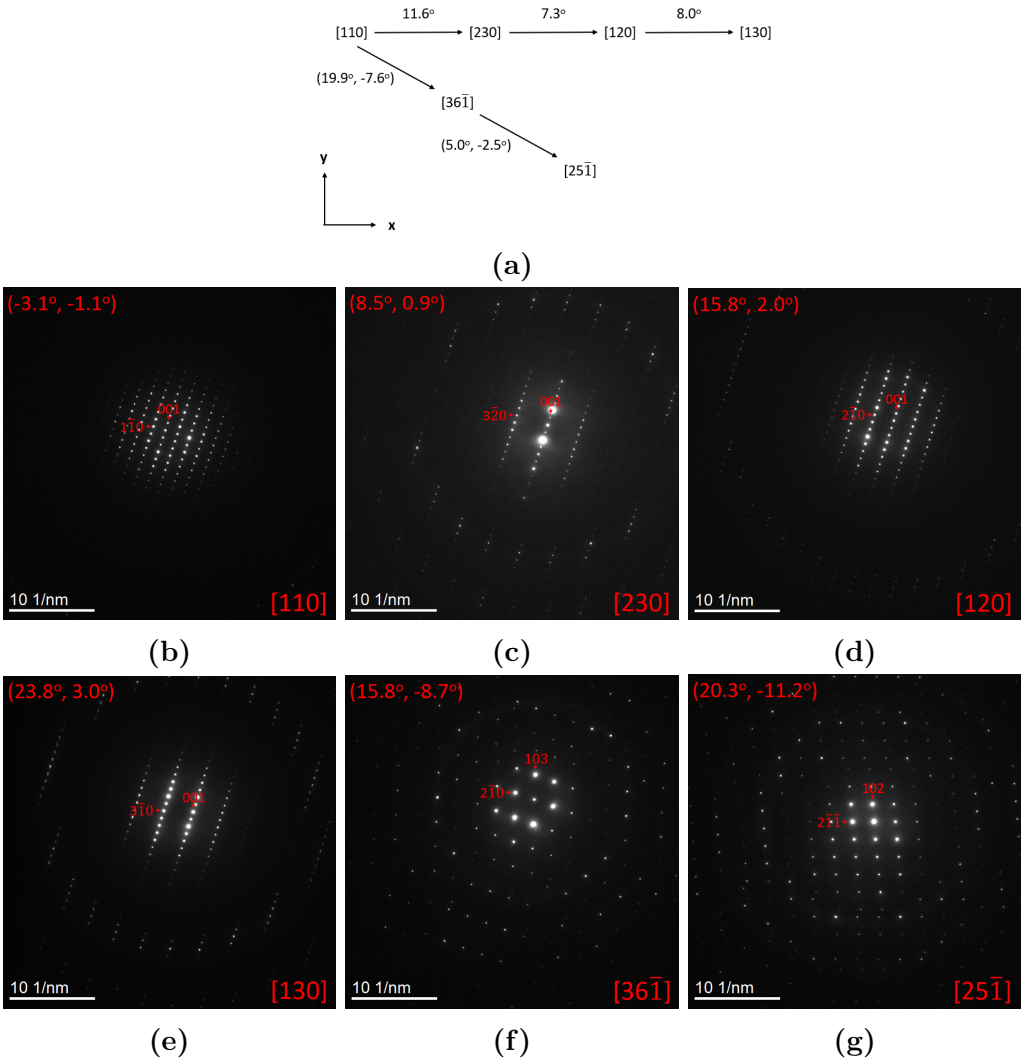


**Figure 4.6:** (a) Schematic of the tilt values given for the experimental tilt series together with the relative tilts between the zones and (b-g) experimental SAED images captured from the tilt series.

Tilting the [110]-oriented KMWPO specimen along the kikuchi bands within the limited tilting ranges, ±30° for x-tilt and ±15° for y-tilt, resulted in the identification of various zone axes, shown in Figure 4.6. A series of SAED patterns were obtained, each annotated with the corresponding relative rotations and zone axes designated, shown in Figure 4.6 (b-g). A total of six different zone axes were located within the gonio tilt ranges. The starting point was identified to be the [110] zone axis appearing at (-3.1°, -1.1°), indicating that after specimen preparation, one is near the intended direction.

The expected triclinic phase and the crystallographic orientation of the KMWPO

crystal was confirmed to have a [110] facet by successfully reproducing the corresponding tilt series simulation in ReciPro, as depicted in Figure 4.7. The identification was based on comparing the ratio of distances between diffraction spots in the experimental SAED patterns with those from the simulated tilt series. The relative tilts between zone axes were noted and compared with simulations.

A comparison of the experimental and the simulated diffraction patterns revealed additional spots in the simulated patterns that were not clearly visible in the experimental patterns for zone axes [36$\bar{1}$] and [25$\bar{1}$]. These additional spots appeared as triplets, with the central spot being the most intense. Although these weaker spots in Figure 4.6 (f) and (g) were mostly overshadowed by the stronger more intense spots and only appeared in close proximity to certain spots near the central spot, their position correspond with the simulated zone axes. Based on this, the crystallographic orientation is confirmed for the [110] facet KMWPO crystal. In addition, the first order laue zone can be observed in certain zone axes, providing additional information on the patterns.

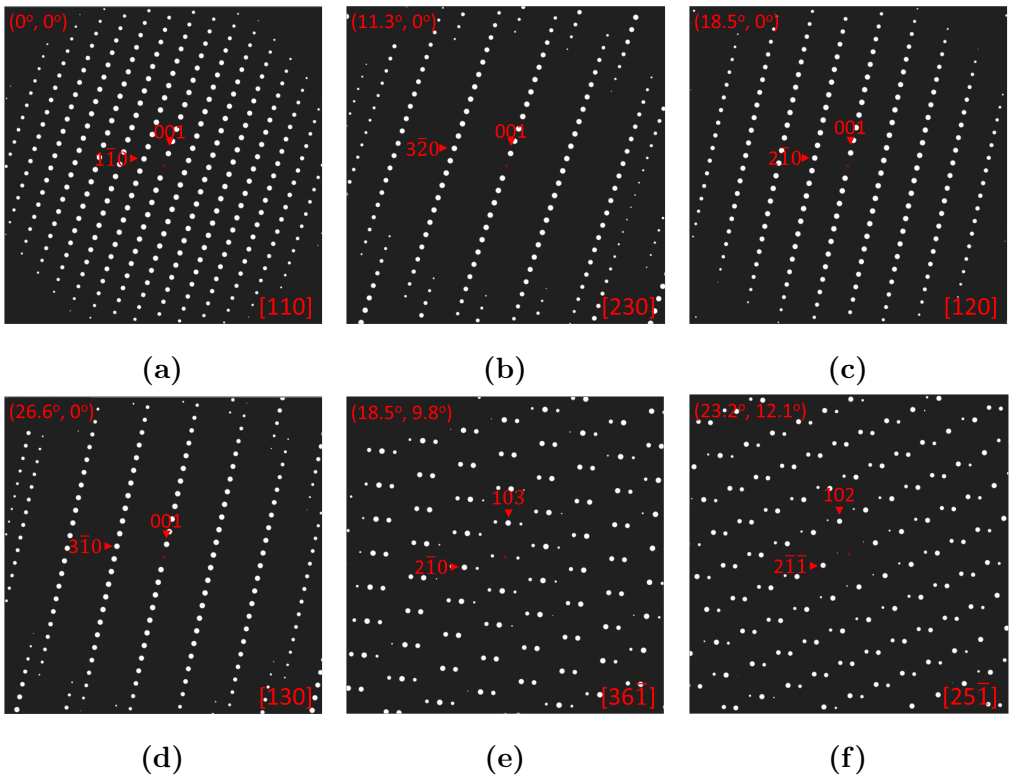


**Figure 4.7:** Simulated kinematic SAED patterns of zones found in experimental tilt series, using the Recipro software, (a-f) corresponding to diffraction patterns (b-g) in Figure 4.6.

Performing a general inspection of the appearance of KMWPO specimen, several recurring structural features were identified across the specimen using the BF technique. These features consisted of alternating contrast horizontal or vertical lines and horizontal needle-like structures. Examples of these structural features are seen in Figure 4.8 together with a schematic annotated with a labeling convention for further analysis. Horizontal and vertical lines exhibit alternating contrast between adjacent features, while adjacent needles have been observed to

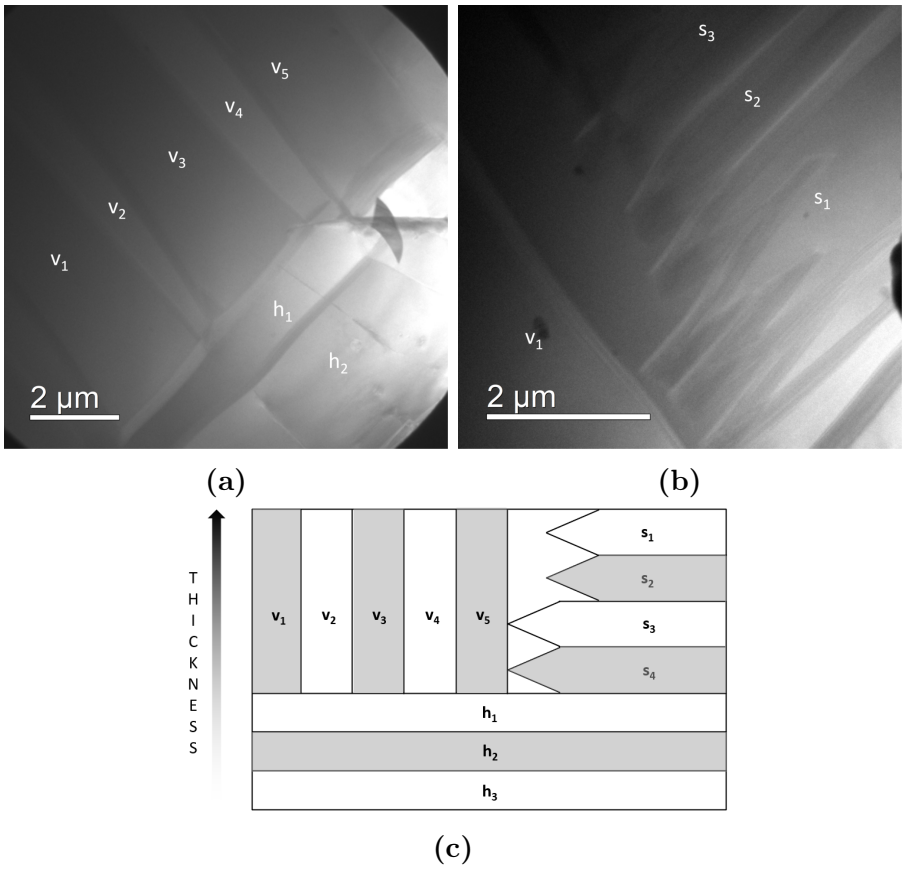


**Figure 4.8:** BF overview images (a) and (b) of structural features with differences in contrast observed in [110] oriented KMWPO specimen, and (c) a schematic representation that contains the same features observed with different contrast combined in one image annotated with notations. The distinct features are labeled in order to relate further analysis to the features.

exhibit both identical and alternating contrast. Features are termed horizontal and vertical based on their shape relative to the specimen edge. These features are perpendicular to one another and terminates at the interface of perpendicular features with similar aspect ratios. Needles on the other hand either ends abruptly or gradually in a pencil shape point; some needle-shaped features extend fully to the interface of vertical features while others cease at a distance from the interface. Vertical lines on the other hand abruptly end at the horizontal lines, which are the most prominent features observed, appearing over large areas of the specimen. Furthermore, the interfaces separating features vary in sharpness, being observed as both sharp and broadened interfaces. Horizontal and vertical lines tend to have straight interfaces. However, observations have been made on interfaces exhibiting curvature or convergence.

Structural features vary in sizes, having widths ranging from less than a micron and up to a couple of microns and lengths spanning from a few to tens of micrometers across the specimen. The widths are comparable to what was measured using PFM in Figure 4.4, being 2.1 $\mu$m. Vertical features follow the $g_{1\bar{1}0}$ direction, while horizontal features and needle-like features align with the $g_{001}$. Although the features tend to follow these directions, variations occur as interfaces exhibit sudden

directional changes, curvatures or convergences. This behavior can be observed in Figure 4.8 (b) where the vertical features of higher intensity gradually converges towards the horizontal bright feature. The horizontal feature is observed to have a varying curved width, with broadened interfaces on both sides.

The occurrence of these features depends highly on the specimen thickness. In regions close to the edge, horizontal features are most prominent, while vertical and needle-like features occur more frequently further from the specimen edge at thicker regions. However, exceptions have been observed in cases which vertical features are found to extend fully to the edge of the sample, such as in Figure 4.5 (a). Because of the higher presence of horizontal features along thin specimen regions, these features were selected for further investigation.

To gain a better understanding of the nature of the observed structural features, SAED patterns were captured of horizontal features to investigate their crystal structure. The difference in diffraction conditions of adjacent features causes them to exhibit alternating contrast. A difference in crystallographic orientation should be visible in SAED patterns. For this reason, SAED patterns were obtained for the horizontal features labeled $h_1$, $h_2$, $h_3$, and $h_4$, illustrated in Figure 4.9. To investigate the interface, SAED patterns were captured within $h_1$, $h_2$, at the interface between $h_2$ and $h_3$ (marked $h_{2/3}$, and within $h_3$. These patterns were captured of the region containing multiple horizontal features of alternating contrast, shown in Figure 4.9 (a). SAED patterns were taken within the features as well as across the interfaces.

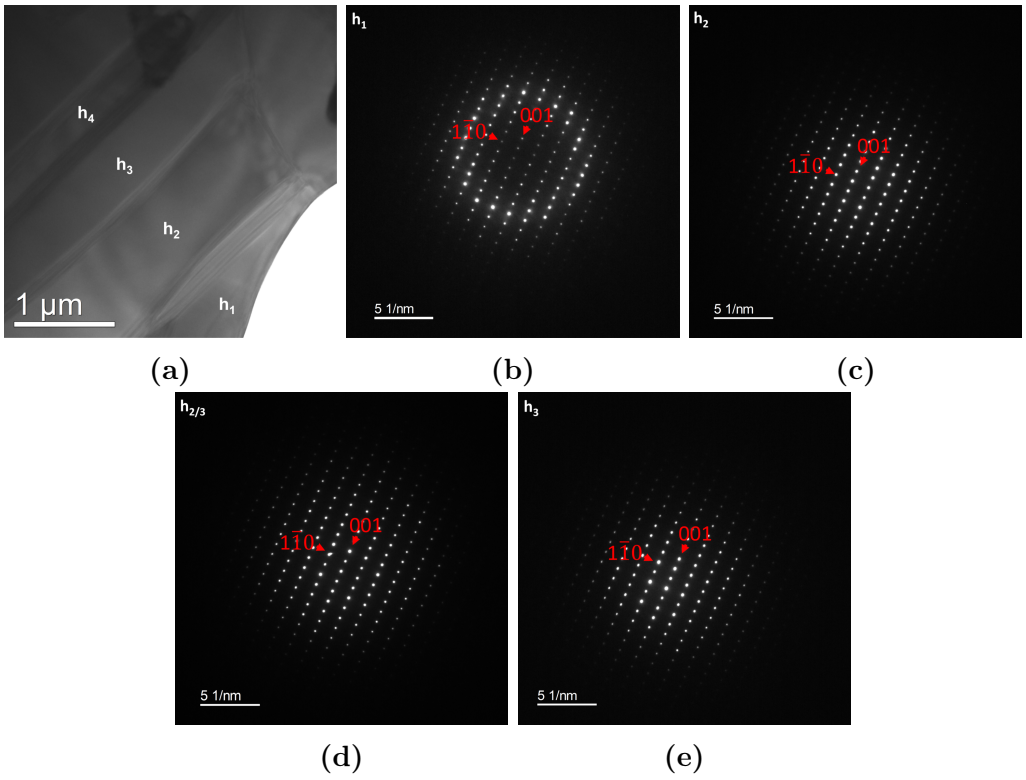


**Figure 4.9:** BF image (a) showing an overview of horizontal features $h_1$-$h_4$ displaying differences in contrast along the edge of the KMWPO specimen and (b-e) SAED patterns captured within the labeled features, respectively.

All SAED patterns in Figure 4.9 (b-e) correspond to the [110] zone axis, with minimal differences between the patterns. The only exception is Figure 4.9 (b), which was captured closer to the edge and exhibited a slight mistilt away from the [110] zone axis in terms of its crystallographic orientation. Similar analyses were conducted for vertical features and needle-like features and are provided in Appendix B, yielding similar results to those observed for horizontal features. The structural features shows similar crystal orientations. Hence, the differences in contrast of the boundaries between features must stem from other factors.

To inspect for intensity variations within the diffraction spots, a DF-TEM series was acquired. Ferroelectric polarization can influence the intensity of diffraction spots, those with a component of the polar axis, by affecting the diffraction conditions, leading to different interference effects. This can for some cases be differentiated using DF TEM based on the relative intensities of diffraction spots. The DF-series from similar horizontal features is presented in Figure 4.10, along with the corresponding diffraction spot selected by the objective aperture. Examining Figure 4.10 (b) and (c) formed by diffraction spots $(1\bar{1}0)$ and $(\bar{1}10)$, a switching of contrast in the dark field images appears, marked by arrows. Adjacent regions exhibit different levels of brightness depending on the selected diffraction spot. Conversely, no similar contrast switching was observed upon selecting the diffraction spots (001) and $(00\bar{1})$.

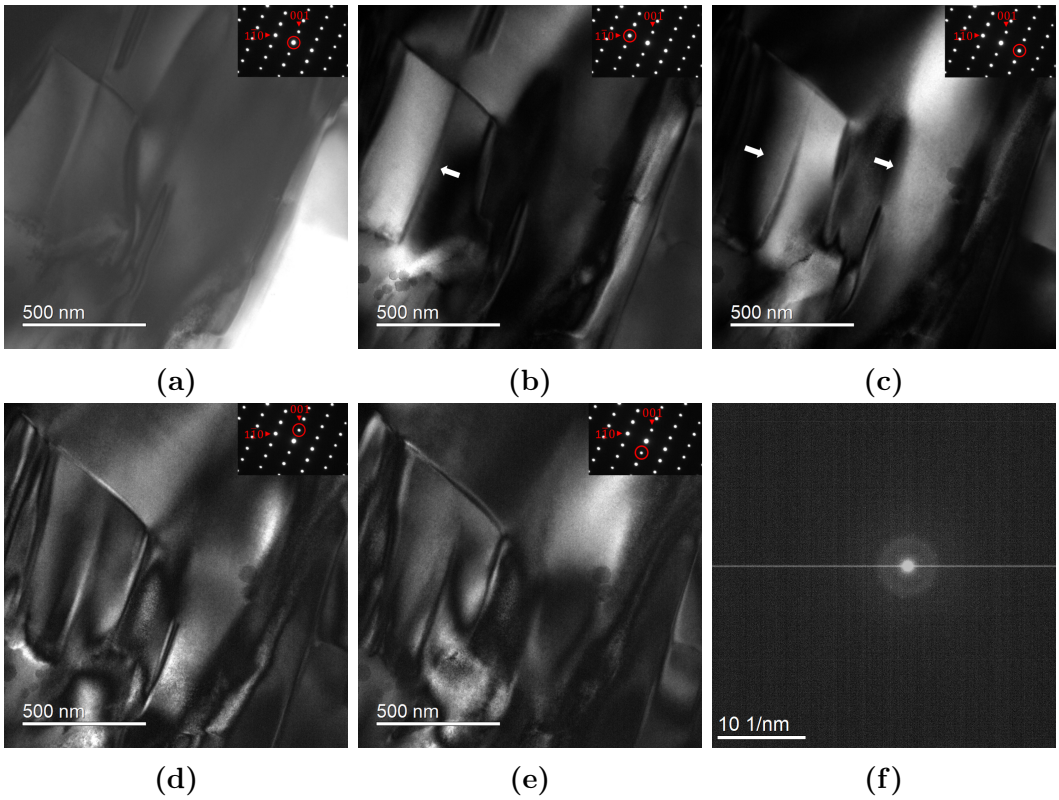


**Figure 4.10:** (a) BF image and (b-e) centered-DF images showing a full DF series of features displaying different contrast along the edge of the KMWPO specimen and (f) showing the diffraction pattern from the same area after capturing the DF series.

Further analysis of this region for example by high magnification DF TEM was no longer possible as SAED after initial DF-series shows that the material turned amorphous. A prolonged exposure thus induced structural damage to the material, creating large amorphous regions. After the DF series was acquired, no BF or DF contrast can be seen to remain from the horizontal features. Therefore, an area in the surrounding region was imaged to enhance the contrast differences in Figure 4.10 using off-axis DF. This was performed by maintaining diffraction spots $g_{1\bar{1}0}$ and $g_{\bar{1}10}$ constant by tilted along the crystallographic $c$-direction. The crystal was tilted to (-2.7°, 5.1°) in the x- and y-direction, respectively, being positioned between off-zone. In this way, the $g_{1\bar{1}0}$ and $g_{\bar{1}10}$ diffraction spots are enhanced by suppressing other diffraction directions as indicated by the DP in Figure 4.11. The off-zone DF series of a small needle-domain is displayed in Figure 4.11, together with the respective diffraction spots from which the image is formed. No apparent differences are seen from the two diffraction spots other than that selecting $g_{1\bar{1}0}$ results in an enhanced scattering in the region towards the right, while $g_{\bar{1}10}$ shows no significant scattering apart from enhanced areas within the needle-like feature. It should be noted that the signal weakened towards the end of the off-axis DF series, as can be seen from image (c), leading to a lower signal-to-noise ratio.

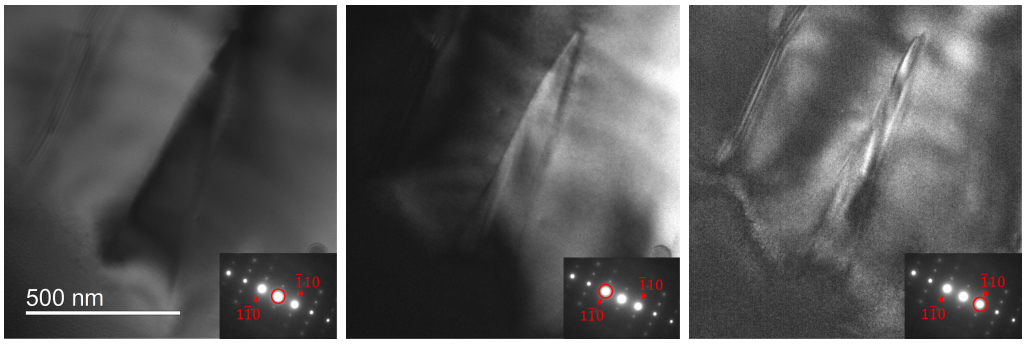


**(a)** **(b)** **(c)**

**Figure 4.11:** Off-zone BF image (a) and DF images (b) and (c) together with the respective diffraction spot used in the image formation. The area contains a small needle-like structure which showing a loss of signal in (c).

Upon inducing structural amorphization of an area containing structural features, the surrounding areas undergo changes in contrast. Figure 4.12 illustrates a region with both horizontal and vertical features before and after exposures in the DF series. Following the local amorphization effects, the area at higher thickness exhibit localized darker contrast, marked with arrows in Figure 4.12 (b). The area surrounding the damaged area experience a change in contrast, appearing darker compared to the same area prior to exposure. After inducing beam damage to the specimen, no structural features are observed.

Lattice imaging of a horizontal feature was attempted with HRTEM, including inspections within the feature and its interface, despite the risk of beam damage from high dose techniques. Investigation of the interface separating features at higher magnification revealed the possibility of capturing images using a slightly converged beam without damaging the material, illustrated in Figure 4.13. Figure 4.13 (a) showcases the interface between two horizontal features being de-

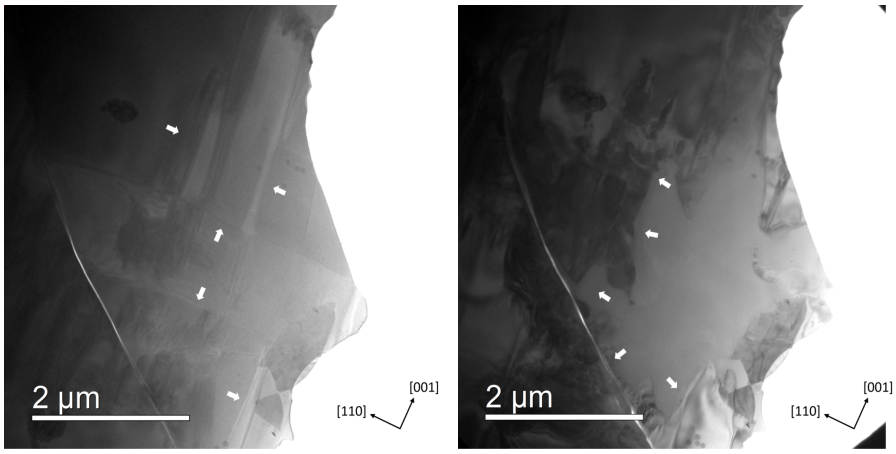


**(a)** **(b)**

**Figure 4.12:** (a) and (b) shows BF images before and after an extended exposure to the electron beam upon capturing a dark field series, showing how differences in contrast from features are removed and shifted away from the regions affected by beam damage.

tectable by its darker contrast, stretching along the [001] direction. A rough estimate suggests that the interface is an extended region with a width of 11-12 nm. A general area within a horizontal feature is illustrated in Figure 4.13 (b) and (c) together with their respective FFTs. These images were captured of the same region before and after converging the beam over a short time interval, resulting in localized beam damage.

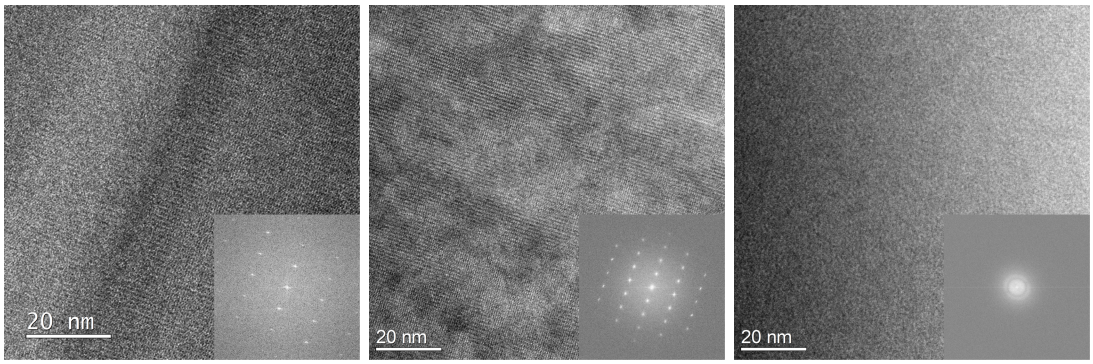


**(a)** **(b)** **(c)**

**Figure 4.13:** HRTEM images together with their respective fast fourier transform (FFT) showing (a) captured at the interface between two horizontal features of different contrast, while (b) and (c) are captured before and after exposing the feature with a convergent beam causing amorphization of the material.

Several intriguing features were observed in the conventional TEM investigations, indicating the need for further analysis. HAADF STEM, being a highly informative technique was employed for further analysis of the structural features. Low-mag HAADF STEM revealed distinct regions of different contrast, extending along the $[1\bar{1}0]$ direction from the specimen edge, illustrated in Figure 4.14. This

shows how the interface of two darker features extends from the edge, experiencing sudden directional changes accompanied by additional contrast changes within the features, marked with an arrow. Notably, these two darker features, labeled (h1 and h3), appear to be merging in the bottom left corner as they draw closer together. Furthermore, brighter contrast features can be observed along the $g_{001}$ direction, while a sharper line parallel to the darker domains appearing in the top right corner. Both the brighter and darker features bear a striking resemblance to the previously observed horizontal and vertical features in TEM mode, having once a gain directions perpendicular to one another.

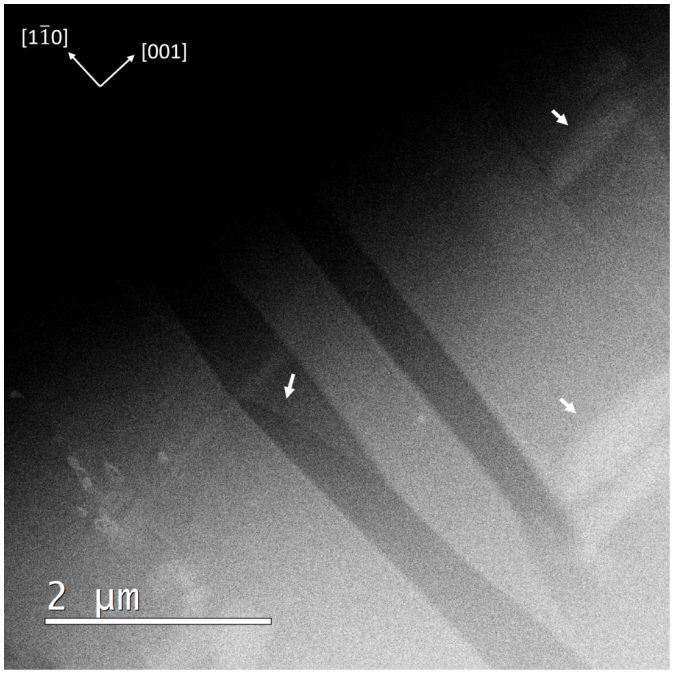


**Figure 4.14:** HAADF-STEM image showing contrast differences from regions propagating inwards into the material towards increasing thickness along the [$\bar{1}$10] direction from the edge. Brighter contrast regions can also be seen perpendicular to the darker contrast features along the [001] direction on both sides of the darker features perpendicular to the edge.

Further investigation of these features at higher magnification shows the emergence of lattice resolution imaging using HR HAADF STEM, shown in Figure 4.15. The material was successfully imaged along the projection of the [110] zone axis, accompanied by its respective FFT in Figure 4.15 (a). Image (b) displays an inverse FFT with the filtered signal to improve the noise-to-signal ratio and contrast together with the filtered signal used in the inversion. Within the Figure 4.15 (b), a distinctive wave-like pattern appear, extending along the *c*-direction. The wave-like pattern closely resembles the simulated crystal structure of the [110] oriented KMWPO, illustrated in Figure 2.14. The wave pattern highlights how the structural unit [$WO_6$] in an alternating chain with [$MgO_6$] along the crystallographic *c*-direction. Imaging structural features at atomic scale presented significant challenges. As seen with DF TEM and HRTEM, beam damage is representing a practical limitation when imaging the material with high dosage techniques. Lattice imaging experienced similar behavior, offering several challenging aspect as it

requires to not succeed the electron dosage threshold and avoid repetitive scans. This highly limits the time interval for optimization of imaging parameters such as defocus, astigmatism, dwell time and scanned areas with the smallest 0.2 nm electron probe.

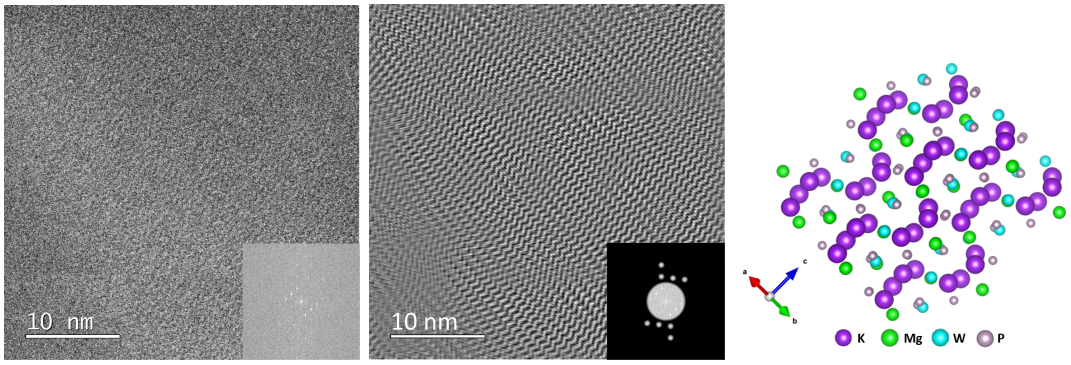


**(a)** **(b)** **(c)**

**Figure 4.15:** HAADF STEM image (a) with 512x512 scanning points using a dwell time of 3.0 $\mu$s together with its FFT and (b) inverse FFT of the filtered filtered signal showing a wavelike chain of atoms in the material resembling (c) the crystal structure of KMWPO for zone axis [110]

While HAADF-STEM offers lattice resolution imaging, it is essential to exercise with caution prior to the image acquisition. Prolonged exposure of the electron beam in the STEM mode cause beam damage, having a detrimental effect on KMWPO causing structural changes and specimen degradation. Optimizing the imaging parameters and reducing the dwell time, lattice resolution imaging has been successfully achieved using the HAADF-STEM technique. However, observations show that repetitive exposures with the intense electron beam causes sample degradation and amorphization. Structural changes occur even for small dwell times of less than a $\mu$s with repetitive exposures causing an accumulation of beam damage. To mitigate the adverse effects of beam damage, it is necessary to consider both dwell time and avoiding repetitive exposures. Figure 4.15 demonstrates the impact of dwell times and scan points by comparing the effect of a 3 $\mu$s dwell time has on the material, while Figure 4.16 (a) and (b) showcase the consequences of longer dwell times of 6 and 8 $\mu$s and smaller pixel sizes, respectively. Figure 4.16 (a) generates a weak signal from crystalline material in the start of the scan, being scanned top-down, while (b) surpasses the threshold limit to cause a detrimental effect causing harm to the material.

Beam damage was observed for dwell times as low as 0.5 $\mu$s using the 40 $\mu$m condenser aperture resulted in beam damage even at 800 k magnification with 512x512 scan points when exposed repetitively, leading to a loss of signal and degradation of sample quality. However, a dwell time of 3 $\mu$s at higher magnification proved to be possible at 512x512 scan positions in Figure 4.15 as long as the material was not repeatedly exposed to the electron beam separated by short time intervals. Therefore, utilizing a reduced dose per area while avoiding repetitive exposures is the best suited technique that ensures to maintain the structural integrity of the material.

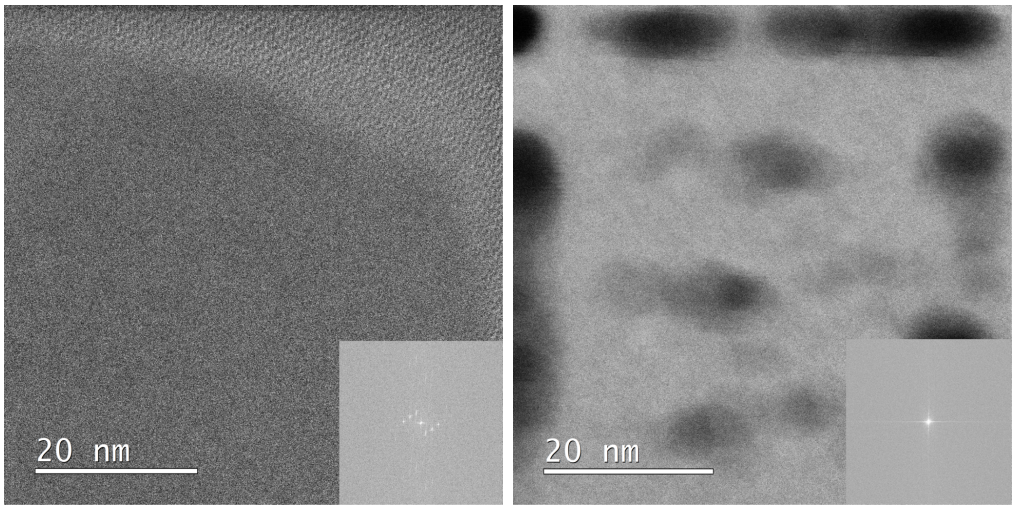


**(a)** **(b)**

**Figure 4.16:** HAADF STEM images captured at different dwell times (a) with a 6 $\mu$s dwell time in a 1024x1024 pixel image with its FFT and (b) with a 8 $\mu$s dwell time in a 2048x2048 pixel image, both causing amorphization and degradation of the material.

## 4.2 KNBO

This section presents the findings related to the preparation and characterization of the *c*-axis out-of-plane oriented specimen, including a description of the site-specific specimen preparation, the structural analysis, and the domain configuration investigation. One of the main objectives of this study is to elucidate the structural configuration of the charged H-H domain boundaries observed in [001] oriented KNBO. To achieve this goal, it is essential to have the rare H-H domain boundaries within the electron transparent edge of the [001] oriented KNBO. Therefore, correlated microscopy was employed to have an accurate stopping point during the site-specific specimen preparation. Furthermore, to confirm the crystallographic orientation of the specimen, a tilt-series analysis is presented.

### 4.2.1 Specimen Preparation

In total, two attempts were made for the site-specific specimen preparation using correlated SPM-PLM-TEM for the atomic scale study of charged twinning domain boundaries in KNBO. The first attempt gave excellent SPM results. However, under tripod thinning a crack developed, causing the area of interest to be lost. The SPM results, i.e. distribution and morphology of the different domains, and careful consideration of the final thinning steps were used to have a successful second run. The second [001] oriented KNBO sample was meticulously prepared using a modified version of the tripod polishing method described in Appendix A. This approach was performed with utmost care, requiring multiple repetitions of sub-micron DLFs to ensure site-specific specimen preparation. These steps included frequent repositioning and limited time steps to ensure that no imperfections formed during the polishing steps. Prior to initiating the final polishing

step, potential areas of the KNBO crystal was identified using PLM, that contained lamellar twinning of twinning domains, being the most likely positions for charged domains, as depicted in Figure 4.17. The region revealed extensive regions containing twinning domains within the crystal, with lamellar twinning between two directions, representing the area of interest. From PLM, mainly two regions were inspected with higher magnification, highlighted in Figure 4.17 (b). The wedge was positioned on the pyrex such that both regions are intersected by the final tripod wedge.

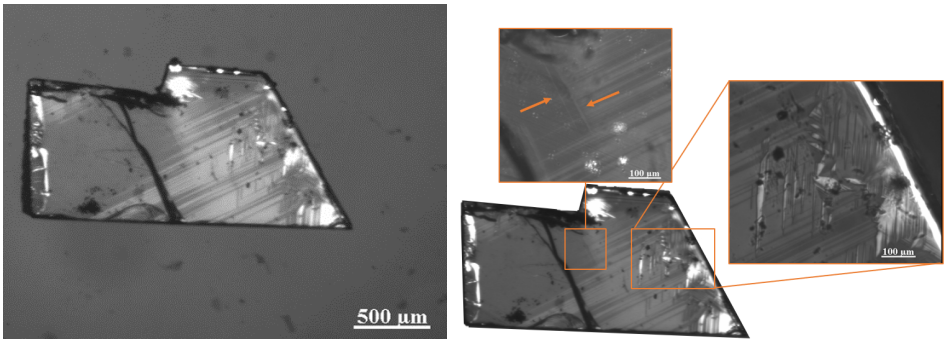


**(a)** **(b)**

**Figure 4.17:** PLM overview images (a) of the KNBO crystal prior to the second side polishing containing needle-like twinning domains over large parts of the crystal and (b) with the interesting areas with lamellar twinning are highlighted in the crystal.

The PFM investigation revealed that one of the prospective areas highlighted by PLM may represent a charged H-H domain wall. The PFM scans, presented in Figure 4.18, depict a larger needle-shaped domain forming angles (30° and 90°) different from the prominent twinning axes, forming at 120° relative to one another. The dominant twinning axes forming at this angle has the tendency to stretch from one corner to the second closest corner, while charged domains tend to form diagonally across opposite corners in hexagonal-shaped single crystals grown using similar crystal synthesis methods, e.g. from approximately 5 to 11 o'clock. The PFM scan in Figure 4.18 (a) highlights an area from which an EFM scan is performed. The EFM scanning mode registers charged areas and shows how only the H-H domain walls are visible in the scan configuration, while T-T twinning domains are not. In (b) a scan of the charged needle in the specimen prepared successfully is depicted, forming at 90° degrees relative to the uncharged twinning domains. These scans were performed at opposite sides of the macroscopic crystal, but have corresponding directions of the charged twinning domain walls. Therefore, the left side of the needle running from 2 to 8 o'clock, marked with an arrow in Figure 4.18 (b) corresponds to the H-H configuration, while the right side of the same needle is the T-T configuration. All other needles extending perpendicular to this domain are head-to-tail (H-T) or tail-to-head (T-H) configurations, all being neutral. Similarly to T-T domain walls, these are not visible in EFM scans.

The area measured with PFM is depicted in Figure 4.17 and is marked with an arrow as it was selected as the area of interest. The largest needle was visible in PLM and was used during specimen preparation. This needle maintained the

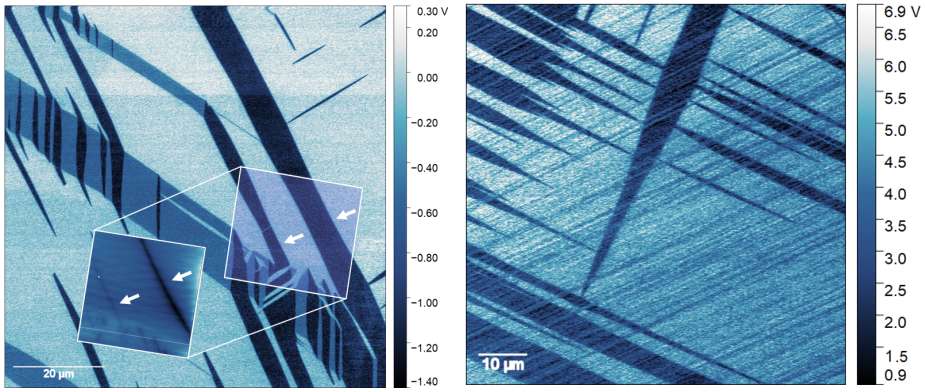


**(a)** **(b)**

**Figure 4.18:** PFM scans (a) of the crystal used for the first attempt of site-specific specimen preparation with a highlighted region from an EFM scan and (b) of the KNBO specimen characterized in this thesis. The EFM scan measures the electrostatic forces across the charged H-H domain wall. In courtesy of Ivan Ushakov and Dennis Meier.

directional tendency of charged domains stretching diagonally across the hexagonal crystal. For these exact reasons, the needle was chosen as the endpoint of the site-specific specimen preparation as it represented the most evident charged domain stretching over more than a 100 microns through the crystal. Prior to performing the specimen preparation, measurements were taken of the position of the needle chosen as area of interest. These measurements estimated that the charged needle domain spans over the interval [580 $\mu$m, 750 $\mu$m], denoting the distance from the bottom edge of the crystal in Figure 4.17 (a).

The resulting tripod wedge after the final polishing step is depicted in Figure 4.19, placed on the pyrex polishing support with an orientation of the crystal recognized by its oblique side. The stopping point was reached using a gradual polishing process with several repetitions of DLFs with 0.1 $\mu$m roughness before several steps with the polishing cloth with colloidal silica particles to remove the remaining material. Upon completion of the site-specific sample preparation, measurements were captured at various positions along the crystal edge to determine the distance from the thin side of the wedge to the thick side of the wedge, denoted d. Measurements along various positions thus resulted in the distance d being within the interval [645 $\mu$m, 660 $\mu$m], being well within the estimated span of the charged needle domain estimated prior to specimen preparation. The edge of the specimen is indicated by the gold coloured line in Figure 4.19 (b), intersecting both regions highlighted in Figure 2.16 (b)

For future analysis, the crystal was subdivided into three main areas, denoted area A, B, and C, shown in Figure 4.20 (a). Areas A and B corresponds to the wedge-polished intersection points of the highlighted areas in Figure 4.17, while area C is an reference area for bulk/defect free region on the opposite side of the crystal where no twinning domains were observed. Investigation of the crystal attached to the TEM half-grid with PLM, depicted in Figure 4.20 (b), revealed weak indications of recognizable features being brighter parallel lines nearly perpendicular to the specimen edge. These features resemble the parallel

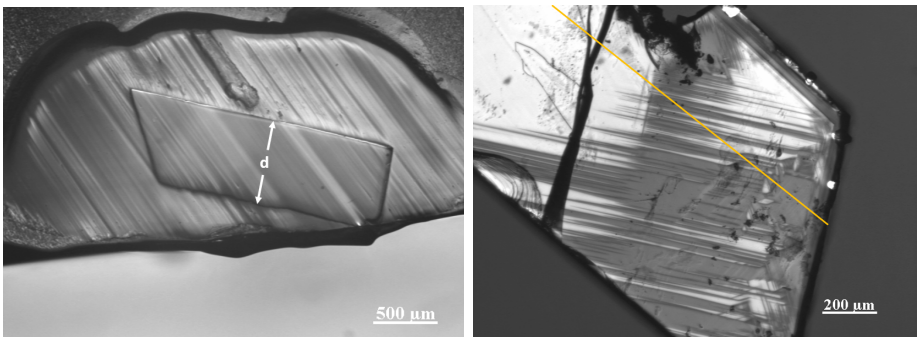


**(a)** **(b)**

**Figure 4.19:** Overview images (a) showing the crystal after the final polishing step with d denoting the distance between the thick and the thin edge of the wedge sample and (b) indication of the edge position within the specimen using PLM.

twinning domains from area A highlighted in the unpolished crystal, being the rightmost area in Figure 4.17 (b). This observation serves as an indication of where the edge lies in the crystal and is in agreement with distances measured in Figure 4.19. Consequently, charged H-H and uncharged T-T domains should be present in the specimen, assuming that the domains are not displaced by the mechanical force applied during the tripod polishing routine.

No further Ga or Ar ion milling was attempted to reduce risk of displacing charged twinning domain boundaries. Neither is it necessary to perform further ion milling thinning if the specimen preparation has been performed successfully.

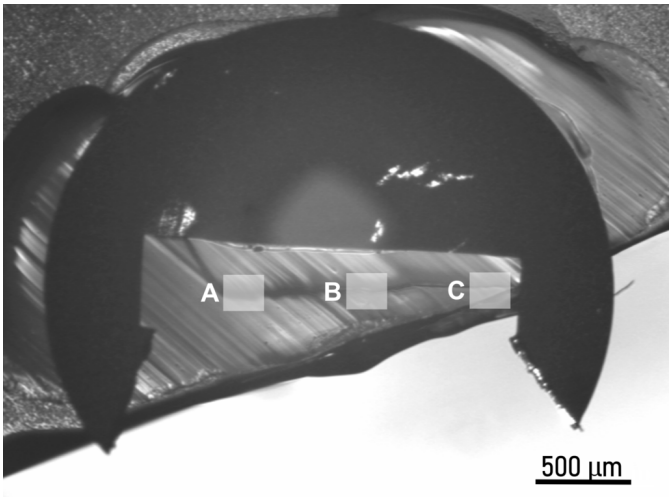


**Figure 4.20:** Overview image of the KNBO crystal attached to the TEM half-grid together with markings of the areas of interest investigated in TEM inspection.

### 4.2.2 Initial TEM and STEM Characterization

Inspection of the KNBO specimen in TEM revealed that the entire edge is electron transparent up to several micrometers away from the wedge edge with the only exception being small areas with induced cracks from the specimen preparation.

In general, the specimen has a low degree of induced damage from the mechanical specimen preparation routine. Therefore, the TEM specimen is observed to exhibit exceptionally high quality with a low degree of defects introduced to specimen edge. However, a large variation in contaminants was observed along the specimen edge, shown in Figure 4.21, displaying area A, B, and C, respectively. Relatively large areas are contaminated by substantial amounts of silica particles introduced from the last polishing step, while other large regions are observed without any signs of contamination. This varies greatly throughout the sample, alternating between contaminated areas and areas of high quality without contamination. Furthermore, the very thin specimen edge exhibits a low degree of bending, i.e. curling up/down, showing minimal thickness variations along the edge, as can be seen from the thickness fringes visible in Figure 4.21 (b). These regular thickness fringes extends over several micrometers into the material and can be observed over large areas without much variation in the fringes, showcasing uniformity of the sample along the edge. As a result of the low degree of bending, the zone axis varies little in position across the specimen, being suitable for domain inspection. Going along the edge, the orientation was kept constant, however the height had to be adjusted with minor changes.

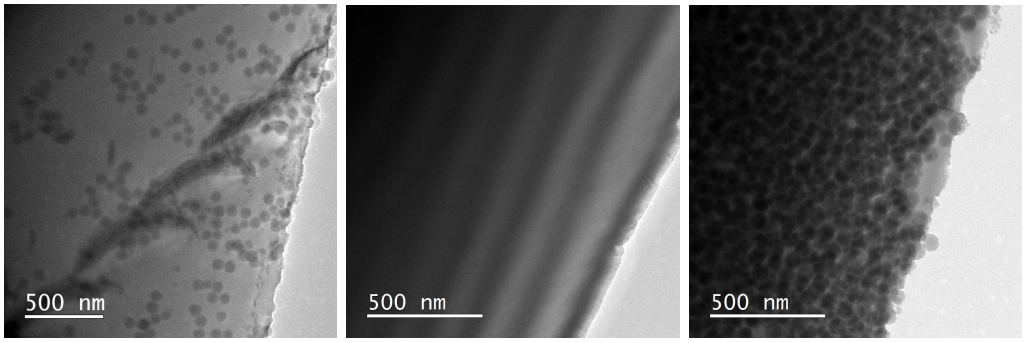


**(a)** **(b)** **(c)**

**Figure 4.21:** TEM BF overview images of (a) A remaining $SiO_2$ polishing particles, (b) B thickness fringes in a clean area of the edge, and (c) C which has high density of $SiO_2$ polishing particles.

Inspections of all three main areas, A, B, and C, revealed a difference in observations of both properties and quality. In general, area A and area C are most affected by the silica contaminants covering areas of tens of micrometers completely, while other areas are seen without a single silica particles over several tens of micrometers. Area B on the other hand consists of approximately 100 micrometers along the specimen edge with exceptional quality, having a high degree of uniformity and no contamination. Comparing the central parts of the wedge to the parts extending towards the corners of the wedge, the most of of the silica contamination buildup appeared to be concentrated towards the corners. All three areas were inspected with low magnification to identify potential regions containing interesting features.

Inspection of area B with BF revealed four anomalies along the specimen edge having the appearance of cracks. In the BF technique, the interfaces are seen as dark lines from the specimen edge and causes shifts and discontinuities of the

thickness fringes across the interface, illustrated in Figure 4.22. These potential twin domain walls are labeled as B1, B2, B3, and B4 based on their relative position within area B and are illustrated in Figure 4.23. Boundaries B3 and B4 are located at a distance of 6.5 $\mu$m apart, while B2 and B1 are approximately 30 $\mu$m apart from both B3 and each other. The potential domain walls were all located within a region of approximately 100 $\mu$m along the edge in area B. All of the boundaries appear parallel along a similar directions, although with some minor variation are seen between the individual interfaces. More specifically, B1-B4 extend closely along the crystallographic $2\bar{3}0$ direction from the indexing scheme in Figure 4.24. Boundaries B2 and B3 extend along similar directions being closest to the crystallographic $2\bar{3}0$ direction, while B1 and B4 has a slight offset, illustrated in Figure 4.22.

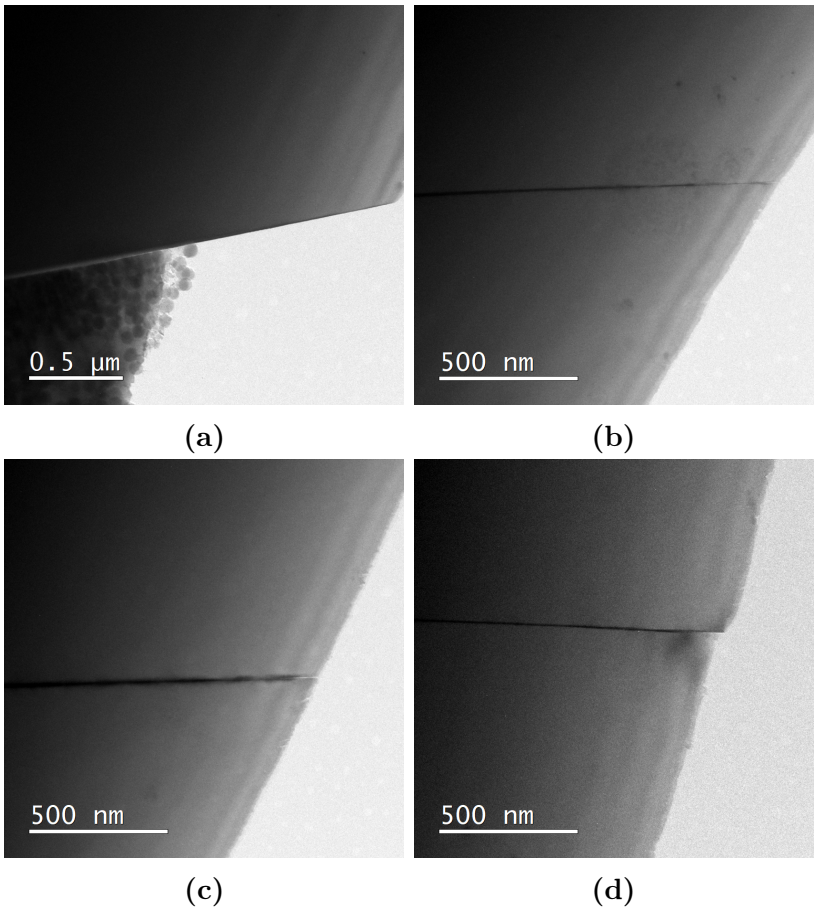


**Figure 4.22:** BF TEM images (a-d) of the four potential domain boundaries. These are labeled B1 to B4. These were in area B and rest of the 1.6 mm long edge did not have such linear lines.

To confirm the crystallographic orientation and to determine and relate structural features to crystallographic directions, a tilt series is presented in Figure 4.24. All SAED patterns are indexed and the relative tilt between the zone axes are noted. In total five zone axes were successfully mapped out within the tilting range for the JEOL EM-31640 Double tilt holder in the x-direction. All zone axes mapped out are higher order zone axes as no lower order zone axes are located

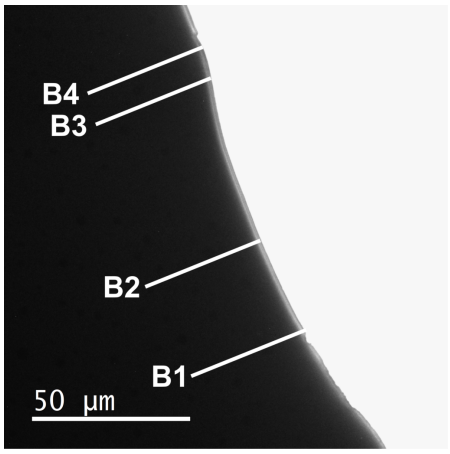


(a)

**Figure 4.23:** Low-mag overview image of area B of the KNBO crystal showing the area containing the four domain boundaries, marked with B1-B4, and their relative positions. Widths are exaggerated for visibility.

within the tilt range of the holder with the given crystal orientation. These zones were indexed using a combination of the relative tilts with the relative distances between the diffraction spots. These were found to match accurately with simulations, illustrated in Figure 4.25, indicating the correct indexing scheme.

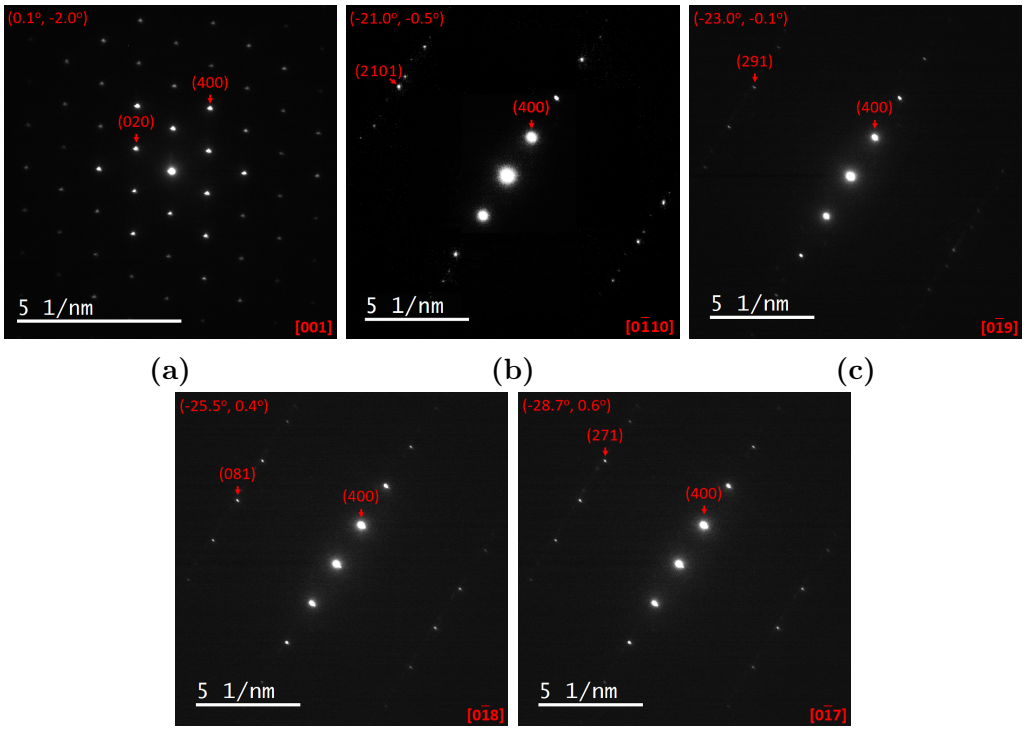


(a) (b) (c)

(d) (e)

**Figure 4.24:** (a-e) experimental SAED images captured from the tilt series together with relative tilts.

Inspecting the satellite spots, being the weaker adjacent spots to (2 10 1) in the [0 $\bar{1}$ 10] zone axis in Figure 4.24 (b), also serve as an indication that the tilt is along the $b$-direction (along the $g_{020}$ diffraction spot), in the crystal as they are relatively parallel with the neighboring spots, while tilting along other directions would cause the satellite spots to be at an angle in relation to the more prominent diffraction spots. By rotating the specimen towards the $b$-direction, the the intensity of (400) and ($\bar{4}$00) is maintained constant. The line of arguments used in this thesis for the indexing scheme presented, correspond well with the direction of the atomic configuration which will be presented in subsection 4.2.3, further strengthening the indexing.

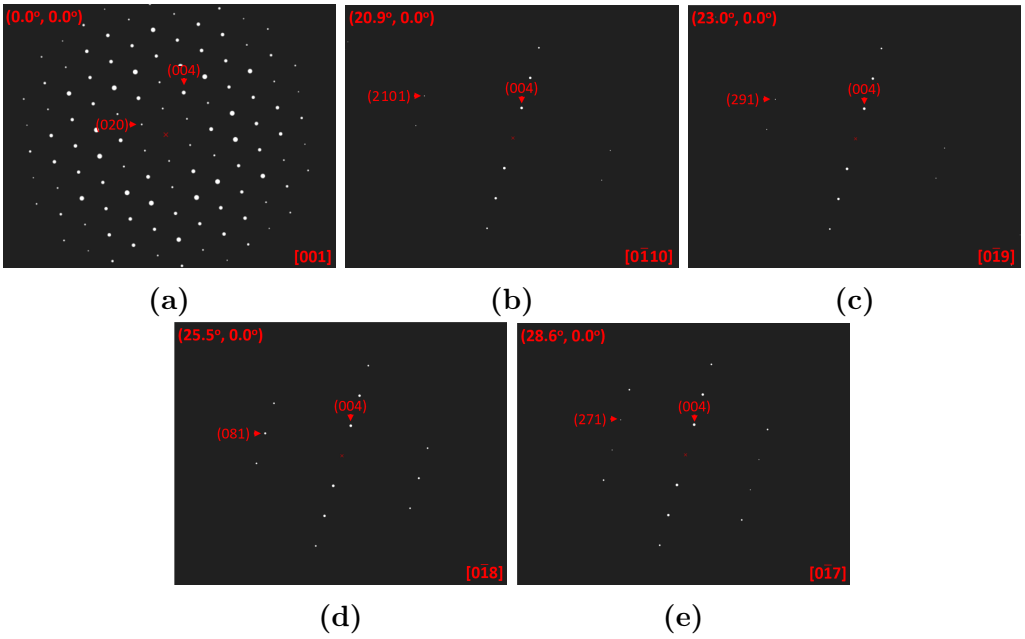


**Figure 4.25:** Experimental tilt series (a-e) together with the relative tilts between the zones and experimental SAED images captured from the tilt series. Note that satellite spots are not illustrated for increased visibility of more intense diffraction spots.

All zone axes were found to match with the simulated diffraction patterns, depicted in Figure 4.25. The simulated diffraction patterns are all given with the relative tilt between the zone axes. There are no apparent deviations between the experimental and the simulated zone axes, which serves as a strong indication that the KNBO wedge assumed to have the crystallographic [001] orientation of the facet of the crystal is correct.

Closer inspection of each of the four boundaries with SAED patterns, revealed no apparent difference in crystal orientation across the boundaries. SAED patterns were captured on both sides of the boundary, as well as on the boundary. Figure 4.26 (a) displays a BF overview image of B4 with the marked locations of each individual SAED patterns. Across the dark interface almost perpendicular to the edge, sudden shifts can be observed in the thickness fringes. Each of the SAED patterns are shown in (b-d), with no apparent difference observed in the differently positioned SAED patterns. No hop in kikuchi lines were observed in CBED patterns across the boundaries. Similar analyses were performed for

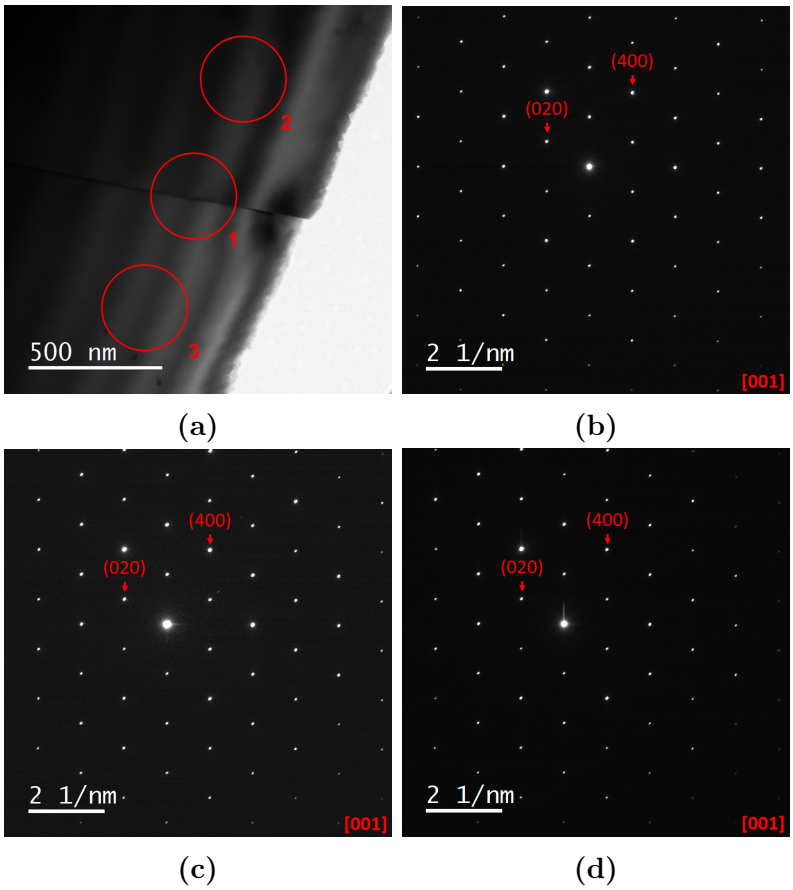


**Figure 4.26:** (a) BF overview image of B4 with the relative positions of SAED patterns marked with 1, 2, and 3, and (b-d) SAED patterns from each location.

boundaries B1, B2, and B3 and are presented in Appendix C. Oppositely to B2-B4, B1 shows a slight misorientation between the opposite sides, being slightly off zone. In some SAED patterns a shift in the diffraction spots can be observed between different positions on the specimen. For each position, adjustments of astigmatism was required to deal with charging effects present close to the edge of the KNBO specimen distorting and shifting the diffraction spots.

Inspection of an arbitrary area long the edge of KNBO with HRTEM shows how, besides the good specimen quality over larger areas, appearance and representation of structural features varies across an increasing thickness, shown in Figure 4.27. Across the image three areas are highlighted, all showing a different representation of the KNBO crystal structure. In the centre of the image the structure resolved resembles the characteristic Nb triplets in KNBO. However, by following the two different directions in the image towards the highlighted areas, the effect of phase contrast emerges. In these highlighted areas the lattice of KNBO appears differently as dark or bright dots. The image is captured having the edge on the right side, such that the thickness increases towards the left in the area imaged, showing how phase contrast varies with thickness.

Each individual boundary was closer inspected at higher resolution using HRTEM. HRTEM, displayed in Figure 4.28, revealed that the boundaries are indeed very sharp and are accompanied by a changes in contrast across the interface. Contrast

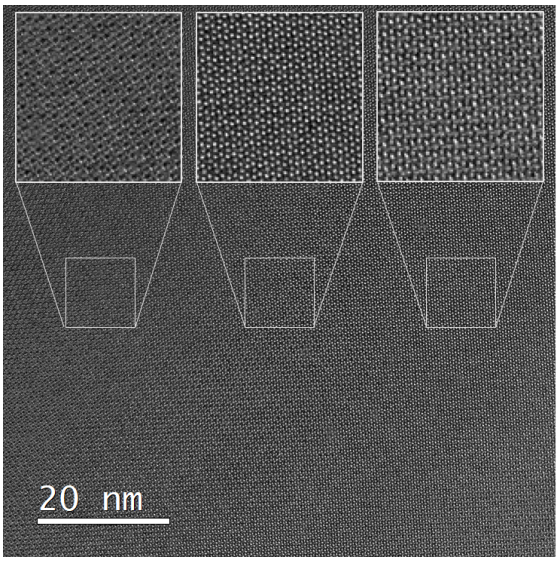


**Figure 4.27:** HRTEM image of an arbitrary area along the edge of the KNBO specimen highlighting how phase contrast variation going from thin (right side) to thicker specimen (left side).

is observed to vary differently for all interfaces. Being more uniform on opposite sides for B2-B4, while B1 is more anisotropic having a darker contrast above the interface than below. Not all of the interfaces exhibit similar characteristics, e.g. interfaces B2 and B3 seems sharper compared to B1 and B4. Across all of the interface, the phase contrast is apparent, showing a sudden change in appearances of the lattice structure. Inspection of Figure 4.28 (d) reveals residues of carbon contamination along the edge originating from the HAADF-STEM analysis. Boundary B1 displays a reduced image quality compared to the other boundaries, as it was acquired at larger thicknesses to reduce the effect of charging and the presence of silica particles. These effects were most prominent along the specimen edge and affected the imaging conditions, ultimately reducing the resolution.

The interesting observations in the HRTEM inspection of the boundaries in Figure 4.28 motivates for a more detailed analysis using HAADF-STEM, which does not suffer from phase contrast variations. This allows for a verification of the details observed in HRTEM giving a more directly interpretable image. Prior to lattice imaging at high magnification, low-magnification HAADF STEM overview images was captured of each boundary. The boundaries can be seen to emerge as a higher intensity compared to its surrounding environment, displayed in Figure 4.29. No obvious strain fields or contrast changes occur in proximity of the interfaces, except for B1 showing a difference in contrast in the opposite sides of the interface. The opposite sides of the B1 interface shows a difference in contrast, as well as silica particles. These particles increase the thickness resulting in a higher intensity, and are also good markers for positioning, being uniform in size. Boundary B1 also shows a difference in orientation, causing the contrast differences observed with BF TEM. The three other boundaries looks more uniform in contrast. Moreover, these well-defined and sharp interfaces can be observed to have a slight curvature in B3 and B4, turning downwards when going towards thicker areas further into the material.

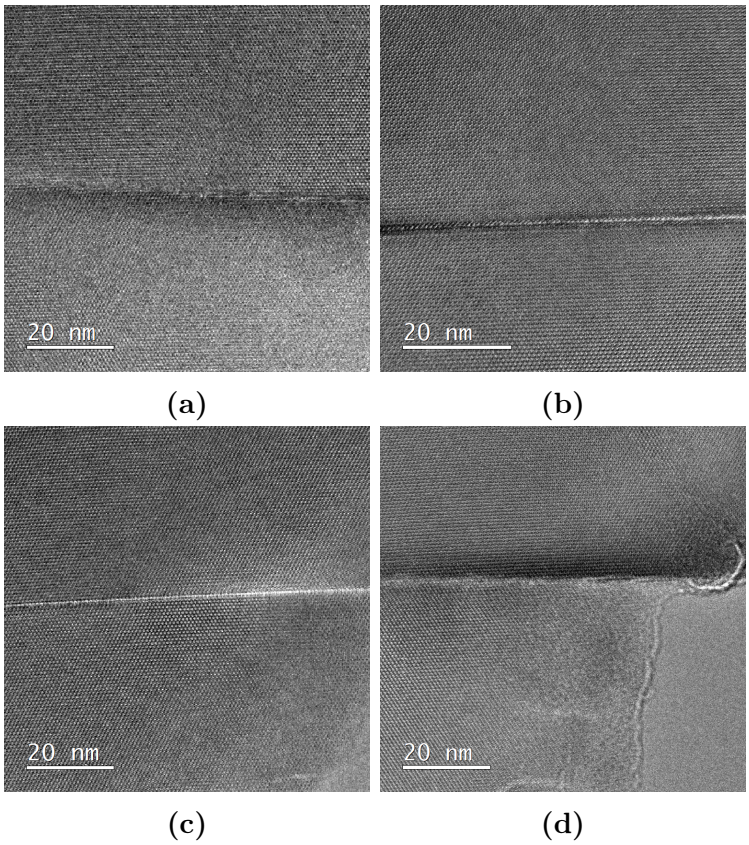


**Figure 4.28:** HRTEM images (a-d) captured of each of the respective boundaries B1 to B4 having the edge on the right side relative to the area imaged.

The boundaries were inspected at higher magnification using HAADF STEM in the uncorrected 2100F microscope. The resulting images of boundaries B1 through B4 are depicted in Figure 4.30. The images show the characteristic Nb-atom column triplets in Figure 2.15 (c), along the atomically sharp interfaces, further strengthening the hypothesis of domain walls rather than cracks, except for B1. In Figure 4.30 (a) B1 is observed to have a difference in focus with a gap separating the opposite sides.

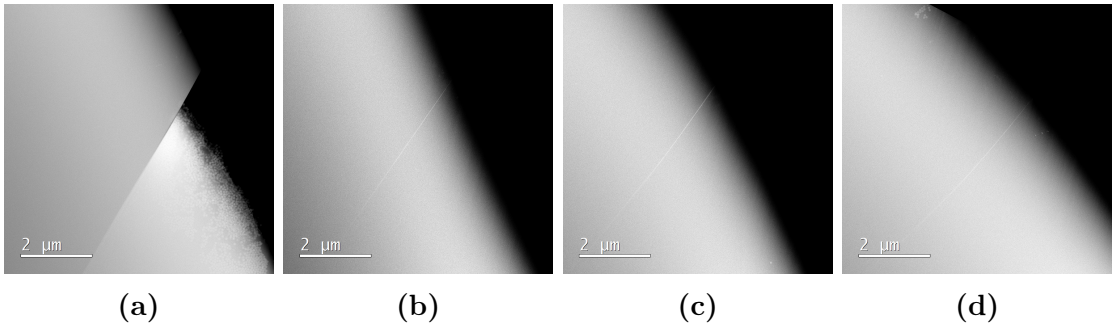


**Figure 4.29:** HAADF STEM overview images (a-d) of boundaries B1 through B4, respectively. The boundaries can be seen to be distinguishable by its higher intensity compared to its surrounding areas.

The remaining interfaces on the other hand, shown in images (b-d), displays atomically sharp interfaces with both sides being in focus simultaneously, recognized by the characteristic Nb triplets. There are several details to take note of in boundaries B2-B4. Boundaries B3 and B4 experience strongly enhanced scattering at the interfaces, increasing the signal causing the bright contrast along the interface. Boundaries B2 and B3 appears to have a dark interlayer, being crystalline, that is not as clearly distinguishable as the surrounding areas, while B4 does not. Inspecting each of the interfaces, B4 can be seen having a slight incline, whereas the boundaries B2 and B3 appears to extend more along a crystallographic direction. In the inclined interface, sudden "jumps" can be seen where the interface switches to the neighbouring triplet at distances averaging around roughly 11-12 nm. B2 and B3 on the other hand are atomically sharp with little variation along the interface. In addition, B3 can be seen to have alternating narrowing and broadening "pockets" along the interface. These pockets can be observed as alternating contrast, appearing to vary the width across the interface. All images suffer from mechanical instabilities as the 2100F is not designed for such resolution. In order to validate these observations and to gain a better understanding of the structural configuration across the sharp interfaces, it is necessary to obtain a higher spatial resolution by employing an aberration-corrected TEM. This will allow for direct imaging of the structural configuration at the interface.

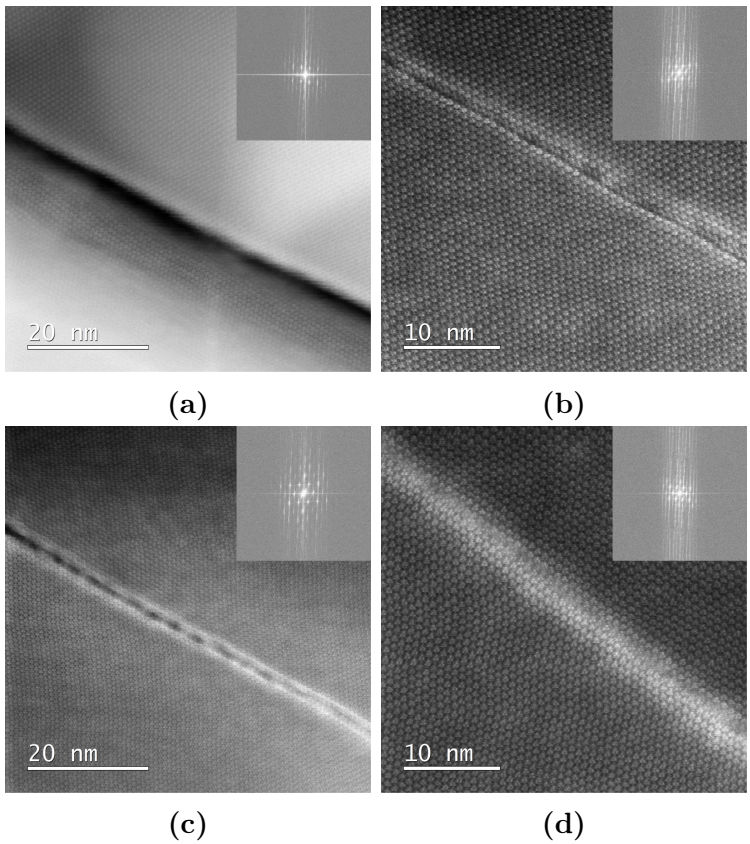


**Figure 4.30:** HAADF STEM images together with their respective FFT (a-d) showing each of the boundaries B1 through B4. All interfaces show slightly different behavior in terms of contrasts and a varying dark interlayer separating the opposite sides.

### 4.2.3 Aberration Corrected HAADF STEM of boundaries

Several interesting aspects prompted for future investigation upon investigating the interfaces in 2100F. To investigate the interfaces with atomic resolution, the ARM was employed to be able to observe the atomic configuration at the domain wall, which can provide interesting insight to the precise atomic arrangement across the boundary. In addition, this gives useful information on defects and strains often accommodated at the interfaces as well as the relaxation of strain in adjacent regions. All data presented in this section is captured with the ARM microscope by Dr E. Christiansen or Dr U. Ludacka.

#### 4.2.3.1 Boundary B1

Inspection of interface B1 with the ARM200F revealed several concluding results agreeing with observations from the 2100F microscope. Figure 4.31 shows a gap separating the left and right side, with absence of signal generated within the gap separating the sides. In addition, both sides can be seen to have a difference in focus, indicating that the sides has a height difference separating them. Observing image (b), the right side can be seen to have a larger variation in height, with only the top right corner being in focus, compared to the left side being evenly focused. This indicates that the right side experiences a bending towards the gap causing it to be out of focus. Inspection of CBED patterns at both sides of the gap also revealed a slight mistilt separating the sides, meaning they do not show the exact same crystallographic orientation. Interface B1 thus shows convincing characteristics of being a crack and will not be further analyzed. However, B1 will serve as a proof that the remaining boundaries are in fact not caused by cracks as they do not exhibit similar characteristic.

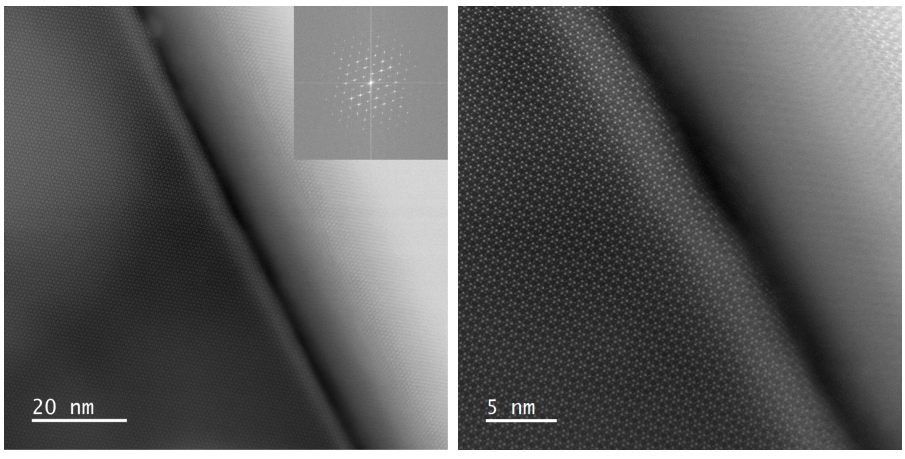


**(a)** **(b)**

**Figure 4.31:** HAADF STEM images captured at two different magnifications, both with camera length 12 cm showing interface B1. Shows bending on right and on left the bright band close to the black gap.

#### 4.2.3.2 Boundaries B2-B4

Investigation of the HAADF-STEM images captured of the remaining boundaries B2-B4 revealed differences and similarities between the different boundaries. In Figure 4.32 (a-c), HAADF-STEM images of B2-B4 shows the general appearance of the interfaces at large scale compared to the interface itself. In general, the appearance of all boundaries are roughly the same at this scale, with some variations in contrast surrounding the region. However, upon closer inspection in Figure 4.32 (d-f), more dissimilarities appear in the structural configuration of the interfaces. In addition, they exhibit different behavior across the interfaces, as will be individually denoted below.

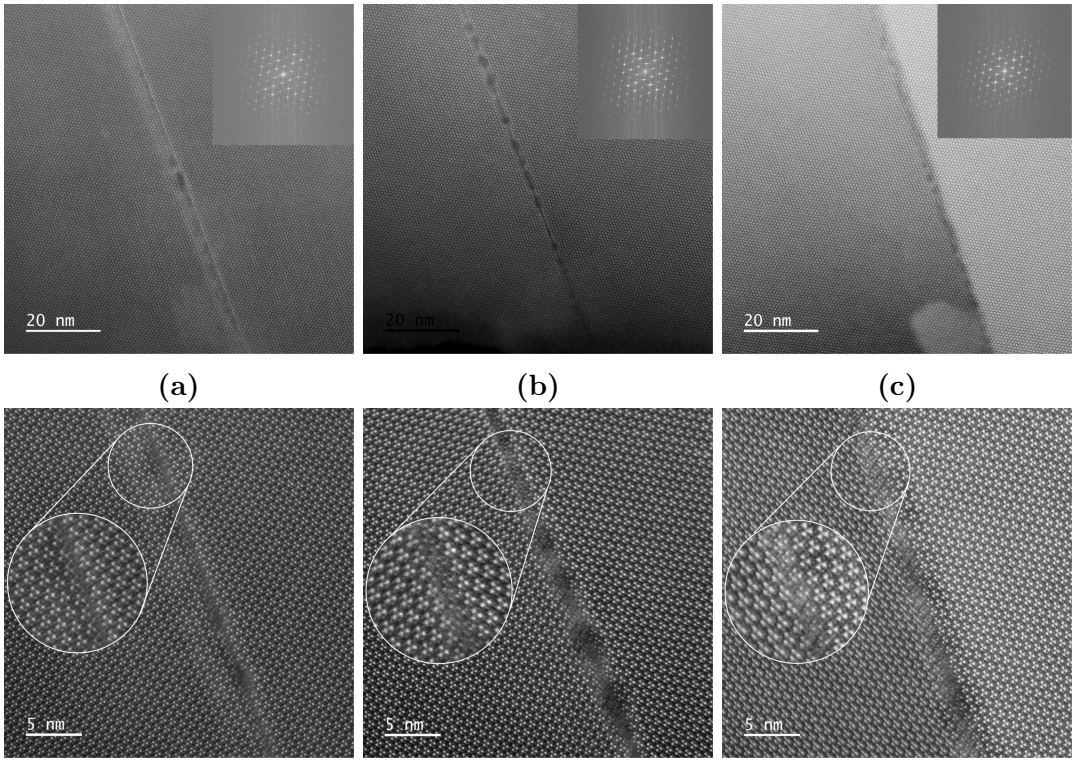


**Figure 4.32:** HAADF STEM images captured with two different magnifications (a-c) with their respective FFTs and (d-f) showing boundaries B2-B4 with each of the interfaces highlighted.

In Figure 4.33, domain walls B2-B4 is shown together with a line along the two polar directions of the twinning domains, corresponding to **a'** and **a"**. The polar domains are seen to intersect the domain wall at an angle of $\sim 60°$, being rotated by 120° across the domain wall. The lines drawn, follow the polar directions, and can be seen to experience shifts upon crossing the domain walls. Following the *a'*-direction across all domain walls (a-c), a shift can be observed in the *b*-direction across the interface as a result of the additional Nb atom columns situated at the interface. The exact direction and sizes of the shifts are rather challenging to quantify based on the images purely as the images are affected by specimen instabilities during imaging. All interfaces exhibit similar behavior in terms of the direction of the shift and in terms of directionality.

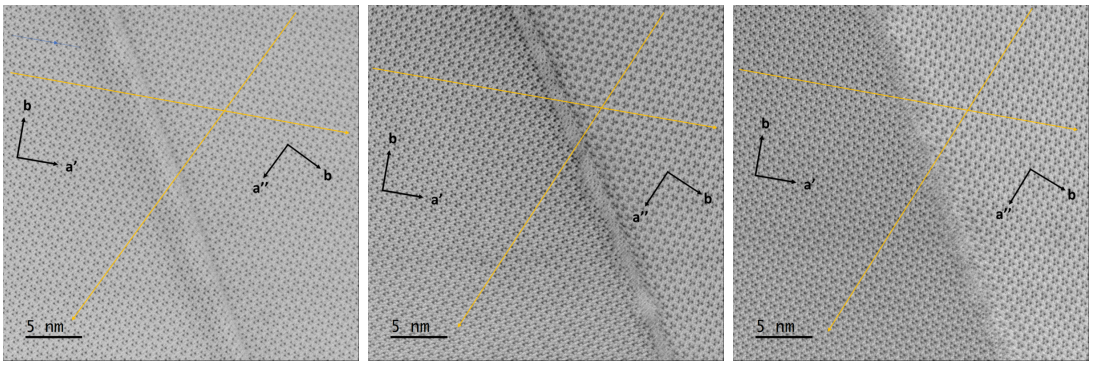


**(a)** **(b)** **(c)**

**Figure 4.33:** BF STEM images (a-c) of B2-B4 showing the atomic shifts by following the row of Nb triplets across the interfaces. Notice that B2 and B3 show similar downward shifts towards the right side, while B4 displays an opposite upwards shift.

**B2** Figure 4.32 (d) shows an atomically sharp image of the B2 interface that closely follows the crystallographic $g_{2\bar{3}0}$ direction. Both sides of the interface are observed to be in focus having atomic resolution with the given defocus, indicating no variation of height across the interface. Looking more closely on the atomic configuration as highlighted in the image, the width of the interface can be observed to span across a single triplet with the addition of two Nb atom columns situated on the right side above the triplet in the interface. By drawing a line through the central atom of the triplet row that pointing towards the interface on the left side and following it across, shown in Figure 4.33 (a), a slight downward shift of $\sim 2$ Å is observed in the $0\bar{1}0$ direction where the line intersects with the upper atom of the corresponding triplet row upon crossing to the right side. In general, the whole interface appears in a similar way, following the same crystallographic direction without exceptions and with no variations in the structural configuration.

Upon correction of astigmatism and focus at higher magnifications, the interface was observed to be slightly affected by beam damage in the magnified. This can be seen as a small "pocket" from which the signal is weaker compared to the remaining interface, illustrated in Figure 4.32 (d) close to the bottom part of the interface. Except from this, no other stability issues were observed upon imaging the interfaces.

Inspecting the images Figure 4.32 (d) and Figure 4.33 (a), one can see a gradual change of contrast due to localized strain variations across a single triplet on the right side of the interface, while it changes across 2-4 triplets on the left side of the interface.

**B3** Figure 4.32 (e) shows an atomically sharp image of the B3 interface that also follows the same crystallographic $g_{2\bar{3}0}$ direction. Both sides are observed to be in focus at the same defocus, indicating no height difference separating the sides. However, in B3 some slightly different behavior is observed in the structural configuration of the interface. Looking more closely on the atomic arrangement of

this interface, one can see that the width of the interface appear to vary along the interface. In Figure 4.32 (b), the alternating contrast can be observed to repeat irregularly down the interface. This alternating contrast along the interface is accompanied by narrowing and broadening of the interface, illustrated in Figure 4.32 (e). In the narrow parts of the interface the atomic structure also spans across a single triplet with two additional Nb atom columns, while within the "pockets" of darker contrast the width can be seen to span across three triplets with the additional columns. These pockets are not due to beam damage, being induced by imaging or aligning and were also visible in 2100F HAADF STEM, which was performed with a lower dose. Oppositely to B2, the additional atoms are situated on the left side of the interface. Despite this, upon drawing a line across the central atoms of a triplet row and following it across the interface, as illustrated in Figure 4.33 (b), a similar downward shift as the one for B2 can be observed where the line intersects with the upper atom of the triplet row on the right side. The shift is along the $0\bar{1}0$ direction, being $\sim 2$Å.

Inspection of the contrast gradient across the interface in Figure 4.33 (b) revealed similar changes on both side with a gradual contrast change spanning across the first two triplets on each side of the interface. The triplet closest to the interface exhibits a more intense contrast compared to an arbitrary triplet in the bulk environment. Around the broadening pockets formed along the interface, the strain contrast is observed to widen somewhat on both sides. In addition, looking at Figure 4.32 (b), the strain contrast increases with increasing thickness by observing the interface from the edge.

**B4** Figure 4.32 (f) shows an atomically sharp image of an interface that follows generally follows the crystallographic $g_{2\bar{3}0}$ direction. However, interface B4 exhibits some differences compared to both B2 and B3. Observing the image it becomes clear that the opposite sides of the interface are situated at different heights, not being in focus at the same time as shown in Figure 4.34. The difference in defocus was determined to be $\Delta f = 6$ nm, corresponding to several unit cells difference in height. In addition, by looking more closely at the interface in Figure 4.32 (f), one can observe that there is a slight incline in the interface, meaning it does not follow the exact same crystallographic direction as B2 and B3. Instead, the interface appears to move in steps separated by approximately 11-12 nm. Between each step, the width of the interface spans across a single triplet with the addition of two atom columns situated at the right side, similar to B2. However, on each step, the interface shifts to the next row of Nb triplets situated beneath the original row on the left side. Upon shifting to the next triplet in a step, the two additional atom columns merges with one Nb atom from the neighboring triplet that was within the interface, before the remaining two Nb atoms from the triplet becomes the new additional atoms in the interface. Subsequently, the interface continues for a certain amount of distance before the procedure is repeated at the next jump. In this way, triplet rows can be seen to cross the interface, being at focus at one position while going out of focus upon transitioning the interface or opposite. Upon following a row of triplets across the interface, as shown in Figure 4.33 (c), an opposite shift is observed compared to the B2 and B3 interfaces. For this interface, a small upward shift of 2 Å is observed in the 010, where a line through the central atoms of a triplet row pointing towards the interface will intersect with

the lower atom of the triplet row on the right side.

Inspection of the contrast gradient across interface B4 in Figure 4.33 (c), shows few signs of contrast changes from localized strain variations in proximity to the interface at low thicknesses. Thicker areas on the other hand show subtle signs of contrast changes in the two to four closest triplets on each side of the interface, seen in Figure 4.32 (c). The contrast transition gradually broadens for increasing thickness, occurring mainly at the right side of the interface.

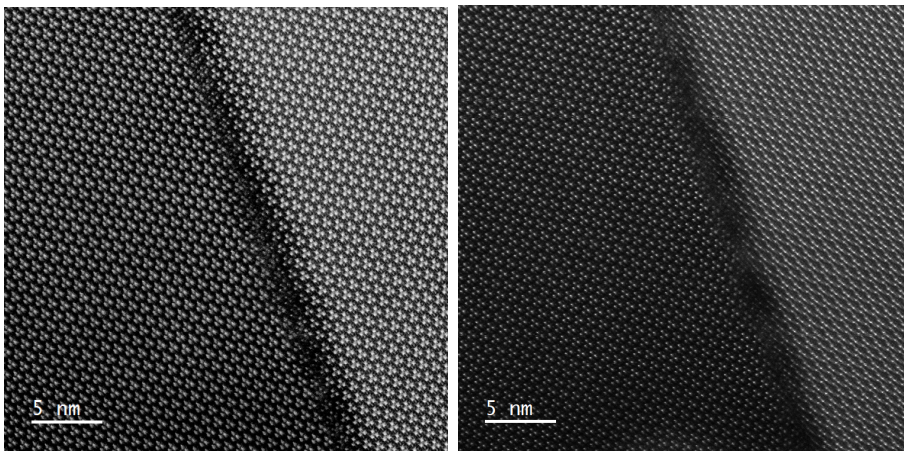


**(a)** **(b)**

**Figure 4.34:** HAADF STEM images (a) and (b) captured with two defocus $\Delta f = 5$ nm and $\Delta f = 11$ nm, respectively. The interface is slightly out of focus in both images, having a gradual transition.

CHAPTER

# FIVE

# DISCUSSION

## 5.1 KMWPO

### 5.1.1 Specimen Preparation

All TEM characterization is highly dependent on the specimen quality. Alteration of the structure and a surface damage layer is deteriorating the quality. Some techniques such as EELS, HRTEM and HR HAADF STEM require thin specimen while other as CBED and EDX benefit from thicker ones. BF and DF contrast can also be highly be sensitive to thickness [30]. In tripod wedges, there is a gradually increasing thickness in a combination with large areas, opening for selective choice of the region for the suitable situation for the technique. The tripod polishing technique thus provides can thus give excellent specimens of a variety of materials [61].The tripod polishing techniques was employed to prepare a KMWPO specimen and was carried out without any challenges, resulting in a high quality millimeter sized long edge specimen. Because of this, the specimen preparation routine can be considered successfully, making the routine a highly viable candidate for TEM specimen preparation of KMWPO. KMWPO has suitable material properties for the mechanical specimen preparation routine, being relatively soft. The routine rapidly removes material and can be prepared into a tripod wedge in an unproblematic manner using the routine inspired by the work of Hunnestad [54], which is further based on the work by Eberg for oxide thin films [55].

External features such as cracks, chipping, contamination, scratches, and bending arise from the specimen preparation routine and can have a detrimental effect on specimen quality. Signs of some effects can be seen in optical microscopy, illustrated in Figure 4.2, while others appear in TEM in Figure 4.5. Some tripod recipes suggest to disregard pieces and completely avoid starting the technique when signs of cracking emerges [61], but in the case of limited amount of material as was the case for this thesis, this was not an option. In order to reduce fatal effects, it is necessary to perform the specimen preparation routine with caution and precision. While performing specimen preparation, it is necessary to be mindful of the plate and the DLFs; the plate should be calibrated to prevent tremors and irregular motions which can break the thin edge. In particular, when polishing with DLFs with roughness less than 1 $\mu$m, specimen and pyrex residues

can circulate the platen back to the specimen as these steps are performed with the polishing lubricant. Therefore, it is necessary to reposition the specimen frequently and reduce the time intervals spent on each polishing step to avoid residues from circulating the platen and harming the specimen. By doing so and removing imperfections introduced from previous steps outlined in the routine, the effects of the imperfections can be minimized. This resulted in that the [110] out-of-plane oriented KMWPO specimen displayed high quality along the edge, with a limited presence of the imperfections mentioned above. Out of these imperfections, the most prominent external features along the specimen was chipping and bending effects. These effects did not directly limit the TEM characterization as a tripod specimen provides millimeter sized areas with electron transparent regions. Therefore, most of the effects from the external features were avoided simply by selecting an unaffected region.

The purely mechanical tripod polishing routine introduces strain to the specimen, causing the edge to bend. The straining mostly originates from the final thinning steps of the routine. For this reason, it is important to avoid applying excessive amounts of pressure and reduce the load on the Allied Multiprep system. During the specimen preparation, it was found to be preferential to have a small load of 50 g or less compared to the 0 g reported in the routine from Appendix A, as this made the micrometer have a higher accuracy, giving better control over the force applied. The strain can in this way be reduced by repeating steps on sub-micron DLFs by adjusting the micrometer to minimize the force applied to the specimen. Gradually, the bending effect will be minimized if this is also applied to the final polishing step using colloidal silica nanoparticles. However, repeated polishing on the step using colloidal silica particles was observed to increase contamination, i.e. silica particles on the surface along the specimen edge as not all particles are removed by the cleaning routine subsequent to polishing. The result is thus a trade-off between specimen bending and contamination, which should be considered upon performing the final thinning. Specimen preparation and artifacts are highly material specific, with each material having a slightly different optimal procedure to prepare specimen.

Tripod specimen prepared with the general workflow described in Appendix A can in some cases experience charging phenomenons either caused by the materials poor electrical conductance or by an insulating layer of glue used for the attachment of the tripod wedge to the TEM half-grid. In any case, the insulating layer of glue have frequently restricted proper electrical connection between the crystal and the copper grid, increasing charging effects in the electrically isolated specimen. In order to mitigate charging effects, several measures can be applied to reduce this effect. Commonly used methods to reduce charging phenomenons in SEM specimen is depositing a thin conducting material directly onto the crystal or alternatively applying silver paste to the material. However, for TEM specimen this layer have to be amorphous, low Z (carbon can be removed by plasma cleaning) and very thin (few nanometers) [62]. It is possible, but will require a good vacuum system, which was not available in this project. Therefore, silver paste was the preferred method for reducing charging effects in this project, as it can be applied to electrically connect the crystalline sample to the grid, without having to deposit a thin conducting layer on the specimen that affects the electronic channeling.

Gentle Ar ion milling (on PIPS with a small angle applied) can be performed with short time intervals of 3 minutes on voltages between 0.5-3.0 kV on tripod specimens as a final thinning process when the wedge is too thick and do not exhibit electron transparency or to remove contamination along the edge. However, the process introduces amorphous regions on the outermost part of the surface and at the edge. It should therefore be avoided unless absolutely necessary as it can introduce artifacts and reduce the quality of the specimen as the quality from using ion milling techniques is highly dependent on the material properties [63]. Eberg's paper showed that ion milling even at short time intervals and low energy can introduce phase transformations in thin oxide films [55].

To conclude, the tripod polishing routine is a highly capable method for preparing TEM specimens of KMWPO. In relatively short time, the technique allows for selective orientation of the specimen and large electron transparent areas, given that it has a known crystallographic orientation. Using the general workflow described in Appendix A with the alterations above, millimeter sized high quality electron transparent regions can be produced with minimal contamination. As a final step ion milling can be used for the final thinning of the specimen edge, but was not required for KMWPO.

### 5.1.2 TEM Characterization

The results presented in this thesis are the first TEM studies on KMWPO, as far as the author can confirm. Previously, the material has only been characterized on micrometer scale, utilizing techniques such as Brillouin scattering, raman scattering, and PLM [33, 34, 39]. These studies reported that KMWPO exhibits highly interesting multiferroic properties, with the appearance of complex twinning domains at room temperature. These complex twinning domains were located within the [110] oriented specimen, shown in Figure 4.4, being dominated by mainly alternating stripe domains with additional oscillating zig-zag domains. The most distinct contrast difference is observed for the zig-zag domains measured with the out-of-plane configuration in Figure 4.4. The alternating contrast is caused by a variation in deflection of the cantilever in terms of amplitude and phase between adjacent domains, indicating opposite polarization directions in-plane. Measurements thus give an indication of the alternating polarization, however with one degree of freedom. Meaning it forms at an angle in relation to the domains.

In this project, the results presented combined SPM performed on the bulk crystal Figure 4.4, BF TEM, SAED diffraction, HRTEM, HAADF STEM, and HR HAADF STEM to characterize a [110] oriented KMWPO specimen. A tilt series was successfully mapped out for the material, confirming the crystal orientation with complementary kinematic simulations. SAED and simulated diffraction patterns matched and it is concluded that it is the triclinic form of KMWPO. Also HR HAADF STEM show pattern of W columns as expected for this phase, shown in Figure 4.15. The tilt directions from which the orientation was mapped out for the project were chosen due to the more distinct kikuchi bands along the $g_{1\bar{1}1}$ and the $g_{1\bar{1}0}$ directions, making it more practical to tilt along the bands due to their increased visibility. The kikuchi band stretching parallel to the $g_{001}$ direction proved to have a poor visibility and was therefore avoided as it would require a large condenser aperture and intense focussed probe, resulting in gradually

increasing amorphization and reduced visibility of the kikuchi band.

General TEM inspections revealed a varying presence of intriguing microstructures with interesting aspects along the large specimen edge. This involved the presence and absence of the structural features reported in Figure 4.8. The microstructures are dominated by the stripe domains, most likely being the stable lowest energy configuration in the material. Because of the varying presence, a TEM characterization of KMWPO requires a large specimen to obtain a representative picture and for this study to have domain walls in the area that can be studied by TEM. SAED patterns were captured across interfaces and within the features such as vertical, horizontal, and needle-like features, revealing no apparent difference in crystal orientation. The alternating contrast must thus be caused by other reasons than crystallographic orientation. The contrast is believed to be caused by the ferroelectric domains, similar to what was observed in Figure 4.4. These are strong indications of a polarization direction in-plane, and is the cause of the local microstructures. This implicates that the material locally subdivides into specific regions or domains within the single crystal that exhibits different scattering properties originating, possibly from the spontaneous polarization.

These features exhibit a mixture of behavior with a variety in terms of directions, sizes, and their presence across the specimen. Horizontal features dominated over thinner regions, possibly being related to the dominant features measured in PFM measurements in Figure 4.4 on [110] out-of-plane bulk KMWPO. Most of the behavior qualitatively, shape and size match from TEM characterization and PFM measurements, strengthening the belief that KMWPO shows ferroelectric domains with [110] out-of-plane. However, there is a slight difference where interfaces separating features displayed both straight lines and curvatures in TEM, while they appear rather straight in PFM. The interfaces widths also vary more in TEM, being either sharp or broad, while they appear to be more uniform in PFM scans in Figure 4.4. In addition, minor directional changes such as the one observed in the HAADF-STEM image in Figure 4.14 accompanied by small changes contrast within the features are observed in TEM. This great variety of interesting characteristics displays the behavior of these structural features varies within the material, proving that more work is needed and that the experiments to investigate them needs refinements. TEM allows to inspect these interesting features with higher spatial resolution than has been reported and could give insight to the atomic structure of these features. However, high magnification is high dose and beam damage could be a limitation, e.g. Figure 4.16.

Investigation of horizontal features with DF imaging revealed contrast shifting between adjacent regions. In Figure 4.10, selection of diffraction spot $1\bar{1}0$ and $\bar{1}10$ enhanced the contrasts, causing different features and regions to light up. The regions experiencing an enhanced contrast are localized and separated from neighboring features by the interfaces in Figure 4.10. For example, the upper left feature was seen to be highlighted from the $1\bar{1}0$ spot in addition to nearby areas surrounding the features, while the lower neighboring feature lights up from the $\bar{1}10$ spot together with other areas located closer to the edge. Diffraction spots 001 and the $00\bar{1}$ did not reveal similar behavior, but was characterized by more uniform scattering. One possible cause for the behavior observed can simply be a combination of thickness and bending effects along the specimen edge. However, the most plausible explanation is that local contrast variations are domain

contrast originating from charged domains and that $1\bar{1}0$ is the polar direction. The spontaneous polarization is believed to affect the scattering conditions, giving rise to interference effects, providing indications on the polarization direction. [110] in-plane giving strong contrast in PLM could indicate the same. Thus in the current view direction, small regions of these domains could be repoled by the electron beam into a single domain [64, 65, 66]. This agrees well with PFM measurements, indicating that the polarization direction is in-plane with one degree of freedom relative to the stripe features in Figure 4.4. This should also be verified by performing dynamical simulations of electron CBED patterns to determine the possibility of observing domain contrast in the material [67, 68].

As the diffraction spots 001 and the $00\bar{1}$ did not exhibit similar contrast switching of structural features upon selection of the diffraction spots in DF series, it could indicate other causes for the alternating contrast observed with conventional TEM in Figure 4.8. One plausible explanation is that the change of contrast is attributed to twinning domains originating from the crystal growth. Twinning domains have been reported for a [001] oriented KMWPO in [39] to exhibit complex twinning structures in multiple directions. During crystal growth, atoms attempt to align in order to reduce the overall energy of the system, where alternative favorable orientations could affect the crystal structure, symmetry, and growth conditions [7]. Formation of twinning domains show an increased probability to occur for slower cooling rates, which characterizes the Nacken-Kyropoulos technique used for KMWPO, with an initial cooling rate of 0.5 K/hour, explained in subsection 3.1.1. Therefore, it is believed that the alternating contrast of vertical features aligned with the $[1\bar{1}0]$ direction could be attributed to the formation of twinning domains. There are multiple types of twinning, some of which can cause local variations in crystal structure or even break the conventional symmetry of the material, thus affecting its properties [69]. Depending on the type of twinning, this could alter the material properties sufficiently to cause the alternating contrast through changes in the scattering conditions of adjacent vertical features.

To further investigate the polarization direction, off-zone DF series was attempted in a neighboring region from the DF series by tilting the specimen (-2.7°, 5.1°) in the x- and y-direction, to maintain the diffraction spots $1\bar{1}0$ and $\bar{1}10$ constant to enhance the contrast differences. Through performing an off-zone DF series, the diffraction spots are enhanced while suppressing the signal from surrounding regions and the 001 and the $00\bar{1}$ directions. The result of the off-zone technique thus optimize the scattering associated by the horizontal features. However, the off-zone DF series did not show the same convincing results as the on-zone DF series. In Figure 4.11 (b) the right side of the needle is highlighted, whereas in (c) a more uniform scattering can be observed together with enhanced scattering from the needle feature. This is most likely caused by thickness effects, as the thickness of the specimen increases towards the left side of the image. As a result of the thickness increasing, the specimen absorbs a larger fraction of the electrons, ultimately reducing the signal at thicker regions. No apparent scattering differences are observed in the form of highlighted regions, other than the right side of the needle feature in Figure 4.11 (b). These results are less convincing compared to the on-zone DF series as there is no apparent contrast switching upon selecting the $\bar{1}10$ diffraction spot. Only the needle has an enhanced contrast upon selection of the diffraction spot, while a more uniform intensity is observed in Figure 4.11

(c). This either indicates differences in scattering properties between horizontal features and needle features or similar scattering conditions for the area. Further work could address this by doing scanning precession electron diffraction with post processing of a virtual aperture to create virtual DF images.

Further characterization of structural features in the aftermath of exposures to high dosage techniques such as DF and CBED imaging proved to be challenging as the specimen experienced gradual degradation of quality within the exposed region. DF imaging is a higher dose technique that was observed to gradually break down the material over time creating accumulation of beam damage. This gradual transition ultimately resulted in total amorphization of the area exposed to the electron beam. The gradual weakening signal of the region exposed in the off-centered tilt series is shown in Figure 4.11 (c) by its worse signal-to-noise ratio. The material thus is believed to undergo a structural change due to radiolysis, originating from the material's poor ability to dissipate the energy introduced from beam-specimen interactions. As a result, the material accumulates heat and defects, ultimately burning a hole in the specimen if the beam is sufficiently converged, causing complete amorphization of the exposed region.

The result of amorphization in regions containing structural features was that structural features were found to disappear or shift. In the aftermath of such structural changes, visible changes had occurred within the area exposed to the intense electron beam. Surrounding regions to the area affected by the beam damage experienced complicated contrast changes, depicted in Figure 4.12. After exposure, the amorphous areas shows a higher intensity in the BF mode, while surrounding regions unaffected by beam damage shows unrecognizable contrast without the presence of structural features. This is most likely caused by phase changes and chemically induced modifications. The amorphization is also believed to cause chemical changes in the surrounding regions causing the local contrast variations.It is possible to make speculations over the mechanisms for these changes, but this would be highly complicated as the readjustments appears to be random.

The general TEM characterization involves several analyses of the features observed from general observations of the material. These analyses prompted for further detailed analysis using lattice imaging techniques such as HRTEM and HAADF-STEM. However, increased resolution is often associated with an increased electron dose. Upon investigating this material, cautious consideration is required, involving careful planning of workflow and experimental work. Further investigation of KMWPO requires a specimen of sufficiently large size to have an abundance of features available for characterization. This makes specimen preparation techniques such as FIB lamellas, typically 5x5 $\mu m^2$ area and damage is higher, quite challenging due to its reduced area and the material's susceptibility to beam damage.

To summarize, large, high-quality TEM specimens can be made and medium conventional TEM imaging and electron diffraction in line with PFM indicate the presence of domain walls in [110] oriented triclinic KMWPO. Even though the material experiences high beam sensitivity, lattice imaging in TEM and STEM mode is attempted.

Inspection of the structural features with HRTEM revealed the possibility of characterizing the features using high resolution techniques upon limiting the dose. Figure 4.13 displays HRTEM images, from the interface and from areas within

a structural feature. Both areas showed stability upon using a relatively broad beam in HRTEM, with no signs of gradually reduced signals before converging the beam additionally. Therefore, it is of importance to understand the beam damage mechanisms for both static broad beam and scanning mode and to determine the critical dose to study and understand features in greater detail.

Because of the challenges related to interpreting HRTEM images due to the phase contrast being sensitive to the imaging parameters, a more directly interpretable imaging technique was employed, namely the HAADF STEM technique. This technique shows a better intensity difference than BF TEM as varying coherent diffraction effects are not collected on the detector. Figure 4.14 showcases features of different contrast along the edge of the KMWPO specimen, resembling the structural features observed with conventional TEM. Since the directions of the structural features correspond with the ones observed in TEM mode, there is reason to believe that the features correspond to the ones observed with conventional TEM. This agrees with the belief that the features are separate regions displaying different scattering conditions. Vertical lines, rarely seen to extend fully towards the specimen edge, are observed as sharper than the horizontal ones traveling perpendicular to them. Horizontal lines are not observed to be as distinct and occur with the same frequency in the HAADF STEM technique compared to conventional TEM, while vertical features have an increased visibility. Therefore, inspection of the atomic configuration within each area could give insight to different material properties separating the structural features.

As Rutherford electron scattering shows a close to $Z^2$ scattering dependency as explained in section 2.4.4, and we in this orientation have K, Mg, W, P, and O columns. W has atomic number $Z = 74$, and would therefore appear brightest and dominate the scattering onto the detectors in the HR-HAADF STEM technique. Increasing the magnification to achieve lattice resolution with HR-HAADF STEM allowed for lattice imaging. Despite the image shown in Figure 4.15 being relatively noisy, a filtering of the signal in FFT followed by inversion reveals structural details in the material. These details closely resembles the highly scattering W atoms participating in the alternating chain containing structural units $[WO_6]$, while the $[MgO_6]$ units are not visible. The unit cell, corresponding to the the distance between two wave tops, has lattice parameter $c = 10.74$Å while measurements from Figure 4.15 estimates the same distance to be $\sim 11.0$Å, being 2.5% of from the actual value. In further work, lattice imaging should be performed with an aberration-corrected microscope, but with a reduced dose, e.g. by the SmartAlign function [70].

This showcases the possibility to achieve lattice resolution, on a non-corrected FEGTEM, using relatively low dwell times of 3 $\mu$s. Scanning mode deposits the energy to a more confined region and is more affected by momentum transfer and knock on damage, being more transient than static exposures [71]. The material appeared to be relatively unaffected by a single scan, but experienced a gradually increasing beam damage from repetitive exposures. This agrees with previous observations that the energy introduced from the electron beam is dissipated poorly throughout the material. Meaning the material is not completely damaged by a single exposure of the electron beam, but is affected by an accumulation of beam damage over a series of exposures. Therefore, the damaging mechanism could be a combination that involves accumulation of heat and radiation damage causing

defects such as vacancies, interstitials, and dislocations.

Using the imaging conditions in search mode, the threshold limit was not surpassed, with no apparent beam damage observed. However, upon exceeding the threshold limit, shown in Figure 4.16, the material can be seen to accumulate extensive amounts of beam damage from the increased electron dose. Based on these scans, rough estimates can be made for the threshold dosage. With the given scan conditions in Figure 4.16 (a), the imaging conditions are still below the threshold, showing lattice fringes in the start of the scan, but is affected by accumulation of beam damage and heating as the beam is allowed to scan further. Further increased dwell time and scan points resulted in devastating structural changes to the material. In Figure 4.16 (b), the beam can be seen to completely burn through the material in certain locations due to excessive beam damage. Reducing the amount of electrons per area or adjusting the scanning pattern is therefore a necessity to perform a complete scan to let the material dissipate the energy introduced from beam-specimen interactions. A relatively uncomplicated solution for this would be to insert the smallest aperture available at the microscope, being the 10 $\mu$m condenser lens aperture, but this comes at the cost of a reduction in spatial resolution, being estimated from the Rayleigh criteria as 1.5 Å by ignoring noise and vibrations. Low dose STEM is conventionally done by reducing pixel dwell time or probe current to stay under the threshold dosage. Reducing the electron dose also affects the signal-to-noise ratio, increasing the need for more sensitive detectors. More sensitive detectors can provide better signal-to-noise ratios to open for more efficient imaging requiring fewer electrons per picture. The overall performance of a detector strongly influences the image quality, allowing for a reduction in electrons per $Å^2$. Therefore, a proposition for further work is to gain additional structural information on the features within the material using lower electron dose techniques in a combination with higher efficiency detectors [71, 72]. This could give interesting information with sufficient resolution while overcoming challenges with beam damage.

To make concluding remarks, this thesis provides the first ever TEM characterization presented on $K_2MgWP_2O_{10}$ (KMWPO). The characterization presented includes SPM, conventional TEM, diffraction, simulations, HRTEM, HAADF STEM and HR HAADF STEM as well as the challenge of beam damage. Correlated microscopy revealed parallel equidistant stripe domains, as well as oscillatory domains, resembling observations made with TEM. These techniques revealed several structural features, found to extend along the crystallographic $(1\bar{1}0)$ and the (001) direction. Investigations revealed that the material is highly beam sensitive, limiting the possibility of performing analyses using high dose techniques. Despite this, lattice resolution has been achieved using static broad beam and scanning mode, showcasing the possibility to do analyses with high spatial resolution. As this thesis presents a general and first-ever TEM characterization of KMWPO, much work remains to be done on the material, exhibiting intriguing properties both in SPM and TEM. Suggestions for further work has included determining the critical dose, careful planning of experimental setup, and acquisition of structural data using reduced dose techniques in combination with higher efficiency detectors. Further data acquisition should be combined with simulations to provide a theoretical reference that can be compared to the experimental data to give a comprehensive interpretation.

## 5.2 KNBO

### 5.2.1 Specimen Preparation

The specimen preparation routine for KNBO was somewhat different to that of KMWPO with the main interest of the material being the charged H-H domain walls as their density is low and earlier tripod preparation [50, 52] on random areas did not reveal them, correlated PFM-TEM was required. Correlated PFM-FIB prep was attempted in the group of Dennis Meier, but the final lamellas revealed no domain walls in them. Because of this, the objective for the specimen preparation was the presence of the charged twinning domain walls along the specimen edge, making it a highly site-specific specimen preparation. This was achieved in the specimen preparation by using correlated microscopy approach using techniques such as PLM and PFM. These techniques successfully mapped out the domain structure of the polished surface, as can be seen from Figure 4.17 and Figure 4.18, making it possible to locate the area of interest containing charged twinning domains within the crystal. The selected region of interest, containing the the recognizable charged needle in Figure 4.18. The wide 8 $\mu m$ needle was measured in terms of distance from the bottom side of the crystal, being the thick side of the tripod wedge. In this way, optical microscopy could measure the distance from the bottom side of the crystal between each polishing step, allowing for a gradual removal of material until the region of interest was reached. Gradual removal of material was performed with extreme caution not to loose the targeted charged domain wall. Therefore, several rounds of polishing was performed with the 0.1 $\mu$m DLF using the polishing lubricant to limit the amount of material removed in the final inclined polishing step to accurately stop prior to the end point was reached. To avoid unnecessary damage to the specimen, it was re-positioned radially after each polishing step to avoid residues to circulate the plate and harm by impact of debris. Upon closing in on the area of interest, the final polishing steps were performed using silica particles to remove the remaining material until the end point was reached.

Characterization of such interfaces with atomic resolution requires sufficiently high specimen quality to not be overshadowed by imperfections in the crystal. By performing all steps with this level of accuracy and caution, a [001] oriented KNBO specimen was successfully prepared showing a remarkable quality. The specimen exhibit an extremely low degree of specimen preparation artifacts, with the only limiting effect being silica particle contamination, especially towards the edges of the 1.6 mm specimen edge. A complete absence of silica particles can be seen in Figure 4.21, while other areas are completely covered across large regions of the specimen. Fortunately, silica contamination did not cover the region of interest that contained the features B1-B4. Other external imperfections that can have a detrimental effect on the specimen quality was barely seen across the millimeter sized specimen, with external features such as cracking, chipping, bending and other effects being almost completely avoided across large areas of the specimen. The specimen did not bend, enabling to navigate over long distances without nearly no reorientation. However, the specimen height required height adjustments when moving over the specimen. Along the approximately 100 micrometer region in area B containing B1-B4, these effects were minimal with close to no bending

contrast observed along the edge. This opened up for the possibility to navigate through 100 micrometers along the specimen edge, with only minor adjustments in height or defocus necessary to maintain lattice resolution. These results really showcases the capability of the tripod polishing routine to prepare specimens of impressive quality.

The only specimen preparation artifact that affected the specimen quality was the contamination. Using the tripod polishing technique and finishing with the silica particle polishing step, there will almost certainly be some level of contamination along the specimen edge. However, there are ways to reduce this contamination. One of the ways to reduce the presence of silica particles can be to reduce the amount of time spent on the last polishing step utilizing silica particles. However, this becomes a trade off as a prolonged time with this polishing step also determines the final quality of the specimen. Therefore, sufficient time should be spent on the final polishing to remove the remaining material to increase specimen quality while also avoiding unnecessary repetitions of the step. Another way of reducing the silica contamination is the cleaning procedure that includes soap applied by cotton buds. One possible way to improve the contamination is to adjust the cleaning procedure by doing it more thorough and applying a larger force with the cotton buds. This might remove additional silica particles, but can also harm the specimen, causing it to shatter and should therefore be performed with care.

Specimen preparation utilizing focused ion beam (FIB) or ion milling has as of now not been successfully performed for the same site-specific specimen preparation as this project. FIB lamellas have been produced with site-specific specimen preparation by the employees at the group of Dennis Meier at NTNU, but non of the lamellas had the imaging on the ARM had a presence of the desired domain walls. A plausible explanation for the absence of charged domain walls is that incident ions induce domain motion due to the strong beam-specimen interactions. If a sufficiently large electric field can be allow to build up via surface charging, domain motion can be induced in response to the high electric fields [73]. These techniques utilizing a sputtering effect might also dissipate sufficient energy within the specimen to cause domain wall motion by overcoming the pinning force of the domain wall and can in these highly site-specific specimen preparations be a rather challenging specimen preparation routine.

To conclude, the tripod polishing routine is a highly capable method for preparing TEM specimens of KNBO. A site-specific specimen preparation using correlated microscopy techniques was successfully performed of the charged H-H domain walls. With sufficient accuracy and caution, high quality electron transparent millimeter sized regions can be produced with minimal specimen preparation artifacts. The results achieved for the [001] KNBO specimen showcases the capability of the site-specific tripod polishing routine to prepare specimens of sufficient quality for atomic resolution with minimal specimen variation. The specimen displayed electron transparent regions across the entire specimen edge, with high uniformity and extremely low variations of crystal orientation.

### 5.2.2 Initial TEM and STEM Characterization

There has previously been performed and reported some TEM characterization of bulk KNBO and the uncharged twinning domains [50, 52]. Recent developments on KNBO with PFM and EFM have revealed the presence of charged domain walls with the H-H configuration, as shown in Figure 4.18. In Figure 4.18 the EFM scan highlighted in the PFM scan measures electrostatic forces difference across one of the charged H-H domain walls, while no electrostatic forces are measured across the T-T domain walls. The potential difference measured across the H-H configuration compared to its corresponding T-T configuration confirms the presence of charged domain walls. This is a highly interesting property of the material that is caused by the three symmetry equivalent directions in the high temperature phase of the material. Investigation of such H-H twinning domain walls at high resolution is highly interesting as it could provide insight to how the material properties are related to the crystal structure. Such insight is absolutely necessary for potential applications in devices and could result in advances in the field of charged domain wall engineering, although strictly speaking the charged domain walls are twin walls rotated by 120° relative to each other, illustrated in Figure 2.16.

Investigation of the domain walls in the uncorrected 2100F microscope was performed as initial work prior to the aberration-corrected ARM microscope. In the 2100F microscope, techniques such as BF and DF, SAED, CBED, HRTEM, and HAADF-STEM were employed to analyse the positions of the features B1-B4, being the potential domain walls. It was shown that conventional TEM and HAADF-STEM could successfully be performed for investigation and localization of the charged domain walls. Domain walls could initially be detected as anomalies in BF imaging, with similar appearance as cracks and can also be seen to cause disturbances in the otherwise uniform thickness fringes. BF is thus an optimal technique for identification of domain walls before further investigation.

From the SAED patterns in Figure 4.26, no apparent differences in diffraction patterns were observed across the linear features B2-B4, while a slight misorientation can be seen from the intensity variation for B1 in Figure C.1. Therefore, there is no indication of a change in crystallographic orientation, despite expecting a rotation of 120° across a twinning domain wall. SAED patterns from each side should in theory show a 120° rotation of the diffraction pattern from the [001] zone axis results, but the diffraction pattern seemingly becomes mapped into itself with only minor differences in distances distinguishing the diffraction spots from one another. Unfortunately the distances separating the diffraction spots are close to indistinguishable for the 400 and the $230/2\bar{3}0$ spots, differing only 0.0005 $nm^{-1}$ in distance, as the crystal exhibits a close to 3-fold symmetry in the [001] direction which is lost in the transition from its high symmetry phase down to room temperature phase.

Distinguishing the SAED patterns across a domain wall is further complicated by the presence of charging along the specimen edge that causing a distortion of the diffraction spots. Despite applying silver paste to electrically connect the KNBO crystal to the copper grid some degree of charging was still present along the specimen edge. As a result, SAED patterns were more affected by distortions and shifts. This effect was most prominent at lower thicknesses and disappeared

somewhat at higher thicknesses. Consequently, diffraction spots were broadened which limited the precision of measurements. Due to the limited precision of the measurements of diffraction spots, the measured distances of the diffraction spot from the center proved to be insufficient for distinguishing the diffraction spots from one another to observe the 120° rotation.

Further investigations of the four interfaces B1-B4 in HRTEM revealed that the boundaries were in fact very sharp interfaces. In Figure 4.28, one can see the four interfaces extending along similar directions from the edge of the specimen. At all interfaces, the edge is located on the right side compared to the location of the HRTEM image. Interfaces B1-B4 exhibit somewhat different characteristics in close proximity to the interface. The contrast difference across the interface is rather uniform for B1 and B3, while B2 shows symmetrical darker contrast on opposite sides and B4 shows a more gradual contrast transition on the top side of the interface. What they all have in common is that they all appear to be atomically sharp interfaces. Despite this, interpretation should be performed with caution as appearance in HRTEM images are highly sensitive to phase contrast as explained in subsection 2.4.5.

Interpreting HRTEM images requires careful consideration of several factors [30]. This is because images are highly sensitive to experimental conditions including specimen preparation, imaging parameters, and instrument stability. HRTEM images are not able to capture the true three-dimensional structure and should therefore not be directly interpreted as structural features may be misrepresented in images, especially when they are not perfectly aligned with the electron beam. In this way, a small change in these parameters can have a large effect on the appearance of the features. An example is Figure 4.27, displaying an HRTEM image captured of an arbitrary area of the KNBO sample. At certain locations the structural features appear as the characteristic KNBO triplets of Nb atoms. However, by following the lines of atoms along different directions in the image one can see the effect of the phase contrast in HRTEM emerging. Moving along two different directions, such as is highlighted in Figure 4.27, shows how the phase contrast varies differently across different directions in the image. In the central part of the image, the Nb triplets are visible, but if you go the two different directions highlighted, opposite effects occur where atoms can appear as dark or bright dots. As the thickness increases towards the left side of the image, having the edge on the right side of the acquisition location, this variation of appearances could well be caused solely by thickness effect. However, it points out the effect of phase contrast and the importance to differentiate between genuine structural information and misrepresented features, as described in subsection 2.4.5. Furthermore, HRTEM is a high dose technique and in this initial study prior to the corrected ARM, the structure at the features of interest should not be damaged. Therefore, HRTEM imaging was not further pushed.

To avoid the effect of phase contrast, HAADF-STEM was employed as it is a more independent technique with improved spatial resolution that could validate the inconclusive observations from HRTEM as it is generally not affected by phase contrast for higher collection angles. Consequently, HAADF-STEM can provide directly interpretable images with atomic resolution, allowing for characterization of the lattice structure. As demonstrated here, lattice imaging HAADF STEM does not require $C_s$ correction, although the latter give a superior resolution (0.6

Å compared to ≈ 2 Å). In addition, by going to lower scattering angles, dechanneling effects can reveal the localized strain variations near the boundaries [74], being another inconclusive observation in HRTEM alone. Thus, HAADF-STEM enables a more comprehensive characterization of the interface with better spatial resolution, as well as detection of defects or strain fields. And applying dose point by point, giving the material a chance to dissipate the energy, reduces the risk for damage.

Figure 4.29 shows overview images of all boundaries B1-B4 with the HAADF-STEM technique. Despite being an overview image, the interfaces can be observed to be sharp, extending several micrometers into the material. This shows that the domain walls can be detected as interfaces that light up in an otherwise uniform environment, making it a highly suitable method for localization of domain walls. Again, no contrast difference on opposite sides of the interface with the exception of B1 which was determined to be a crack. Furthermore, displacing the HAADF detector to perform off-centered HAADF was attempted to reveal domain contrast, but did not provide any enhanced contrast difference on opposite sides of the interface due to different polarization directions.

An attempt was made by utilizing HAADF-STEM at low magnification to locate additional domain walls along the edge of the specimen in the region between area A and area B in Figure 4.20. Unfortunately, contamination was observed in an alternating matter, covering large parts of the specimen edge in this region. No signs of additional domain walls were located, despite the edge intersecting with an interesting area along the edge that could potentially have contained charged domain walls. As was previously reported, uncharged twinning domains should be visible using the HAADF-STEM technique [52]. From PLM in Figure 2.16, there should be an abundance of uncharged twinning domains located in the region next to the charged domains. Neither of these twinning domains have been observed where they were expected. For this reason, the silica contamination is believed to overshadow these structural features.

Silica particles are believed to only cover one side of the specimen originating from the second side polishing step. Depending on which side of the specimen the particles are resting on during TEM inspection might be decisive for the detection of the domains. If the particles are resting on top of the specimen, which was the case for the experimental setup, the incident electrons are then disturbed by the amorphous silica particles affecting the channeling, causing them to scatter randomly before hitting the crystalline substrate. Oppositely, if the particles were located on the opposite side, then the incident electrons would first interact with the crystalline specimen, causing the electrons to be scattered to specific directions before interacting with the amorphous particles improving the STEM resolution compared to the current case. This could potentially still reveal charged or uncharged twinning domains. Therefore, further work could be to investigate the remaining area of the specimen with opposite orientation.

Investigation of interfaces B1-B4 with HR HAADF-STEM, shown in Figure 4.30, revealed characteristics that the interfaces are indeed atomically sharp. With this uncorrected TEM/STEM, the triplets of Nb columns (the highest Z) can be identified. The instability during scanning distorts the picture, but the general structure can be deduced. B2-B4 appears to have similar appearance in terms of contrast differences across, while B1 appears to be a gap rather than an

interface. No signal is generated from the gap, where it has a position dependent orientation along the gap. Based on this, B2-B4 all exhibit similar characteristics and are believed to be interfaces, while B1 is believed to be a crack. As the 2100F is a non-aberration-corrected TEM, it has a limited spatial resolution. For this reason, the aberration-corrected ARM microscope was employed to achieve a higher spatial resolution to investigate what happens at the interface. This microscope is designed to achieve a higher spatial resolution (0.6 Å demonstrated), with an improved signal-to-noise ratio, utilizing an increased electron dose. The improved signal-to-noise ratio is clearly shown by comparing the FFTs between the HAADF STEM images in for the different instruments.

### 5.2.3 Aberration Corrected HAADF STEM of Boundaries

The results presented in 4.2.3 proves that both the site-specific specimen preparation and that the initial characterization was performed successfully. Many of the same conclusions are drawn in the ARM compared to the findings in the 2100F, however the improved spatial resolution provides additional data that opens for interpretation of the atomic structure of the charged twinning domain walls. The successful characterization of each interface with atomic resolution also highlights the quality of the specimen as it is possible to navigate from the edge to increasing thickness without having to adjust the tilts to stay on axis. Furthermore, the specimen was relatively stable under the electron beam at high magnifications during lattice imaging. This allowed for characterization of the charged H-H with atomic resolution without causing domain motion or beam damage to the specimen, although strictly speaking it is a twin boundary rather than a mobile ferroelectric boundary.

In Figure 4.31 characteristics such as mistilt, difference in defocus, and bending effects were observed on the right side of the interface. These are convincing characteristics of a crack. Therefore, B1 was determined to be a crack and was not further analysed. However, there is a possibility that these characteristics are caused by a crack that has propagated along an interface. Having the same direction and seemingly atomically sharp at higher thicknesses in HRTEM, shown in Figure 4.28 (a), it might be a domain wall or a tendency for cleaving along 230 planes, what also are planes of domain walls. Even if this was the case, investigation of this interface would require analysis at increased thickness, which is unsuitable for techniques such as HAADF STEM. Considering that all interfaces are assumed to be H-H domain walls, further analysis of B1 was left out to focus on the remaining three interfaces.

The reasoning behind the assumption that the remaining interfaces B2-B4 are charged H-H domain walls and that the atomic structure of T-T configurations are structurally indistinguishable. This H-H distinct atomic configuration, where T-T are not requiring atomic reconfiguration has been suggested by initial density functional theory (DFT) by collaborators in the KNBO project of Dennis Meier (unpublished). Similarly to the visibility in EFM, it is believed that only the H-H configurations are visible using the HAADF STEM technique. HAADF STEM is a technique that is sensitive to atomic positions, but does not show the polarization direction. In some cases the DW can be inverted as there is a clear atomic displacement difference in the two domains, as for hexagonal man-

ganites (R-$MnO_3$, R = Sc, Y, In, Dy–Lu) [75]. Off-centered HAADF-STEM was attempted but did not reveal any contrast differences between expected domains. Therefore, the structurally indistinguishable T-T configurations are not revealed by the techniques employed in this thesis, alternative techniques will be addressed in section 6.2. Based on the SPM measurements in Figure 4.18, the assumed order and positions of H-H domain walls and T-T domain walls along the specimen edge is illustrated in Figure 5.2. Both interfaces are visible using the PFM technique. Similarly, there could be techniques to observe both type of interfaces or either one. Further work therefore includes to find domain contrast using an imaging approach to see the direction of spontaneous polarization.

Initially the crystallographic orientation was decided from the tilt series by comparing the experimental data with simulations. All SAED patterns are observed to fit relatively well with corresponding simulations, including satellite spots going parallel to the more intense spots. This crystallographic orientation was captured from area A, not seen to contain charged DWs. Upon rotating and aligning the atomic resolution ARM data with conventional TEM BF images, as illustrated in Figure 5.1, the orientation is observed to closely match the polarization direction from PFM measurements in Figure 4.18 being approximately 60° relative to the interface. The *a'*-direction on the bottom side can be seen to go parallel to the central atom of Nb triplets towards the domain wall, being rotated by 120° upon crossing the H-H domain wall. This corresponds to the *a"*-direction, which extends until it intersects with the structurally indistinguishable T-T configuration, where it again is rotated by 120°. In this way, the orientation of the neighboring twin domain is also known from the properties of the twinning domains.

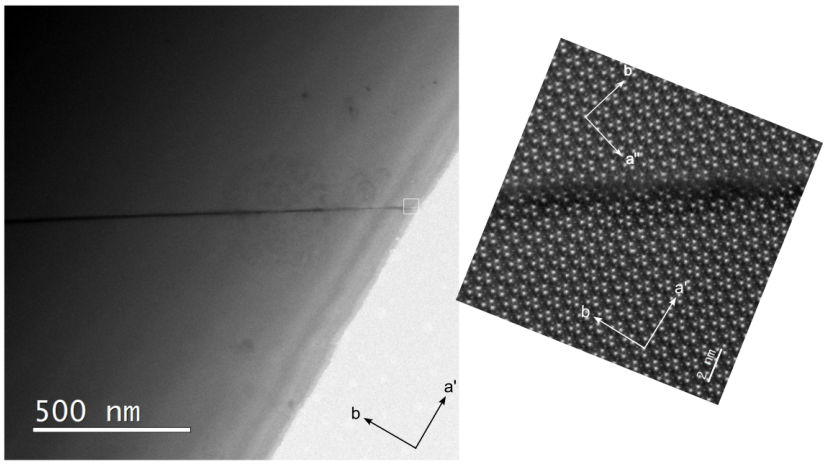


**Figure 5.1:** BF overview image of B2 with an aligned HR HAADF STEM image. Crystallographic orientation is found from the tilt series, located downwards from the crack to give *a'*. Polarization directions *a'* and *a"* are seen to align with the Nb triplets within each twinning domain.

One possibility to prove the existence of a structurally indistinguishable T-T configuration a corresponding tilt series along the $g_{2\bar{3}0}$ direction should be performed within the charged twinning domain. By performing this and comparing it to a general tilt series outside the charged twinning domain, the difference in orientation could be distinguishable by looking at the intensity profile of the

diffraction spots, but might require better detectors than the CCD used in the present work, i.e. direct electron detectors.

Another possible method to verify the presence of the charged H-H and T-T configuration would be to perform additional PFM and EFM scans on the specimen wedge. This has proven to be success full in mapping out the domain structure, without harming the specimen [50]. Oppositely, specimen damage has occurred during such investigation [52]. Performing such analysis with PFM along area B could reveal the amount domain walls along the edge. However, as the directions of the interfaces relative to the edge and their position matches closely with PLM images, it is quite certain that the interfaces are in fact H-H configurations. Therefore, this should not be performed unless necessary as it offers an additional risk to the specimen. This would prohibit all further work suggested in this thesis, as the site-specific specimen preparation is a challenging procedure.

Inspecting the atomically resolvable interfaces in Figure 4.32, there are several similarities between interfaces B2-B4 as well as differences distinguishing them in terms of structural configurations and contrast distributions. The interfaces all show that the span of the interface at some point is across less than a single unit cell, being across a triplet with two additional Nb atom columns situated within the interface. The positions of these additional atoms have been observed on both sides and there has been observed shifts in the $b$-direction across the interface in the line along the $a$'-direction. The atomic configuration within the interface are causing structural distortions in the adjacent triplets, being the most probable cause of the shifts across the interface in Figure 4.33. Ideally it would be possibly to deduce how the crystal on opposite sides are related to each other and to the phase in between using a description of fractional lattice parameters and directions (e.g. $\frac{c}{3}$[UVW]). From the 2D projections in HAADF STEM (with a limited spatial resolution of $\approx 0.8$) there are at least three possible ways to describe how the lattice between the three segments shifts and rotates (see Figure 4.33). Therefore, we describe the atomic structure of the H-H boundary in terms of repeating sub unit cells, the Nb atom columns (shown in Figure 4.32 are clearly visible in HAADF STEM lattice imaging and their common spacing in KNBO in the [001]-projection. Across the twin relation, rotated by 120°, there is a band going along the $2\bar{3}0$ direction with a triplet plus additional Nb columns, with widths of approximately 9-10 Å. In addition, pockets can be seen in an alternating matter along B3. This phenomenon can possibly be caused by instabilities in the interface, causing the formation of these pockets to further stabilize the interface. There are only limited data on the occurrence of such behavior as only three interfaces have been observed within this thesis. Thus, there is a lack of statistics, which opens for many possible interpretations and speculations to be made about the structural configuration of the interface. This could be further elaborated on by complementary simulations of interfaces, e.g. by DFT simulations, a widely applied method for simulation of the local atomic and electronic structure [76]. However, interpretation of the atomic arrangement in structural configuration of the charged H-H domain walls is not a priority for this thesis and is suggested for further work.

Variations in shape have been observed between boundaries B2-B4 having two straight interfaces and one non-straight interface, illustrated in Figure 5.3 (a-c). For all interfaces the interface was observed to be set at a different focus compared

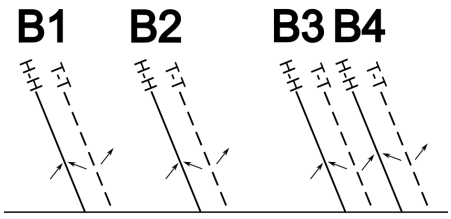


**Figure 5.2:** Schematic showing the four domain walls B1-B4 believed to be H-H domain walls together with their corresponding T-T domain walls. Arrows indicate the spontaneous polarization direction within each twinning domain.

to the different sides of the interface. Opposite sides remained in focus for B2 and B3, while for interface B4 only one of the sides of the interface can be seen to be in focus, where the difference in defocus was indicated as 6 nm. This is a relatively large and unphysical difference in focus, corresponding to several unit cells in difference. However, it is believed that the defocus is not accurate as the focus steps in STEM for this instrument was never calibrated. There is undoubtedly a height difference causing the different regions to fall outside the depth of field. For all the different boundaries, the interface was at a different focus compared to either sides. One plausible explanation is that the differences in defocus are caused shifts in the *c*-direction of the crystal structure, as illustrated in Figure 5.3 (d-f). There are different possibilities of how large these shifts are and how they appear across the interface. Observing the difference in defocus in Figure 4.32 (d-f), the shifts in the unit cells at the interface are homogeneous for B2 and B3, while a step-wise shift could be a reason for the the behavior seen across the B4 interface in as illustrated in Figure 5.3 (d-f), with all levels being set at different defocus. This is better illustrated for B3 in Figure 5.4, where the interface is in focus, while both of the opposite sides fall outside the depth of field, like illustrated in Figure 5.3 (e). Therefore, one can say with quite certainty that there is a height difference at the interface, most likely caused by a shift in the *c*-direction.

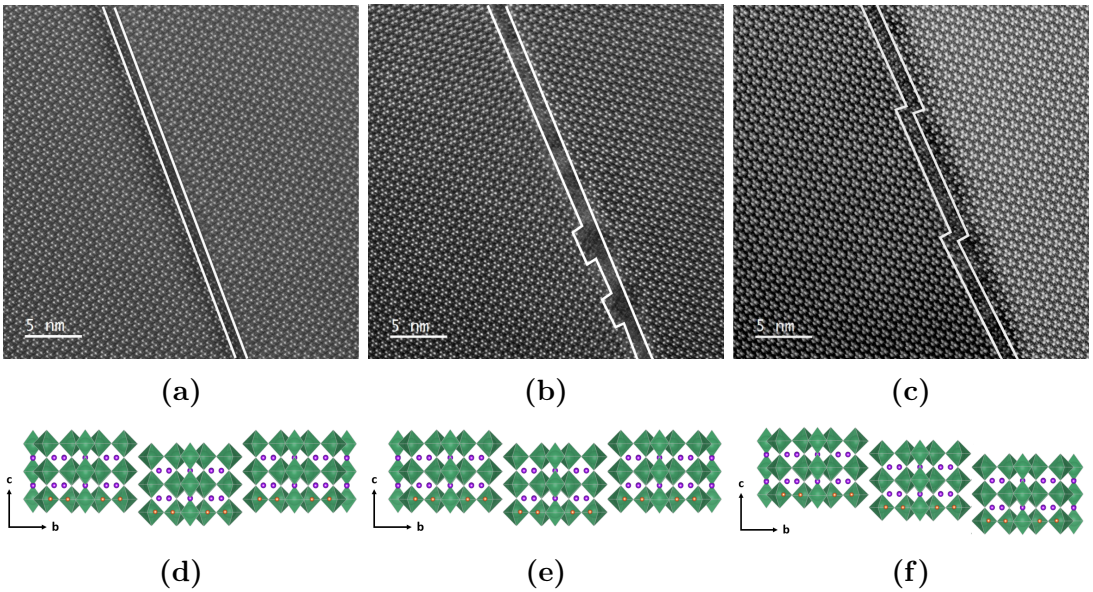


**Figure 5.3:** HAADF STEM image (a-c) of interfaces B2-B4 with lines marking the interface and (d-f) schematic of how unit cells are displaced in the *c*-direction of the corresponding interfaces, with K atoms, Nb octahedras, and B atoms. Note that (d-f) are simplifications ignoring atoms at the boundary of adjacent unit cells. This is only a simplification to illustrate the shift in the c-axis

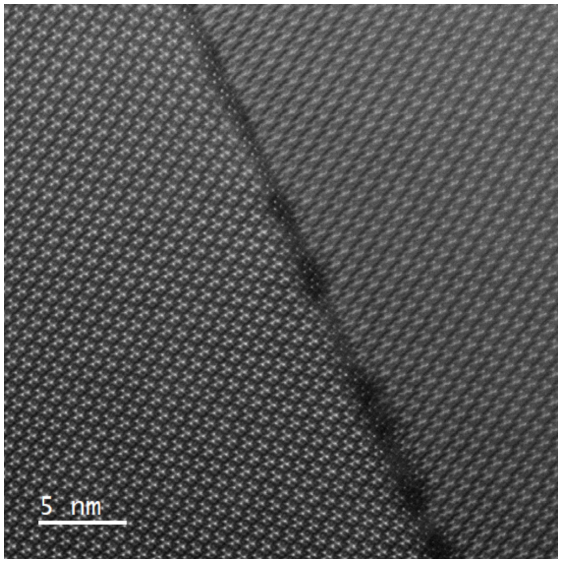


**Figure 5.4:** HAADF STEM image with the interface in focus while the opposite sides of the interface fall outside the depth of field.

The different behavior in interface B4, shifts in the unit cell and steps along the interface, is believed to originate from the structural configuration of the twinning domain. In Figure 4.18 there are thick and parallel walls and needles that terminate at the endpoints. As B4 shows a non-straight interface, the steps can originate from such endpoints where the twinning domains converge in on each other. Thus, the needle could be a result of the twinning domain being close to

the start point or the end point of the domain, where it experiences convergence or divergence. This causes the needle to broaden or narrow, resulting in the needle not being exactly directed along a crystallographic direction over the entire length. As the direction of the steps is towards B3, these two interfaces could be related as they are only 6.5 $\mu$m apart in distance. Although B3 is believed to be a H-H, there is also the opportunity that the T-T is structurally distinguishable as it exhibit a different atomic configuration with the additional atoms situated on the left side of the interface. This difference in behavior could thus indicate the presence of both domain walls. However, if this was the case, then interface B2 should be accompanied by a correlated domain wall, which has not been observed between B2 and B1. B1 is situated at a distance of approximately 30 $\mu$m apart from B2, which should be visible both in PLM and measured with PFM. Therefore, it is still believed that all domain walls are H-H configurations.

## 5.3 TEM Comparison of KMWPO and KNBO

In this study, two multiferroic materials have been characterized using TEM techniques, where previously non or nearly no TEM data has been published on them. Both materials appear to exhibit domain structures, likely derived from twinning domains upon transitioning from the higher temperature phases. However, the aims of the characterization and the areas of interest of the different materials are fundamentally different. KNBO have previously been somewhat studied using TEM, with domain inspection of uncharged twinning domains [50, 52]. The primary objective of the analysis of KNBO was to perform site-specific specimen preparation to characterize the H-H configuration of the charged twinning domains, being a highly specific task related to the understanding of the material. On the other hand, KMWPO has no previous TEM characterization. Therefore, the current study represents the first attempt to make a general characterization of the KMWPO using correlated microscopy and TEM. Consequently, the KMWPO characterization is more general and exploratory, seeking to provide an introduction to the material and to analyse the material's domain structure.

Both materials are relatively exotic in the sense that they are not well-studied yet, despite seen as potentially interesting in the field of ferroelectric DWs. All materials exhibiting twinning domains are highly interesting within the field of charged domain wall engineering and are investigated for their intrinsic properties, as they contain twinning domains in the room temperature phase. These properties make them highly interesting for applications within devices, prompting for investigations to correlate the material properties to the crystal structure. Characterization of the materials gives insight to the material properties and can give indications on the suitability of each material for applications within devices.

Large and high quality tripod specimens were prepared for each of the materials in a combination with correlated microscopy, showing that the specimen preparation approach is solid. KMWPO revealed interesting optical properties in PLM with the [110] in-plane, but was prepared having [110] out-of-plane because of the crystal dimensions limiting the possibility of preparing another orientation. Observing the [110] oriented KMWPO in PLM revealed weak indications of birefringence, resulting in a general specimen preparation. Compared to KMWPO,

the KNBO specimen was prepared with a highly site-specific specimen preparation method. Both PFM and PLM were actively used during specimen preparation to ensure the presence of charged twinning domains along the edge of the specimen. Both materials was prepared successfully with the tripod polishing technique, despite exhibiting different materials properties. The wedges produced was high quality specimens displaying electron transparency along a millimeter sized edge. This mechanical specimen preparation routine is thus a highly capable method for production of TEM specimen, giving large areas of high quality for TEM characterization.

Each of the materials were characterized using several different imaging techniques with TEM. These techniques revealed interesting features that gives insight into the materials intrinsic properties. Within each material, different observations were made on the material properties. KNBO, exhibit twinning domains that is possible to locate with PLM localized within certain regions and are observed to be highly localized within the specimen, being accumulated in certain regions. The twinning domains are visible with certain TEM techniques and rarely occur along the specimen edge. The twinning domains follow closely to a crystallographic direction and generally appears to have similar behavior at a larger scale. In comparison, features are seen to alternate frequently in KMWPO covering the majority of the specimen edge. These structural features are not observable in PLM and extend over a short distances compared to the twinning domains of KNBO. Structural features observed within KMWPO exhibit less regular appearance, showing a larger variance in appearance, directions, and occurrence.

In general the HAADF achieves a better contrast compared to that of BFTEM. For each material, the contrast became more apparent compared to its surroundings when switching to the STEM mode. Because of its directly interpretable Z-contrast imaging and strong contrast due to enhanced channeling effects when exactly aligned with the zone axis, the mode maps out the strain fields and defects within localized regions. This causes enhanced scattering regions to light up, while having a thickness sensitivity that does not affect the incoherent nature of the image [30].

The materials differ considerably in terms of their stability under the incident electron beam. While KNBO shows high stability under the electron beam up to high magnifications, KMWPO displayed increasing beam damage upon exposure with high dosage techniques, such as DF and lattice imaging techniques. In the aftermath of such techniques, the KMWPO specimen experienced a structural amorphization of large areas, affecting the structural features. This greatly complicated further analyses of the structural features, limiting the characterization of KMWPO. KNBO did not exhibit similar behavior as KMWPO, but also this material displayed some degree of beam damage. Lattice imaging is possible for both materials, but the threshold dosage should be considered under high resolution techniques. The techniques work on both materials, but depends if they can give useful results. Exposure of KNBO with HR HAADF STEM during optimization of imaging parameters at higher magnification caused a region along the charged H-H interface to generate reduced signals, showing indications of beam damage. A similar resolution for KMWPO is most likely not possible to achieve without harming the specimen.

In conclusion, there are many differences distinguishing the materials. Both

materials exhibit interesting intrinsic properties that are possible to characterize using TEM. However, there are some details to consider for further characterization of the structural features presented for each material. KMWPO started from scratch with a general direction, while KNBO being better known had a highly specific task. Domain imaging reveal many interesting features and more work is needed for a complete characterization of both materials. Therefore, careful planning of the experimental setup should be considered for further characterization. This is necessary to correlate the material properties to their respective crystal structures and gain an understanding of the material for potential applications within charged domain wall engineering.

CHAPTER

# SIX

# FURTHER WORK

## 6.1 KMWPO

The work here, as far as the author could verify, is the first TEM study of triclinic KMWPO. A specimen preparation routine, limitations due to beam damage, and initial TEM results have been obtained. Many intriguing features were reported for the [110] oriented KMWPO specimen in the TEM characterization and SPM measurements. While it might be interesting to obtain a complete characterization of these features, further work in this thesis suggests to study KMWPO having [110] in-plane. The reasoning for this is that [110] is the optically active axis, revealing optical birefringence that could indicate the presence of interesting properties such as twinning axes remaining from the cooling of higher symmetry states, shown in Figure 4.3. These interesting sightings are in agreement with Peuchert, whom reported that KMWPO exhibits a complicated twinning structures [39] in the given orientation. Therefore, having the [110] in-plane is believed to be the most interesting orientation of the material that should be investigated in further detailed TEM studies. Preparation of a [110] in-plane specimen was attempted for this thesis, but the given (110) crystal was only 300 $\mu$m thick. Preparing a wedge polished specimen with [110] in-plane from the original crystal, was inefficient as it uses much material and the final steps of the specimen preparation failed. A larger thickness of the crystal is beneficial for specimen handling.

From the presented results (e.g. Figure 4.16) it is clear that beam damage can be a showstopper in TEM and possibly in STEM. When increasing magnification, the dose (electrons/Å$^2$) increases. Before attempting to perform further analysis at high spatial resolution of the structural features present in the material, it is necessary to estimate the threshold dosage that the material can handle without experiencing detrimental effects to the structure. The imaging conditions discussed in subsection 5.1.2 can give a rough estimate of what the critical dose for the material is. Having critical dose as design criteria for high resolution imaging and spectroscopy work is essential [77]. An attempt was made at estimating the critical dosage, using SmartAlign [70]. This involved repeatedly exposing an area at low dose, allowing to remove scan noise and drift, therefore the dwell time and with that the dose at one point can be reduced. With swift scans combined with scan rotations the frame from which beam damage appears can be decided to give an estimate on the critical dose. The attempt proved to be inconclusive in terms

of determining when beam damage was introduced to the specimen. Therefore, a more systematic dose test at constant thickness is suggested for further work as it provides a more accurate estimate of the threshold limit. This could involve controlling the exposure times of a converged beam onto a selected position of an area of known thickness to systematically determine the dosage at which the material becomes amorphous. In doing so, the threshold limit can be identified and can motivate for the employment of more advanced reduced dosage techniques. A similar approach, determining the critical dose for tripod wedges using SmartAlign to obtain atomic resolution has previously been achieved for $\alpha$-quartz which is very beam sensitive (more than KMWPO) [78].

Further analysis of structural features using reduced dose techniques are accompanied by a reduction signal. To compensate for this, more sensitive detectors, e.g. ultrafast or direct electron detectors, should be utilized to improve the signal-to-noise ratio, opening for more efficient imaging with fewer electrons per image. The proposal therefore includes careful planning of the experimental setup to avoid surpassing the critical dose by using advanced reduced dose techniques to acquire structural information. More specifically, 4D-STEM techniques [79] combined with reduced electron doses and modern efficient direct electron detectors could provide interesting data on the material which would require post processing data analysis. This could give interesting information with sufficient resolution to investigate structural features and their interfaces without damaging the specimen. Experimental data should be combined with simulations to provide a theoretical reference that can be compared to the experimental data to give a comprehensive characterization.

To conclude on the alternating contrast differences observed for structural features, a proposition is to perform dynamical simulations of CBED patterns to determine the possibility to observe domain contrast for the material. CBED is a powerful technique to determine the crystal structure, including the polarization direction of the material. The local intensity variation could thus provide indications of the polarization direction to explain the observations made in the DF series.

## 6.2 KNBO

Some initial TEM studies were done prior to this study, but the preparation was further refined to have specific charged H-H in the electron transparent area, with a quality good enough for detailed structural analysis through HAADF STEM lattice imaging. Lattice imaging of boundaries B2-B4 revealed differences in astigmatism when the twins and extended twin boundaries are situated at different heights. These differences in astigmatism between each domain caused the astigmatism by the probe to vary slightly between neighboring domains, leading to differences in blurring, contrasts, and distortions in STEM images. The presence of astigmatism can also be influenced by other factors, such as instrumental conditions, lens aberrations, and the specimen. Therefore, it is suggested to perform accurate defocus step calibration of the instrument and quantify the fractional shift in $c$-direction. One way would have, in analog to 6.1, to prepare the $c$-direction in-plane. This is a challenge, as identified from 2D PFM/EFM and density is

low. Investigating this can provide valuable information on the crystallographic differences or structural properties of twinning domains, and can determine if the astigmatism is attributed to variations in crystal orientation or lattice strain.

Image processing techniques would be interesting to employ to investigate the rotations between the twinning domains, being 120° relative to each other. This can either be performed by more accurate electron diffraction analysis as CBED + simulations could be used to verify the relative rotation of adjacent twinning domains or by determination of potential center of mass shifts between reference points in the adjacent twinning domains. The center of mass can shift together with the polarization direction, which can be detected with higher sensitivity detectors than was available in this thesis. This would provide conclusive evidence on the differences in crystal structures on opposite sides of the interface.

Further work also includes to find domain contrast using an imaging approach to see the direction of spontaneous polarization. This would reveal the presence of corresponding T-T domain walls. In the SPM measurements, there were configurations such as PFM which see both interfaces, and EFM which revealed the charged domain wall. Similarly, there could exist imaging approaches that reveals either one or both of the domain walls.

The presence of H-H and T-T domain walls could be proved by performing another tilt series within and outside the charged twinning domain along similar direction. By investigating variations in intensity along the different directions, one could give indications on the polarization directions within the charged twinning domain and compare it to the one captured outside, which has a known crystallographic direction. This could be performed at opposite sides of the H-H domain walls to show differences in intensity.

It would be interesting to investigate where the charge originates from in the charged twinning domain wall. Therefore, EELS is suggested for further work to detect potential migration of charged defects or redistribution of charge carriers. If the charged H-H twin boundary is positively charged, the most likely candidate would be the single Nb column present at the interface. Nb loss edges (N, M, and L) have distinct different shapes depending on valency [80]. As electrons passes through a specimen in EELS, it interacts differently with each elements and electronic states in the material, resulting in characteristic energy losses. The Nb atoms are known to be able to change valency and are thus the focus of interest for the EELS spectra. These energy losses can be seen as characteristic fingerprints for Nb oxides. Variations of the fine structure can be seen as shifts in the high loss peaks of Nb, to see the electronic structure of the material [80]. As each Nb oxide has a characteristic fingerprint in EELS, comparing the energy loss spectra acquired from the interface with one acquired in a different region of the specimen could possibly determine the origin of the charge within the domain wall. Initial attempts shows a need for higher dose for improved signal-to-noise ratio, at 200 kV this caused amorphization. Again better dose management with SmartAlign combined with more efficient detectors can greatly increase the possibility to investigate the electronic structure finger prints.

CHAPTER

# SEVEN

# CONCLUSION

In this work, the multiferroic materials $K_2MgWP_2O_{10}$ (KMWPO) and $K_3Nb_3B_2O_{12}$ (KNBO) have been characterized using a combination of scanning probe microscopy (SPM), conventional transmission electron microscopy (TEM), electron diffraction, HRTEM, HAADF STEM and HR HAADF STEM. The obtained results represent significant advancements in the field as they are the first attempt at characterizing KMWPO and the first study to achieve atomic resolution characterization of the charged twinning domains in KNBO. The work includes optimization of tripod specimen preparation methods for these type of materials, using correlated microscopy for localization of features of interest to map out their domain structure. Correlated microscopy combined polarized light microscopy and piezoresponse force microscopy (PFM) with TEM serve as complementary techniques to successfully analyze ferroelectric properties and the atomic structure. All of the goals set prior to this work have been accomplished; i) determine the viability of site-specific specimen preparation using correlated microscopy, ii) provide an initial characterization of KMWPO with TEM, and iii) determine the structural configuration of the charged H-H twinning domain walls in KNBO.

The method of mechanical tripod polishing proved highly effective in producing electron transparent regions of high quality in millimeter-sized wedges. The specimen preparation routine guided by correlated microscopy techniques enabled the production of tripod wedges of [110] oriented KMWPO and site-specific preparation of low number density charged twinning domains of the [001] oriented KNBO. Potential issues and artifacts have been identified, for example KMWPO is rather soft and remaining silica particles from polishing step can cover areas of interest.

In the general characterization of KMWPO, intriguing alternating contrast features assumed to be charged ferroelectric domains with widths of less than one micron to a few microns were observed along the specimen edge. These features appeared abundantly along large parts of the specimen, mainly extending along the $(1\bar{1}0)$ and (001) directions. The structural features display close resemblance to those measured with PFM and are easily distinguishable using conventional bright-field (BF) technique and high-angle annular dark-field (HAADF) STEM technique. As the specimen is single crystalline and SAED patterns from the structural features are indistinguishable, it is believed that contrast differences is a result of domain structure, i.e. the non-centrosymmetric nature. Based on dark-field TEM, the $1\bar{1}0$ axis is believed to be the polar axis. This study showcases the

possibility of investigating the structural features with lattice resolution, however beam damage is the main challenge. After this first and initial TEM study, further more advanced and detailed studies should be done with consideration to the beam sensitivity of the material. Suggestions for further work: the critical dose should be quantified and after the technique can be optimized given this threshold limit. It would also be interesting to investigate KMWPO with the [110] direction in-plane, where a different and more interesting domain structure is expected using low dose techniques in a combination with more efficient detectors, and data processing.

For KNBO, recent developments using PFM and EFM have revealed the existence of charged twinning domains in the [001] oriented crystal with a low number density. Hence specimen preparation have involved locating and conserving them, with the initial focus of this study being to inspect these unusual interfaces. Four structural anomalies have been observed along the tripod specimen edge, coincident with features in an area studied by PFM in terms of directions and characteristics. Further characterization revealed that three anomalies are sharp interfaces separating twinning domains, being rotated by 120° relative to each other. The structural features, being visible using the conventional BF technique and with the HAADF STEM technique, are all believed to correspond to the H-H configuration, while the T-T boundaries between the H-H are indistinguishable. This thesis presents the first atomic resolution characterization of charged H-H twinning domain walls, exhibiting subtle differences in terms of structural configurations and behavior. Based on lattice imaging using HAADF STEM it is concluded that two straight H-H structures had a width of a single nanometer, corresponding to less than a unit cell and are shifted in the $c$-direction. The $a$-direction (polar axis) oriented approximately 60° relative to the charged domain walls. The interfaces are atomically sharp between domain and domain wall, with additional Nb atoms separating the crystallographic orientations of the neighboring twin domain, causing shifts in the $\pm$ $b$-direction across the interface. The interfaces extend along the crystallographic $2\bar{3}0$ direction, being slightly shifted in the $c$-direction at the interface. The third H-H DW is different as it is not straight, being shifted every 12 nm. Further work suggested includes finding an imaging approach that allows for contrast to identify T-T domain walls and investigation to find the origin of the charge within the interface.

This work demonstrates that exotic and yet not well studied ferroelectric oxides can be characterized by a correlated microscopy study with TEM. Investigation of domain walls requires site-specific specimen preparation that conserves the domain wall structure of high quality. Commonly used ion based thinning methods have here been avoided. The approach based on correlated microscopy has proved as a highly capable method for site-specific specimen preparation for an inspection of charged twinning domain walls in the [001] oriented KNBO and polar ferroelectric domain walls in the [110] oriented KMWPO. The here used approach should be applicable to other oxide ferroelectric materials. However, for high spatial resolution TEM the critical dose to avoid beam damage can be a hard limit. Initial TEM characterization can establish this risk qualitatively. Further work should quantify the critical dose and use alternative advanced techniques that gather the atomic structure information below the limit.

# REFERENCES


[1] A. Gruverman and A. Kholkin. "Nanoscale ferroelectrics: processing, characterization and future trends". In: *Reports on Progress in Physics* 69.8 (July 2005), p. 2443. DOI: 10.1088/0034-4885/69/8/R04. URL: https://dx.doi.org/10.1088/0034-4885/69/8/R04.

[2] J. Mannhart and D. G. Schlom. "Oxide Interfaces. An Opportunity for Electronics". In: *Science* 327.5973 (2010), pp. 1607–1611. DOI: 10.1126/science.1181862. URL: https://www.science.org/doi/abs/10.1126/science.1181862.

[3] P. Sharma, P. Schoenherr, and J. Seidel. "Functional Ferroic Domain Walls for Nanoelectronics". In: *Materials* 12.18 (2019). ISSN: 1996-1944. DOI: 10.3390/ma12182927. URL: https://www.mdpi.com/1996-1944/12/18/2927.

[4] D. D. Viehland and E. K.H. Salje. "Domain boundary-dominated systems: adaptive structures and functional twin boundaries". In: *Advances in Physics* 63.4 (2014), pp. 267–326. DOI: 10.1080/00018732.2014.974304. URL: https://doi.org/10.1080/00018732.2014.974304.

[5] G. Catalan et al. "Domain wall nanoelectronics". In: *Reviews of Modern Physics* 84 (1 Feb. 2012), pp. 119–156. DOI: 10.1103/RevModPhys.84.119. URL: https://link.aps.org/doi/10.1103/RevModPhys.84.119.

[6] J. Seidel. "Domain Walls as Nanoscale Functional Elements". In: *The Journal of Physical Chemistry Letters* 3.19 (2012), pp. 2905–2909. DOI: 10.1021/jz3011223. eprint: https://doi.org/10.1021/jz3011223. URL: https://doi.org/10.1021/jz3011223.

[7] C. Kittel. *Introduction to Solid State Physics*. Wiley, 2004. ISBN: 9780471415268. URL: https://books.google.no/books?id=kym4QgAACAAJ.

[8] G. F. Nataf et al. "Domain-wall engineering and topological defects in ferroelectric and ferroelastic materials". In: *Nature Reviews Physics* 2 (11 Jan. 2020), pp. 634–648. DOI: 10.1038/s42254-020-0235-z. URL: https://doi.org/10.1038/s42254-020-0235-z.

[9] D. Meier and S.M. Selbach. "Ferroelectric domain walls for nanotechnology". In: *Nature Reviews Materials* 7.3 (2022), pp. 157–173. DOI: https://doi.org/10.1038/s41578-021-00375-z. URL: https://www.nature.com/articles/s41578-021-00375-z.

[10] P. Bednyakov et al. "Physics and applications of charged domain walls". In: *npj Computational Materials* 4 (Dec. 2018). DOI: 10.1038/s41524-018-0121-8.

[11] R. K. Vasudevan et al. "Domain wall geometry controls conduction in ferroelectrics". In: *Nano letters* 12.11 (2012), pp. 5524–5531. DOI: 10.1021/nl302382k. URL: https://doi.org/10.1021/nl302382k.

[12] E. K. H. Salje and Z. Huali. "Domain boundary engineering". In: *Phase Transitions* 82.6 (2009), pp. 452–469. DOI: 10.1080/01411590902936138. URL: https://doi.org/10.1080/01411590902936138.

[13] S. Van Aert et al. "Direct Observation of Ferrielectricity at Ferroelastic Domain Boundaries in CaTiO3 by Electron Microscopy". In: *Advanced Materials* 24.4 (2012), pp. 523–527. DOI: https://doi.org/10.1002/adma.201103717. URL: https://onlinelibrary.wiley.com/doi/abs/10.1002/adma.201103717.

[14] P. S. Bednyakov et al. "Formation of charged ferroelectric domain walls with controlled periodicity". In: *Scientific Reports* 5 (2015), p. 15. 15819. DOI: 10.1038/srep15819. URL: http://infoscience.epfl.ch/record/213451.

[15] Y. Qi et al. "Coexistence of ferroelectric vortex domains and charged domain walls in epitaxial $BiFeO_3$ film on (110)O $GdScO_3$ substrate". In: *Journal of Applied Physics* 111.10 (2012), p. 104117. DOI: 10.1063/1.4722253. URL: https://doi.org/10.1063/1.4722253.

[16] G. F. Nataf et al. "Domain-wall engineering and topological defects in ferroelectric and ferroelastic materials". In: *Nature Reviews Physics* 2 (Nov. 2020), pp. 634–648. ISSN: 2522-5820. DOI: 10.1038/s42254-020-0235-z.

[17] P. Shan et al. "Lead-free polar borate crystal $K_3Nb_3B_2O_{12}$: a novel antiferroelectric structure type". In: *Journal of Materials Chemistry C* 8 (20 2020), pp. 6654–6658. DOI: 10.1039/D0TC01383H. URL: http://dx.doi.org/10.1039/D0TC01383H.

[18] P. Shan et al. "Electro-optic modulation in a non-centrosymmetric antiferroelectric crystal". In: *Journal of Materials Chemistry C* 9 (30 2021), pp. 9431–9435. DOI: 10.1039/D1TC02309H. URL: http://dx.doi.org/10.1039/D1TC02309H.

[19] E. K. H. Salje. "Multiferroic Domain Boundaries as Active Memory Devices: Trajectories Towards Domain Boundary Engineering". In: *ChemPhysChem* 11.5 (2010), pp. 940–950. DOI: https://doi.org/10.1002/cphc.200900943. URL: https://chemistry-europe.onlinelibrary.wiley.com/doi/abs/10.1002/cphc.200900943.

[20] D. Lee et al. "Mixed Bloch-Néel-Ising character of 180° ferroelectric domain walls". In: *Physical Review B* 80 (6 Aug. 2009), p. 060102. DOI: 10.1103/PhysRevB.80.060102. URL: https://link.aps.org/doi/10.1103/PhysRevB.80.060102.

[21] M. Topstad. "TEM Characterization of Ferroelectric $BaMgF_4$. Project thesis, Norwegian University of Science and Technology". unpublished. 2022.

[22] Z. Dauter and M. Jaskolski. "How to read (and understand) Volume A of International Tables for Crystallography: An introduction for nonspecialists". In: *Journal of Applied Crystallography* 43 (Oct. 2010), pp. 1–22. DOI: 10.1107/S0021889810026956.

[23] K. Stadnicka, B. Oleksyn, and K. Sokalski. "International tables for crystallography edited by Th. Hahn". In: *Acta Crystallographica Section B* 42 (Oct. 1986), pp. 240–241. DOI: 10.1107/S0108768186097768.

[24] P. Shi et al. "Symmetry breaking in molecular ferroelectrics". In: *Chemical Society Reviews journal* 45 (14 2016), pp. 3811–3827. DOI: 10.1039/C5CS00308C. URL: http://dx.doi.org/10.1039/C5CS00308C.

[25] G. Catalan et al. "Domain wall nanoelectronics". In: *Review of Modern Physics* 84 (1 2012), pp. 119–156. DOI: 10.1103/RevModPhys.84.119. URL: https://link.aps.org/doi/10.1103/RevModPhys.84.119.

[26] J. van den Brink and D. I. Khomskii. "Multiferroicity due to charge ordering". In: *Journal of Physics: Condensed Matter* 20.43 (Oct. 2008), p. 434217. DOI: 10.1088/0953-8984/20/43/434217. URL: https://dx.doi.org/10.1088/0953-8984/20/43/434217.

[27] L. D. Landau and E. M. Lifshitz. "On the Theory of the Dispersion of Magnetic Permeability in Ferromagnetic Bodies". In: *Perspectives in Theoretical Physics*. Amsterdam: Pergamon, 1992, pp. 51–65. ISBN: 978-0-08-036364-6. DOI: https://doi.org/10.1016/B978-0-08-036364-6.50008-9. URL: https://www.sciencedirect.com/science/article/pii/B9780080363646500089.

[28] C. Kittel. "Theory of the Structure of Ferromagnetic Domains in Films and Small Particles". In: *Physical Review* 70 (11-12 Dec. 1946), pp. 965–971. DOI: 10.1103/PhysRev.70.965. URL: https://link.aps.org/doi/10.1103/PhysRev.70.965.

[29] E. K. H. Salje. "Ferroelastic Materials". In: *Annual Review of Materials Research* 42.1 (2012), pp. 265–283. DOI: 10.1146/annurev-matsci-070511-155022. URL: https://doi.org/10.1146/annurev-matsci-070511-155022.

[30] D. Williams and C. Carter. *Transmission Electron Microscopy: A Textbook for Materials Science*. Vol. III. Springer New York, NY, June 2009. ISBN: 9780387765020. DOI: 10.1007/978-1-4757-2519-3.

[31] R. Erni. *Aberration-corrected imaging in transmission electron microscopy: An introduction*. World Scientific Publishing Company, 2015.

[32] U. Peuchert, L. Bohaty, and J. Schneider. "Ab initio structure solution and rietveld refinement of the high-temperature $K_2MgWO_2(PO_4)_2$ phase (T = 773 K) from X-ray powder diffraction data". In: *JOURNAL OF APPLIED CRYSTALLOGRAPHY* 31.1 (Feb. 1998), pp. 10–15. ISSN: 0021-8898. DOI: 10.1107/S0021889897006389.

[33] M. Maczka et al. "Direct evidence of an order-disorder nature of ferroelectric phase transitions in $K_2MgWO_2(PO_4)_2$". In: *Applied Physics Letters* 90.12 (2007), p. 122903. DOI: 10.1063/1.2713873. URL: https://doi.org/10.1063/1.2713873.

[34] M. Maczka et al. "Temperature-dependent IR and Raman scattering studies of phase transitions in $K_2MgWO_2(PO_4)_2$". In: *Journal of Physics-Condensed Matter* 25.2 (Jan. 2013). ISSN: 0953-8984. DOI: 10.1088/0953-8984/25/2/025901.

[35] M. Maczka et al. "Lattice dynamics and high-pressure Raman scattering studies of ferroelectric $K_2MgWO_2(PO_4)_2$". In: *Physical Review B* 78 (Aug. 2008), p. 064116. DOI: 10.1103/PhysRevB.78.064116. URL: https://link.aps.org/doi/10.1103/PhysRevB.78.064116.

[36] U. Peuchert, L. Bohaty, and J. Schreuer. "The triclinic room-temperature modification of $K_2MgWO_2(PO_4)_2$". In: *Acta Crystallographica Section B* 53.1 (Jan. 1997), pp. 11–14. ISSN: 0108-2701. DOI: 10.1107/S0108270196011389.

[37] K. Momma and F. Izumi. "*VESTA3* for three-dimensional visualization of crystal, volumetric and morphology data". In: *Journal of Applied Crystallography* 44.6 (Dec. 2011), pp. 1272–1276. DOI: 10.1107/S0021889811038970. URL: https://doi.org/10.1107/S0021889811038970.

[38] M. Mączka et al. "Heat capacity and high-resolution Brillouin scattering studies of phase transitions in $K_2MgWO_2(PO_4)_2$: Observation of the coupled soft optic and acoustic mode". In: *Physical Review B* 75 (21 June 2007), p. 214105. DOI: 10.1103/PhysRevB.75.214105. URL: https://link.aps.org/doi/10.1103/PhysRevB.75.214105.

[39] U. Peuchert. "Kristallphysikalische und strukturelle Untersuchungen von Phasenumwandlungen in den Orthophosphaten vom Typ $K_2Me^{II}WO_2(PO_4)_2$ mit $Me^{II}$ = Mg, Ni, Co, Fe, Mn, Cd". unpublished. PhD thesis. University of Cologne, 1995.

[40] J. Choisnet et al. "Nouvelles structures à tunnels de section pentagonale $K_3Nb_3B_2O_{12}$ et $K_3Ta_3B_2O_{12}$". In: *Acta Crystallographica Section B* 33.6 (June 1977), pp. 1841–1845. DOI: 10.1107/S056774087700716X. URL: https://doi.org/10.1107/S056774087700716X.

[41] A. A. Kaminskii et al. "Room-temperature high-order Stokes and anti-Stokes generation in orthorhombic ferroelectric-ferroelastic $K_3Nb_3O_6(BO_3)_2$ crystal". In: *Physica Status Solidi* 201.9 (2004), pp. 2154–2169. DOI: https://doi.org/10.1002/pssa.200406834. URL: https://onlinelibrary.wiley.com/doi/abs/10.1002/pssa.200406834.

[42] M. Maczka et al. "High-pressure Raman scattering study of ferroelectric $K_3Nb_3O_6(BO_3)_2$". In: *Physical Review B* 82 (1 July 2010), pp. 104–106. DOI: 10.1103/PhysRevB.82.014106. URL: https://link.aps.org/doi/10.1103/PhysRevB.82.014106.

[43] P. Becker, P. Held, and L. Bohaty. "Crystal growth of ferroelectric and ferroelastic $K_3Nb_3O_6(BO_3)_2$ and crystal structure of the room temperature modification". In: *Zeitschrift für Kristallographie – Crystalline Materials* 211 (July 1996), pp. 449–452. DOI: 10.1524/zkri.1996.211.7.449.

[44] P. Becker, L. Bohaty, and J. Schneider. "Crystal structure of the high-temperature $K_3Nb_3O_6BO_3)_2$ phase refined by the Rietveld method". In: *Crystallography Reports* 42 (2 Mar. 1997). DOI: http://dx.doi.org/10.1134/1.170615.

[45] G. A. Rossetti and A. G. Khachaturyan. "Inherent nanoscale structural instabilities near morphotropic boundaries in ferroelectric solid solutions". In: *Applied Physics Letters* 91.7 (2007), p. 072909. DOI: 10.1063/1.2771095. URL: https://doi.org/10.1063/1.2771095.

[46] V. I. Voronkova, E. P. Kharitonova, and V. K. Yanovskii. "Growth, structure, and properties of ferroelectric—ferroelastic— superionic $K_3Nb_3B_2O_{12}$ and $K_{3x}Na_xNb_3B_2O_{12}$ crystals". In: *Crystallography Reports* 45 (5 Sept. 2000), pp. 816–820. DOI: https://doi.org/10.1134/1.1312928. URL: https://link.springer.com/article/10.1134/1.1312928.

[47] M. Mączka, J. Hanuza, and S. Kojima. "High-resolution temperature-dependent Brillouin scattering studies of ferroelectric $K_3Nb_3O_6(BO_3)_2$". In: *Physical Review B* 77 (10 Mar. 2008), pp. 104–116. DOI: 10.1103/PhysRevB.77.104116. URL: https://link.aps.org/doi/10.1103/PhysRevB.77.104116.

[48] E. P. Kharitonova et al. "Polymorphism of ferroelectric, ferroelastic, superionic crystals $K_3Nb_3B_2O_{12}$ and $K_{3-x}Na_xNb_3B_2O_{12}$". In: *INORGANIC MATERIALS* 38.8 (Aug. 2002), pp. 819–824. ISSN: 0020-1685. DOI: 10.1023/A:1019782912439.

[49] E. P. Kharitonova, V. I. Voronkova, and V. K. Yanovskii. "Phase transitions and ferroelectric and superionic properties of $K_3Nb_3B_2O_{12}$-$K_3Nb_3Si_2O_{13}$ single crystals". In: *Inorganic Materials* 39.2 (Feb. 2003), pp. 127–132. ISSN: 0020-1685. DOI: 10.1023/A:1022190411905.

[50] O. Ryggetangen. *Domain imaging of multiferroic $K_3Nb_3B_2O_{12}$ by transmission electron microscopy*. 2021. URL: https://hdl.handle.net/11250/2823454.

[51] M. Linnerud. "Correlated transmission electron microscopy studies for high spatial resolution and lattice defect structure analysis in single crystal $K_3Nb_3B_2O_{12}$ and its domain wall structures". Unpublished. Dec. 2021.

[52] M. Linnerud. *Building a framework for domain characterisation of $K_3Nb_3B_2O_{12}$ by electron diffraction and transmission electron microscopy*. 2022. URL: https://hdl.handle.net/11250/3021961.

[53] P. E. Tomaszewski. "Jan Czochralski—father of the Czochralski method". In: *Journal of Crystal Growth* 236.1 (2002), pp. 1–4. ISSN: 0022-0248. DOI: https://doi.org/10.1016/S0022-0248(01)02195-9. URL: https://www.sciencedirect.com/science/article/pii/S0022024801021959.

[54] K. A. Hunnestad. *Visualizing Ferroelectric Domain Structures in $ErMnO_3$ and $Pb_5Ge_3O_{11}$ by Electron Microscopy*. MSc theisis, Dep. Physics, Norwegian Univeristy of Science and Technology. 2019. URL: http://hdl.handle.net/11250/2625259.

[55] E. Eberg et al. "Comparison of TEM specimen preparation of perovskite thin films by tripod polishing and conventional ion milling". In: *Journal of Electron Microscopy* 57.6 (Sept. 2008), pp. 175–179. ISSN: 0022-0744. DOI: 10.1093/jmicro/dfn018. URL: https://doi.org/10.1093/jmicro/dfn018.

[56] *Multiprep Polishing System - 12"*. Allied High Tech Products inc. 2019. URL: https://www.alliedhightech.com/Equipment/multiprep-polishing-system-12 (visited on 11/18/2022).

[57] Gatan inc. *Gatan inc. DigitalMicrograph Software*. Accessed: 2023-02-23. URL: http://web.archive.org/web/20080207010024/http://www.808multimedia.com/winnt/kernel.html.

[58] C. Schneider, W. Rasband, and K. Eliceiri. "NIH Image to ImageJ: 25 years of image analysis." In: *Nature Methods* 9 (2012), pp. 671–675. DOI: 110.1038/nmeth.2089. URL: https://www.nature.com/articles/nmeth.2089.

[59] Y. Seto and M. Ohtsuka. "*ReciPro*: free and open-source multipurpose crystallographic software integrating a crystal model database and viewer, diffraction and microscopy simulators, and diffraction data analysis tools". In: *Journal of Applied Crystallography* 55.2 (Apr. 2022), pp. 397–410. DOI: 10.1107/S1600576722000139. URL: https://doi.org/10.1107/S1600576722000139.

[60] D. Nečas and P. Klapetek. "Gwyddion: an open-source software for SPM data analysis". In: *Open Physics* 10.1 (2012), pp. 181–188. DOI: doi:10.2478/s11534-011-0096-2. URL: https://doi.org/10.2478/s11534-011-0096-2.

[61] P .M. Voyles, J. L. Grazul, and D. A. Muller. "Imaging individual atoms inside crystals with ADF-STEM". In: *Ultramicroscopy* 96.3 (2003). Proceedings of the International Workshop on Strategies and Advances in Atomic Level Spectroscopy and Analysis, pp. 251–273. ISSN: 0304-3991. DOI: https://doi.org/10.1016/S0304-3991(03)00092-5. URL: https://www.sciencedirect.com/science/article/pii/S0304399103000925.

[62] T. Höche, W. J. Gerlach, and T. Petsch. "Static-charging mitigation and contamination avoidance by selective carbon coating of TEM samples". In: *Ultramicroscopy* 106.11 (2006). Proceedings of the International Workshop on Enhanced Data Generated by Electrons, pp. 981–985. ISSN: 0304-3991. DOI: https://doi.org/10.1016/j.ultramic.2006.05.007. URL: https://www.sciencedirect.com/science/article/pii/S0304399106000957.

[63] L. A. Giannuzzi and F. A. Stevie. "A review of focused ion beam milling techniques for TEM specimen preparation". In: *Micron* 30.3 (1999), pp. 197–204. ISSN: 0968-4328. DOI: https://doi.org/10.1016/S0968-4328(99)00005-0. URL: https://www.sciencedirect.com/science/article/pii/S0968432899000050.

[64] J. L. Hart et al. "Electron-beam-induced ferroelectric domain behavior in the transmission electron microscope: Toward deterministic domain patterning". In: *Physical Review B* 94 (17 Nov. 2016), p. 174104. DOI: 10.1103/PhysRevB.94.174104. URL: https://link.aps.org/doi/10.1103/PhysRevB.94.174104.

[65] Z. Chen et al. "Manipulation of Nanoscale Domain Switching Using an Electron Beam with Omnidirectional Electric Field Distribution". In: *Physical Review Letters* 117 (2 July 2016), p. 027601. DOI: 10.1103/PhysRevLett.117.027601. URL: https://link.aps.org/doi/10.1103/PhysRevLett.117.027601.

[66] E. D. Roede et al. "Contact-free reversible switching of improper ferroelectric domains by electron and ion irradiation". In: *APL Materials* 9.2 (Feb. 2021). ISSN: 2166-532X. DOI: 10.1063/5.0038909. URL: https://doi.org/10.1063/5.0038909.

[67] A. Chuvilin et al. "On the origin of HOLZ lines splitting near interfaces: multislice simulation of CBED patterns". In: *Journal of Electron Microscopy* 54.6 (Jan. 2006), pp. 515–517. ISSN: 0022-0744. DOI: 10.1093/jmicro/dfi069. URL: https://doi.org/10.1093/jmicro/dfi069.

[68] A. I. Kirkland and R. R. Meyer. ""Indirect" High-Resolution Transmission Electron Microscopy: Aberration Measurement and Wavefunction Reconstruction". In: *Microscopy and Microanalysis* 10.4 (2004), pp. 401–413. DOI: 10.1017/S1431927604040437.

[69] S. Parsons. "Introduction to twinning". In: *Acta Crystallographica Section D* 59.11 (Nov. 2003), pp. 1995–2003. DOI: 10.1107/S0907444903017657. URL: https://doi.org/10.1107/S0907444903017657.

[70] L. Jones et al. "Smart Align – a new tool for robust non-rigid registration of scanning microscope data". In: *Advanced Structural and Chemical Imaging* 1 (July 2015). DOI: 10.1186/s40679-015-0008-4.

[71] Q. Chen et al. "Imaging Beam-Sensitive Materials by Electron Microscopy". In: *Advanced Materials* 32.16 (2020), p. 1907619. DOI: 10.1002/adma.201907619. URL: https://onlinelibrary.wiley.com/doi/abs/10.1002/adma.201907619.

[72] J. P. Buban et al. "High-resolution low-dose scanning transmission electron microscopy". In: *Journal of Electron Microscopy* 59.2 (Nov. 2009), pp. 103–112. ISSN: 0022-0744. DOI: 10.1093/jmicro/dfp052. URL: https://doi.org/10.1093/jmicro/dfp052.

[73] E. D. Roede et al. "Contact-free reversible switching of improper ferroelectric domains by electron and ion irradiation". In: *APL Materials* 9.2 (Feb. 2021). ISSN: 2166-532X. DOI: 10.1063/5.0038909. URL: https://doi.org/10.1063/5.0038909.

[74] A. T. J. van Helvoort et al. "Imaging of out-of-plane interfacial strain in epitaxial $PbTiO_3/SrTiO_3$ thin films". In: *Applied Physics Letters* 86.9 (Feb. 2005). ISSN: 0003-6951. DOI: 10.1063/1.1874303. URL: https://doi.org/10.1063/1.1874303.

[75] M. E. Holtz et al. "Topological Defects in Hexagonal Manganites: Inner Structure and Emergent Electrostatics". In: *Nano Letters* 17.10 (2017), pp. 5883–5890. DOI: 10.1021/acs.nanolett.7b01288. URL: https://doi.org/10.1021/acs.nanolett.7b01288.

[76] M. Sepliarsky et al. "Atomic-level simulation of ferroelectricity in oxide materials". In: *Current Opinion in Solid State and Materials Science* 9.3 (2005), pp. 107–113. ISSN: 1359-0286. DOI: https://doi.org/10.1016/j.cossms.2006.05.002. URL: https://www.sciencedirect.com/science/article/pii/S1359028606000416.

[77] S. Wenner et al. "Atomic-resolution chemical mapping of ordered precipitates in Al alloys using energy-dispersive X-ray spectroscopy". In: *Micron* 96 (2017), pp. 103–111. ISSN: 0968-4328. DOI: https://doi.org/10.1016/j.micron.2017.02.007. URL: https://www.sciencedirect.com/science/article/pii/S096843281730001X.

[78] J. Busam et al. "Structural Characterization of Natural Quartz by Scanning TEM". In: *Microscopy and Microanalysis* 24 (Aug. 2018), pp. 2044–2045. DOI: 10.1017/S143192761801070X.

[79] C. Ophus. "Four-Dimensional Scanning Transmission Electron Microscopy (4D-STEM): From Scanning Nanodiffraction to Ptychography and Beyond". In: *Microscopy and Microanalysis* 25.3 (June 2019), pp. 563–582. ISSN: 1431-9276. DOI: 10.1017/S1431927619000497. URL: https://doi.org/10.1017/S1431927619000497.

[80] D. Bach et al. "EELS of Niobium and Stoichiometric Niobium-Oxide Phases—Part I: Plasmon and Near-Edges Fine Structure". In: *Microscopy and Microanalysis* 15.6 (Oct. 2009), pp. 505–523. ISSN: 1431-9276. DOI: 10.1017/S143192760999105X. URL: https://doi.org/10.1017/S143192760999105X.

# APPENDICES

APPENDIX

# A

# TRIPOD POLISHING ROUTINE

The routine used in the specimen preparation of all tripod samples is an adaption from the previous work of the author [21], the work of Hunnestad [54], which is further based on the work of Eberg et al. [55]. Alterations have been made to the process based on the best approach to achieve superior quality samples. The process used a *Allied Multiprep System* polishing system.

1. **Sample preparation**

   - Mount the crystal on a glass slide using wax.
   - Separate into pieces of $1 \times 1 - 2$ mm$^2$ using *Testbourne Model 650 Low Speed Diamond Wheel Saw* with a 3" 150 $\mu m$ diamond wafering blade. Apply sufficient load, $> 200g$ with a sufficiently high rotation speed.
   - Detach the sample from the glass slide using acetone followed by a rinse in ethanol.
   - Calibrate the polisher to assure reliable accuracy.
   - Polish pyrex stub using 15 $\mu m$ followed by 6 $\mu m$ with a 500 g load to have sufficient surface roughness for glue to adhere properly.
   - Clean pyrex using acetone followed by ethanol.
   - Mount specimen on pyrex stub using *Loctite Precision* acetone soluble glue and let the glue cure overnight.

2. **Polishing routine - First facet**

   - Polish the reference using the 15 $\mu m$ DLF with 200 g load at 30 rpm until sample is flat while continuously rinsing with water. Inspect sample in VLM for crack formations.
   - Polish sample using a 6 $\mu m$ DLF using the same conditions until 50 $\mu m$ of material is removed. Inspect sample in VLM for crack formations.
   - Polish sample using a 3 $\mu m$ DLF using the same conditions until 20 $\mu m$ of material is removed. Inspect sample in VLM for crack formations.
   - Polish sample using a 1 $\mu m$ DLF with 50 g load until 10 $\mu m$ of material is removed. For this step, use *Allied Green Lube* applied to the DLF and avoid rinsing with water. Inspect sample in VLM for crack formations.

- Polish sample using a 0.5 $\mu m$ DLF using the same conditions for 30 sec before inspecting the sample in VLM for crack formations.
- Polish sample using a 0.1 $\mu m$ DLF using the same conditions for 30 sec before inspecting the sample in VLM for crack formations.
- Polish sample for 30 sec at a time using a polishing cloth with *Allied 0.02 $\mu m$ Colloidal Silica* solution with 50 g load. After polishing, rinse in DI water and clean sample with *Allied Micro Organic soap* applied using a cotton swab followed by another rinse with DI water. Inspect sample in VLM for crack formation. Repeat process until all deep scratches are removed and specimen looks uniform.
- Detach sample from pyrex using an acetone bath overnight and rinse inside an ethanol beaker for a 5 minutes. Re-attach the sample perpendicular to the edge of the pyrex with the polished side facing the pyrex.

3. **Polishing routine - Second facet**

   - Using a 15 $\mu m$ DLF, polish the sample down to 500 $\mu m$ thickness while rinsing with water with a 200 g load.
   - Introduce a 2° angle to the polishing system and continue polishing with 15 $\mu m$ DLF until the edge reaches a thickness of 250 $\mu m$. Ensure the sample is oriented perpendicular to the polishing direction.
   - Polish sample using a 6 $\mu m$ DLF using the same conditions until the thickness of the edge is 150 $\mu m$. Inspect sample in VLM for crack formations.
   - Polish sample using a 3 $\mu m$ DLF until the thickness of the edge is 60 $\mu m$. Inspect sample in VLM for crack formation.
   - Polish sample for using a 1 $\mu m$ DLF at $<$ 50 g load, using *Allied Green Lube*. Inspect sample frequently in VLM for crack formation.
   - Polish sample using a 0.1 $\mu m$ DLF using the same conditions for 10 sec before inspecting the sample in VLM to observe a shortening of the thin edge inwards into the polishing stub. Inspect for potential crack formations or chipping and reposition the specimen after each polishing step to avoid residues circulating and harming the specimen.
   - Polish sample for 20 sec using a polishing cloth with *Allied 0.02 $\mu m$ Colloidal Silica* solution at $<$ 50 g load. Avoid excessive pressure (more than 0.010 on the micrometer). After polishing, rinse in DI water and clean sample with diluted *Allied Micro Organic soap* applied using a cotton swab followed by another rinse with DI water. Inspect sample in VLM for crack formation or chipping. Repeat process until all deep scratches are removed and thickness fringes are more prominent

4. **Sample mounting to TEM half-grid**.

   - Make the 2 mm $\times$ 0.5 mm TEM slot grid into a TEM half-grid using a scalpel. The intention of this is to make subsequent ion milling easier if further treatment of the specimen is necessary.

- Distribute small drops of *Araldite epoxy adhesive* acetone-resistant two-part glue to the sample using a sharpened toothpick.
- Place the half-grid on top and gently slide it into the correct position to achieve the region of interest at the center. Avoid glue covering the region of interest.
- Let epoxy glue cure overnight.
- Detach sample from pyrex using acetone bath overnight.
- Move sample into a clean acetone bath for another 15 minutes followed by a rinse in ethanol for 5 minutes.

The final tripod sample is extremely brittle so it should only be handled by vacuum tweezers. Apply silver paste to mitigate charging effects by electrically connecting the crystal to the TEM half-grid.

APPENDIX

# B

# FEATURE INVESTIGATION

This appendix contains a similar collection of structural investigation of the KMWPO features, corresponding to the one performed for horizontal features in Figure 4.9, including vertical features and needle-like features.

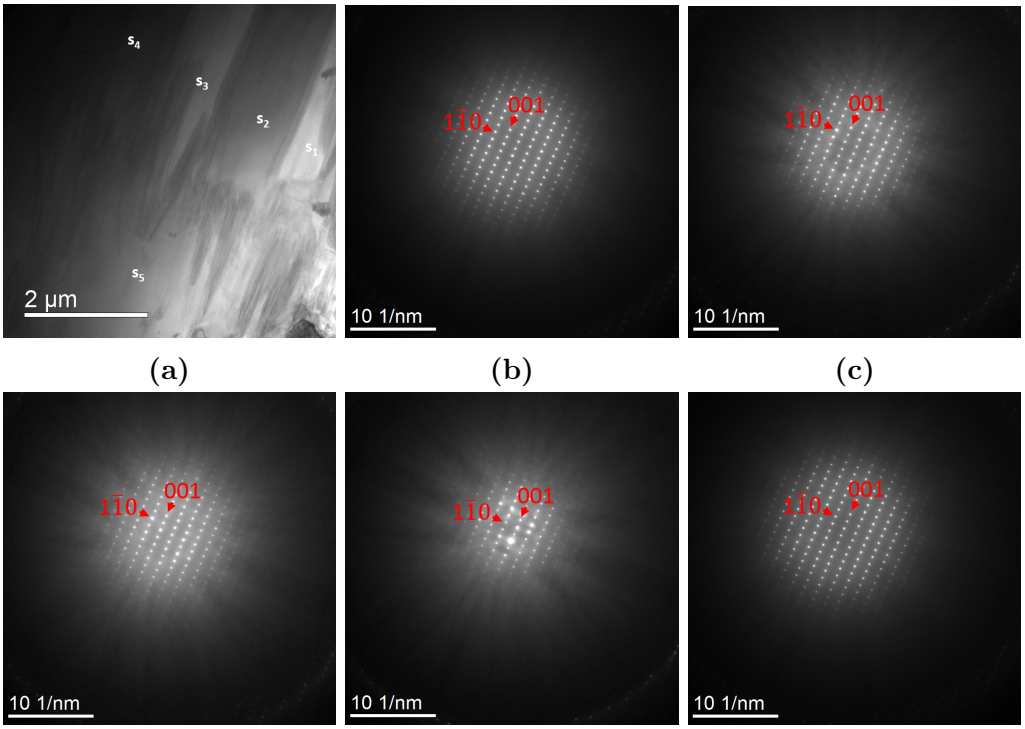


**Figure B.1:** (a) BF overview image of needle-like features displaying differences in contrast in the [110] oriented KMWPO specimen, while (b-f) shows SAED patterns captured from region $s_1$-$s_5$, respectively.

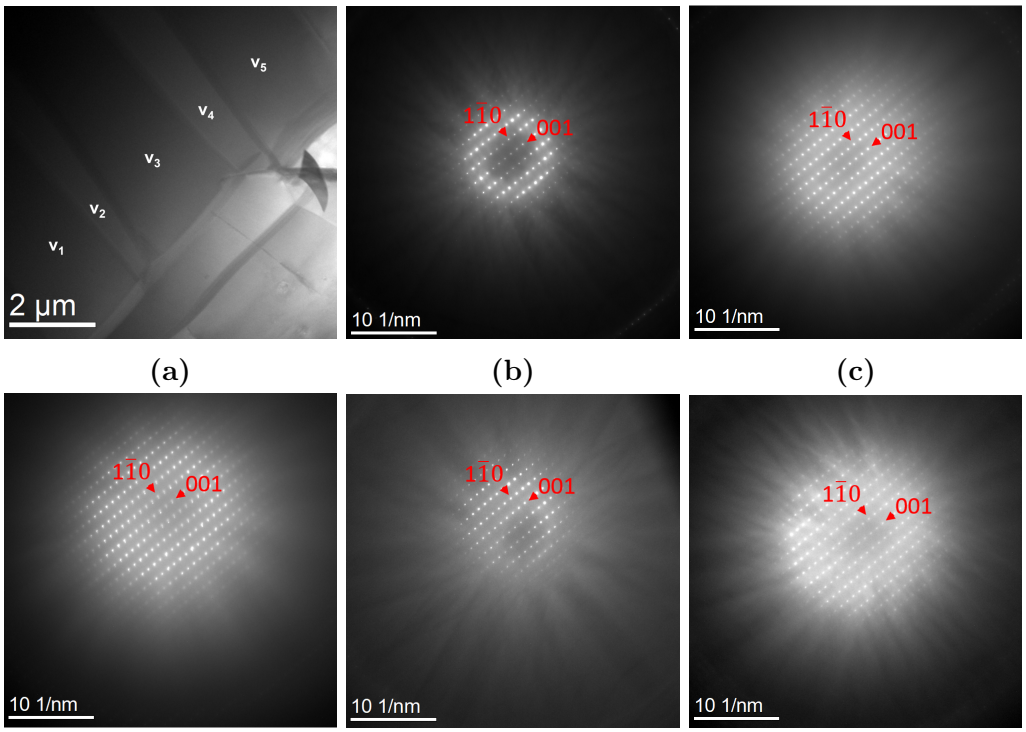


**Figure B.2:** (a) BF overview image of vertical features displaying differences in contrast in the [110] oriented KMWPO specimen, while (b-f) shows SAED patterns captured from region $v_1$-$v_5$, respectively.

APPENDIX

# C

# BOUNDARY INVESTIGATION

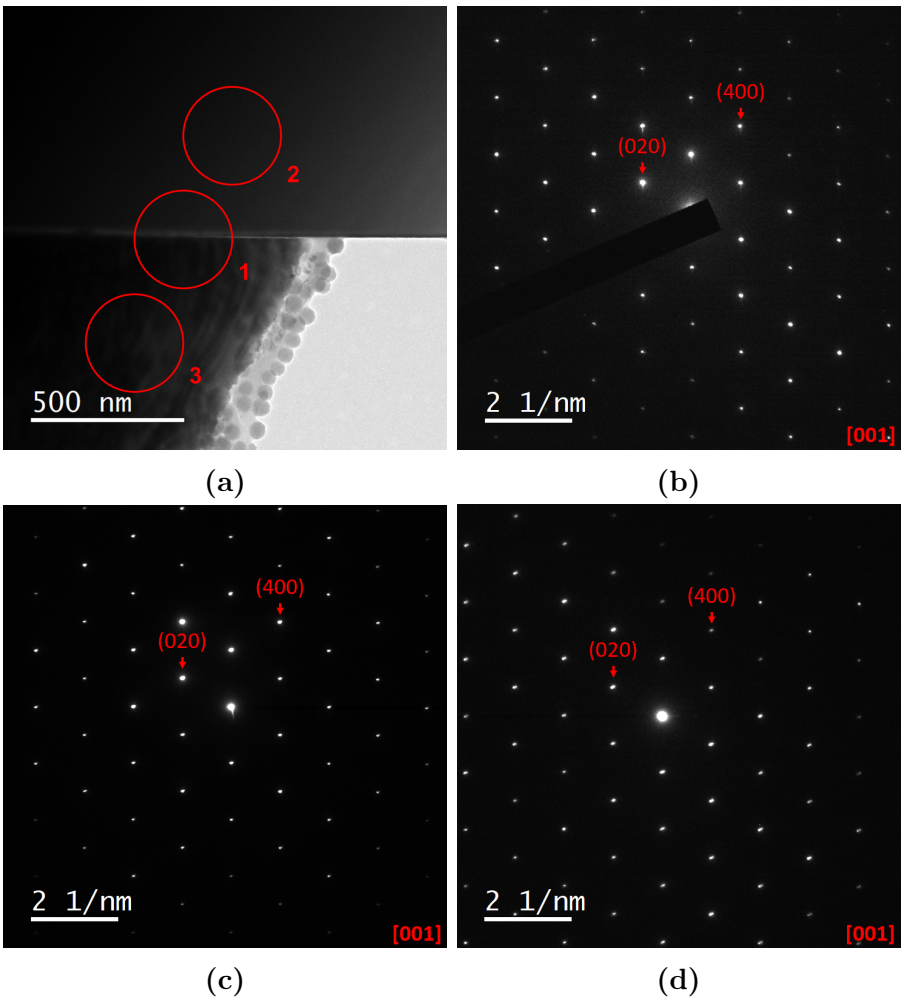


**(a)** **(b)**

**(c)** **(d)**

**Figure C.1:** (a) BF overview image of B1 with the relative positions of the SAED patterns marked with 1, 2, and 3, and (b-d) the SAED patterns from each location.

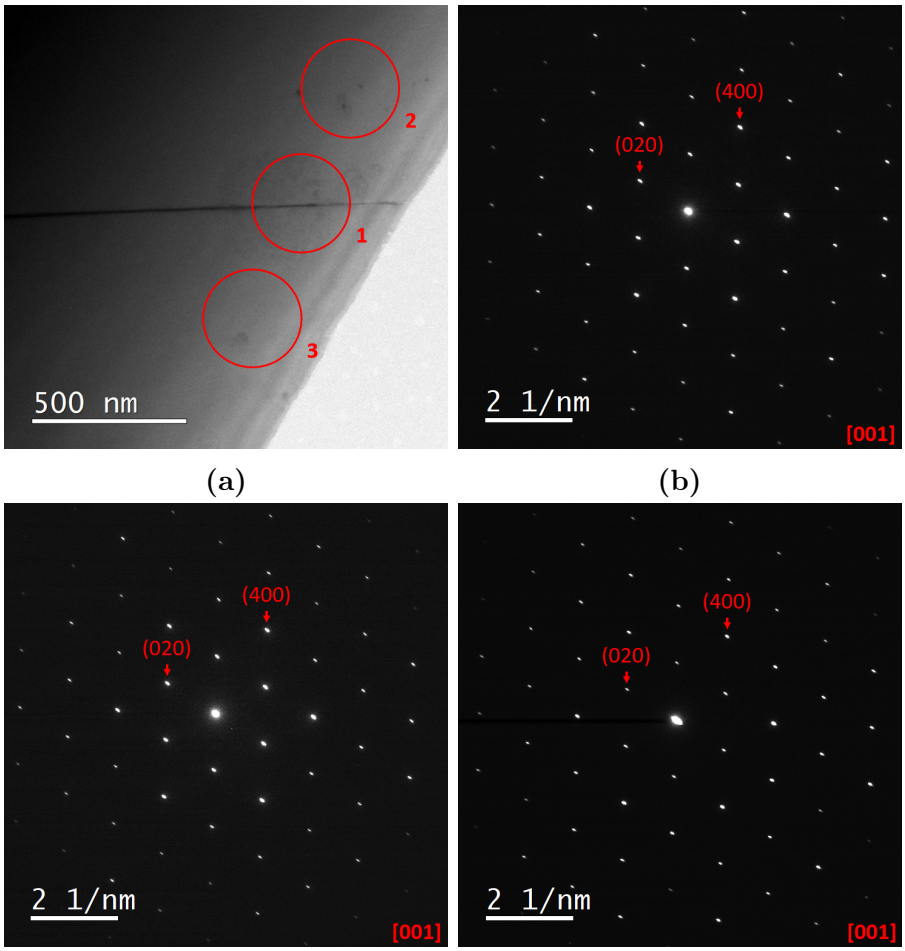


**Figure C.2:** (a) BF overview image of B2 with the relative positions of the SAED patterns marked with 1, 2, and 3, and (b-d) the SAED patterns from each location.

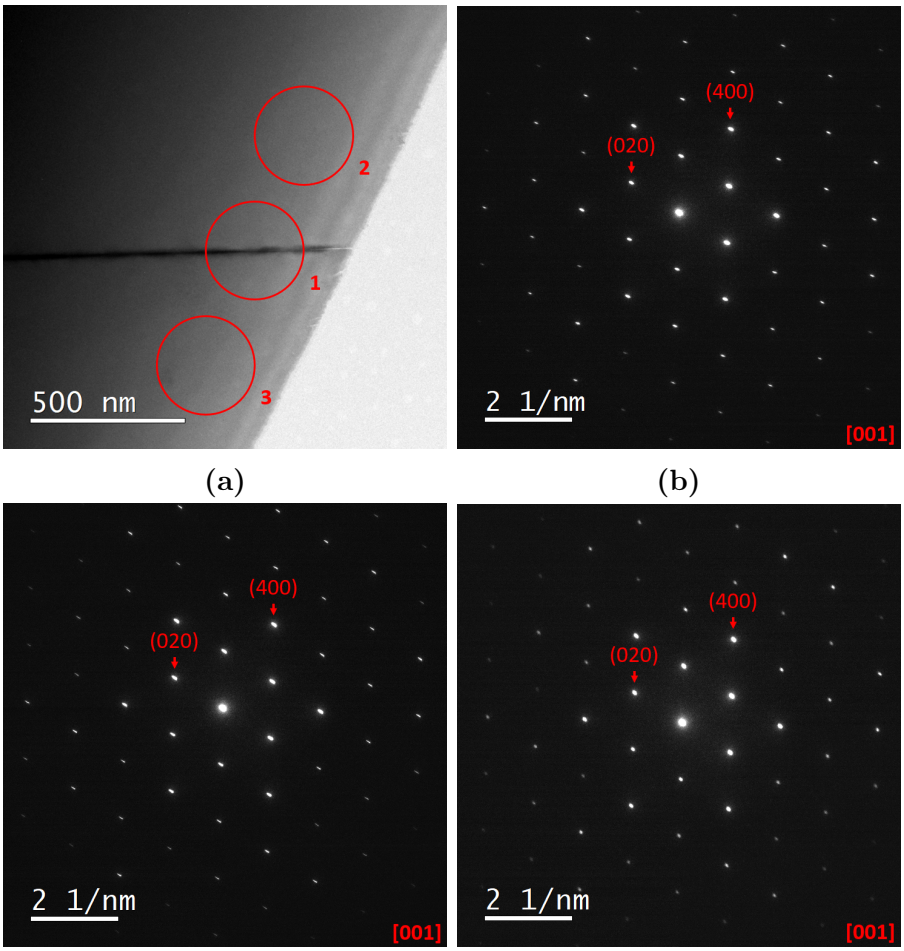


(a) (b) (c) (d)

**Figure C.3:** (a) BF overview image of B3 with the relative positions of the SAED patterns marked with 1, 2, and 3, and (b-d) the SAED patterns from each location.

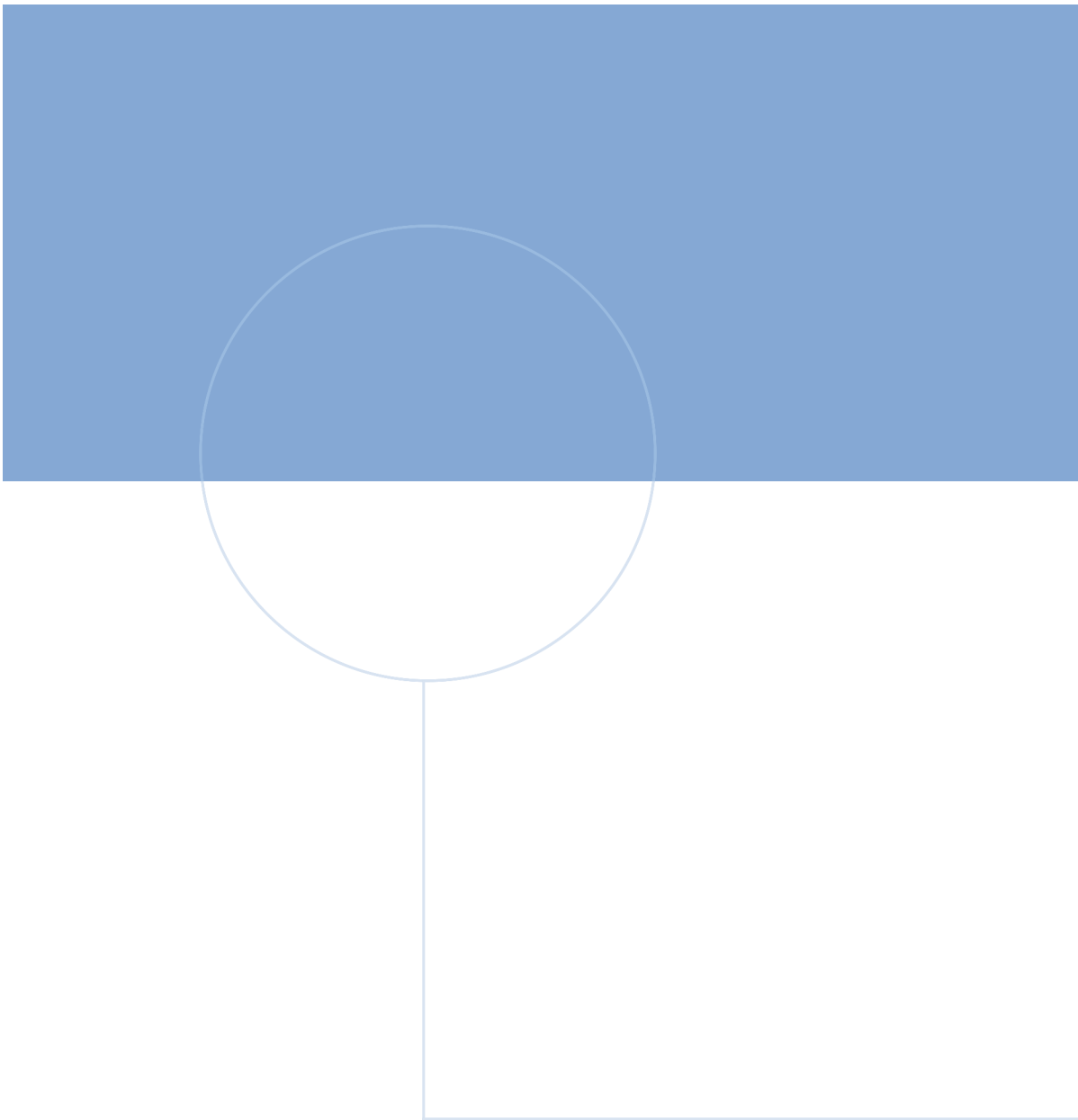

NTNU

Norwegian University of
Science and Technology